Efficient, High-Power Operation of CW Yb:YAG and Q-switched Nd:YAG Planar Waveguide Lasers

Ian James Thomson, MPhys (Hons)

Thesis Submitted for the Degree of Doctor of Philosophy

Heriot-Watt University

School of Engineering and Physical Sciences

March 2010

Abstract

The planar waveguide gain medium offers a good approach to creating a high-power lasers. Excellent thermal properties allow for lasers with good beam-quality and high-efficiency. A Neodymium doped YAG planar waveguide laser was actively Q-switched using a hybrid unstable resonator and acousto-optic modulator. A Ytterbium doped YAG planar waveguide laser was side-pumped using two laser diode stacks with a total of 800 W incident pump power.

The Nd:YAG planar waveguide laser has a core 200 μm thick and was face pumped with ten laser diode bars. Q-switching was achieved through the use of a new hybrid unstable resonator configuration providing high-speed modulation of the laser cavity. The laser produced 100 W of average power with a pulse repetition rate of 100 kHz, giving 1 mJ pulses with 50 ns duration. Shorter 15 ns pulses were achieved with 4.5 mJ pulse energy at lower pulse repetition rates.

The Yb:YAG planar waveguide laser has a 150 μm core thickness, side pumped by two 430 W, six-bar diode laser stacks. Each diode stack has a custom phase-plate, correcting for collimation errors and lens aberrations. These gave a line focus matching the dimensions of the waveguide core with an incident intensity on each side of approximately 22 kWcm^{-2}. Ray tracing of spontaneous emission within the waveguide core shows side facet angles of 7° and 20° were required to minimise ASE and parasitic oscillations within the waveguide core.

A technique to image the fluorescence from the Yb:YAG waveguide core has been developed. This technique allows for easy alignment of the pump lasers to the waveguide core and measurement of the pump intensity profile throughout the planar waveguide. This technique showed single-sided pumping to follow Beer's law, and with double-sided pumping considerably improved the pump uniformity. A diode laser probe was used to measure the gain present within the waveguide. The small signal gain coefficient was shown to be 1 cm^{-1} with a uniform profile across the width of the waveguide when pumped to saturation. This highlights the potential of operating the planar waveguide laser as an efficient amplifier.

High-power high-efficiency operation of the Yb:YAG planar waveguide laser was achieved through the use of a hybrid stable waveguide resonator. Output power of 400 W was extracted in a multi-mode beam with a slope efficiency of 75%. This result represents the highest output power from a diode-pumped solid-state planar waveguide laser to date.

Acknowledgements

Firstly, I would like to thank Professor Howard Baker and Professor Denis Hall for giving me the opportunity to work within the Laser and Photonics Applications Group. Particular thanks go to Howard, my supervisor, for the many hours of discussion and support he has provided over the last four years.

I would like to thank all of my many colleagues from the LPA group for all of their support, guidance and enthusiasm. Particular thanks go to those who I have worked most closely with: Dr. Jesus Valera, Dr. Fernando Monjardin, Dr. Aaron McKay, Dr. Fei Sun, Mr. Adam Russell, Mr. Victor Valles-Gomez, Ms. Natalia Trela, Mr. Krystian Wlodarczyk and Mr. Alberto Campos Zatarain. They have helped to make my time within the LPA group both productive and enjoyable.

I must also thank my many office mates over the last few years for their support and friendship, particularly, Dr. Ryan Warburton, Dr. Richard Moug, Dr. Keith Serrels, Mr. Spyros Brown and Mr. Ian Davidson. Of course, I must also thank all of the many people within the Physics department who have helped in many different ways during the course of my studies.

Special thanks must go to my parents and to my partner, Debbie. I am extremely grateful for their unwavering love and support throughout my studies.

List of Publications

Journal Publications

1. I. Thomson, J. Monjardin, N. Trela, H. Baker, D. Hall, "Double-edge pumped Yb:YAG planar waveguide laser with 400W output power", *In preparation*, 2010.

2. I. Thomson, H. Baker, D. Hall, "Pump and gain uniformity in a double-edge pumped planar waveguide laser", *In preparation*, 2010.

3. K. Wlodarczyk, I. Thomson, H. Baker, D. Hall, "CO_2 laser fabrication of sub-millimetre width mirrors for planar waveguide laser applications by localised vaporisation", *In preparation*, 2010.

4. J. Xu, I. Thomson, J. Valera, H. Baker, A. Russell, D. Hall, "A planar waveguide Nd:YAG laser using active Q-switching of a hybrid unstable resonator", *IEEE Journal of selected topics in quantum electronics*, vol. 13(3), pp. 638-646, 2007.

Conference Proceedings

1. I. Thomson, H. Baker, K. Wlodarczyk, N. Trela, D. Hall, "400W Yb:YAG planar waveguide laser using novel unstable resonators", *Proceedings of SPIE Photonics West*, Paper 7578-20, 2010.

2. H. Baker, J. Monjardin, I. Thomson, N. Trela, J. Valera, D. Hall, "Development of edge pumped planar waveguide lasers", *Proceedings of SPIE Photonics West*, Paper 6871-23, 2008.

Conference Papers

1. I. Thomson, H. Baker, K. Wlodarczyk, N. Trela, D. Hall, "400W Yb:YAG planar waveguide laser using novel unstable resonators", *Paper presented at SPIE Photonics West conference*, San Francisco, USA, 2010.

2. I. Thomson, H. Baker, N. Trela, J. Monjardin, J. Valera, D. Hall, "Double sided diode edge-pumped Yb:YAG laser with 230W output power", *Paper presented at CLEO conference*, Baltimore, USA, 2009.

3. K. Wlodarczyk, I. Thomson, H. Baker, D. Hall, "Mode-selective toroidal mirrors for unstable resonator planar waveguide and thin-slab solid state lasers", *Paper presented at ECLEO conference*, Munich, Germany, 2009.

4. A. McKay, V. Valles-Gomez, I. Thomson, H. Baker, D. Hall, "Development of solid-state laser technologies", *Paper presented at James Watt Institute for High-value Manufacturing conference*, Heriot-Watt University, Edinburgh, 2009.

5. I. Thomson, J. Monjardin, N. Trela, J. Valera, H. Baker, D. Hall, "Width scaling of diode-pumped Yb:YAG planar waveguide lasers", *Paper presented at Europhoton '08 conference*, Paris, France, 2008.

6. I. Thomson, J. Monjardin, N. Trela, J. Valera, H. Baker, D. Hall, "Development of width-scaled edge pumped planar waveguide lasers", *Paper presented at IoP Photon '08 conference*, Heriot-Watt University, Edinburgh, 2008.

7. H. Baker, J. Monjardin, I. Thomson, N. Trela, J. Valera, D. Hall, "Development of edge pumped planar waveguide lasers", *Paper presented at SPIE Photonics West Conference*, San Jose, USA, 2008.

8. I. Thomson, J. Valera, H. Baker, D. Hall, "Q-switching dynamics of an efficient unstable resonator, planar waveguide laser", *Paper presented at Europhoton '06 conference*, Pisa, Italy, 2006.

9. H. Baker, J. Valera, A. Russell, I. Thomson, D. Hall, "Q-switching of an unstable resonator for a high average power planar waveguide Nd:YAG laser", *Paper presented at CLEO conference*, Long Beach, USA, 2006.

Contents

List of Variables

a - Planar waveguide core half-thickness.

a_1 - Planar waveguide core half-thickness incorporating evanescent field contribution.

L_{wg} - Planar waveguide length.

W_{wg} - Planar waveguide width.

a_{max} - Maximum planar waveguide core half-thickness for a single-mode waveguide.

n_1 - Planar waveguide core refractive index.

n_2 - Planar waveguide cladding refractive index.

m - Planar waveguide mode order.

β_i - Waveguide mode longitudinal propagation constant.

NA - Numerical aperture.

k_0 - Wave vector.

Q_{max} - Maximum thermal load that can be applied to a planar waveguide before thermal-guiding dominates index-guiding.

Z_r - Rayleigh Range.

R_n - Radius of curvature of resonator mirror n.

L - Air-equivalent resonator cavity length.

M - Magnification of a confocal unstable resonator.

OC - Output coupling of a laser resonator.

d_n - Separation of mirror n from planar waveguide facet.

$w(z)$ - Beam width at position z.

w_0 - Beam width at beam waist.

Z_0 - Position of beam waist.

g_0 - Small-signal gain coefficient.

G - Double-pass amplification factor.

ρ_n - Q-switched pulse energy at intra-cavity position n.

$M(t)$ - Acousto-optic modulator transmission function.

R - Output coupler reflectivity.

EFL - Effective focal length of a lens.

η_{slope} - Slope efficiency.

I_s - Laser saturation intensity.

$I_{p,s}$ - Pump saturation intensity.

P_{avail} - Power available to be extracting as useful laser output.

V - Volume of gain medium.

σ_a - Pump transition absorption cross-section.

σ_e - Laser transition emission cross-Section.

τ - Upper laser manifold lifetime.

τ_{pair} - Upper manifold lifetime of cooperative luminescence process.

$E_{l,n}$ - Energy of lower manifold n.

$E_{u,n}$ - Energy of upper manifold n.

$f_{l,n}$ - Fractional population in lower manifold n.

$f_{u,n}$ - Fractional population in upper manifold n.

N_0 - Total active ion dopant density.

P_{out} - Laser output power.

P_p - Incident pump power.

P_{th} - Threshold pump power for laser oscillation.

η_{del} - Pump delivery efficiency.

η_{po} - Pump overlap efficiency with laser mode.

η_{lo} - Laser mode overlap efficiency with doped-core.

$h\nu_p$ - Pump photon energy.

$h\nu_l$ - Laser photon energy.

T - One-way waveguide transmission.

Chapter 1

The Technology of Planar Waveguide Lasers

1.1 Introduction

Many applications require the use of compact, efficient, high-power lasers with good beam quality, such as laser machining, marking and ranging. These applications require both continuous-wave (CW) and pulsed lasers operating from a few watts of power up to the kilowatt range, with increasing interest in 100 kW CW lasers for military applications [1]. Currently, the solid-state laser fills many of these roles, however, when operated at high-powers, the bulk solid-state laser has several problems related to heating of the gain medium through pumping, such as thermal lensing, and eventually damage to the laser crystal [2]. By increasing the surface area to contained volume ratio of the active region, it is possible to improve the cooling efficiency of the active region resulting in less distortion due to heating [3, 4]. There are different types of laser using this idea such as the thin disc laser, discussed in section 1.7.1, the fibre laser, discussed in section 1.7.2, slab lasers and planar waveguide lasers, the subject of this thesis. The excellent thermal properties of the planar waveguide laser are advantageous for scaling to high-power devices and temperature-sensitive quasi-three-level laser systems. The small active-area also allows high-inversion densities to be reached more easily than traditional rod lasers, allowing interesting transitions such as Nd:YAG operating efficiently on the quasi-three level, 946 nm laser transition [5] and overcoming the ground-state absorption in Yb doped materials [6]. There is also interest in low power planar waveguide lasers to create on-chip, integrated devices in which the resonator and any modulators can be contained in one package.

Planar waveguide lasers have existed in many forms since the first was demonstrated in 1971 [7] consisting of a dyed thin-film on a dielectric substrate. The planar waveguide format was then demonstrated very successfully for high-power operation using hollow bore CO_2 waveguides pumped using an RF discharge. Degnan and Hall detailed efficient waveguide resonators [8] and over the two-decades leading up to the 1990's power scaling to the 1 kW power level [9] and beyond was achieved, with com-

mercial CO_2 planar waveguide lasers capable of 20 kW power output [10]. It wasn't until the late 1980's that solid-state planar waveguide laser research became an active research area due to the availability of cheap, high power diode laser sources capable of pumping solid-state laser materials [11]. In 1997, the 1 W output power barrier was broken by Millas *et al.* within the Laser and Photonics Applications group at Heriot-Watt University [12], introducing a diode-face pumped Nd:YAG planar waveguide giving 9 W of quasi-continuous-wave (QCW) output power. Improvements to the face pumping geometry resulted in Lee *et al.* [13] demonstrating 150 W CW output power in a multi-mode beam and ∼100 W with near diffraction-limited beam quality achieved using a hybrid negative-branch unstable resonator, previously developed for CO_2 planar waveguide lasers. Sueda *et al.* [6] have demonstrated 250 W CW output power from a sapphire clad Yb:YAG planar waveguide, with a thick 500 μm core resulting in a laser they termed a micro-thickness slab laser. More recently, Xiao *et al.* [14] have demonstrated 280 W QCW output power from a Nd:YAG planar waveguide laser with 38% slope efficiency, whilst Mackenzie *et al.* have demonstrated 35 W output from the unusual 946 nm quasi-three-level transition of Nd:YAG resulting in a slope efficiency of 57%.

1.2 Thesis Structure

The aim of this thesis is to extend the operation of the planar waveguide solid-state laser into the high-energy pulsed regime with excellent beam quality, building on the CW laser developed by Lee *et al.* [13]. The second aim of this thesis, is to investigate power scaling of planar waveguide lasers towards 500 W CW output utilising novel beam corrected high-brightness diode stacks to pump an Yb:YAG planar waveguide, increasing the conversion efficiency from that obtained using Nd:YAG, demonstrating the power scaling ability of the planar waveguide geometry. The research presented within this thesis was almost entirely carried out by the author, however, some equipment that was used was built by other members of the Laser and Photonics Applications group, whilst some work was carried out in collaboration with other members of the research group. Due to this, the work carried out with collaborators is clearly stated at the beginning of each chapter.

The thesis is organised into chapters based on subject area. This chapter gives an introduction to the thesis and discusses the technology used to create a high-power solid-state planar waveguide laser and the resonators required to give good beam quality. Chapter 2 discusses active Q-switching of an unstable resonator planar waveguide laser, with the work from this chapter resulting in a publication in the IEEE Journal of Selected Topics in Quantum Electronics [15]. Chapter 3 introduces a side-pumped Yb:YAG planar waveguide laser, the laser design is discussed and early trials of the

laser are presented, highlighting a number of issues with the original configuration. Chapter 4 describes improvements to the Yb:YAG laser design, with an analysis of the pump uniformity and gain within the active medium under intense pumping performed. Chapter 5 presents high-efficiency, high-power operation of the Yb:YAG planar waveguide laser and introduces novel toroidal shaped resonator mirrors produced using a CO_2 laser ablation technique. Finally, chapter 6 concludes and discusses future work including amplifier operation and possible resonator improvements.

1.3 Planar Waveguide Properties

This section discusses the properties of diode-pumped solid-state planar waveguide lasers. Fabrication methods are discussed, with contact bonding being the method utilised to produce the planar waveguides used within this thesis. Waveguide propagation is reviewed, with the waveguide mode equations presented. Different methods of diode pumping are presented and the maximum power density that can be applied to planar waveguides of varying core thicknesses is shown.

1.3.1 Fabrication

Planar waveguide fabrication is typically produced using one of two methods. Either modifying the refractive index of a bulk material or layering different materials to create a waveguide. Modifying bulk materials can be achieved through the use of ion exchange [16], ion implantation [17] or direct laser writing, where a pulsed laser is used to directly alter the materials refractive index. Modifying bulk material methods typically produce thin waveguides with low numerical apertures (NA). To produce waveguides using dissimilar materials, techniques such as molecular beam epitaxy [18], liquid phase epitaxy [19], and pulsed laser deposition [20] can be used in which the waveguide is grown onto a substrate.

The technique used for the planar waveguide lasers presented in this thesis is contact bonding of dissimilar materials, developed by Onyx Optics [21], with the fabrication method described in references [22, 23, 24]. The materials used are first precision polished to the dimensions required, the materials are then brought into contact with each other allowing the Van der Waals forces to bond the dissimilar materials together. It allows extremely strong bonds to be formed without the requirement of adhesives and is independent of the material properties. This technique allows planar waveguides to be manufactured with effectively any core thickness. The cladding layers can be manufactured to any thickness required depending on the thermal and optical properties the planar waveguide is to have. The only limitation on

bonding dissimilar materials is the thermal expansion coefficient must be similar, so that heating of the device does not introduce differential stress causing thermal lensing and possible mechanical failure of the active medium. Multiple waveguides can also be bonded together end to end using the same technique giving zero-loss joints, allowing devices of any size to be formed with the limiting factor becoming the cost. The technique can also be used to create double-clad waveguide structures, enabling easier pump coupling [25].

1.3.2 Waveguide Propagation

This section details an approximation for the modes which can propagate in the transverse direction through a planar waveguide. An exact solution for the waveguide modes can be found using the standard analysis presented in reference [26]. The waveguide core thickness is defined as $2a$, with n_1 being the core refractive index and n_2 being the cladding refractive index which are required to be of infinite extent as shown in figure 1.1a). The definition of the co-ordinate axis to be used in the following analysis and throughout the rest of the thesis is presented in figure 1.1b).

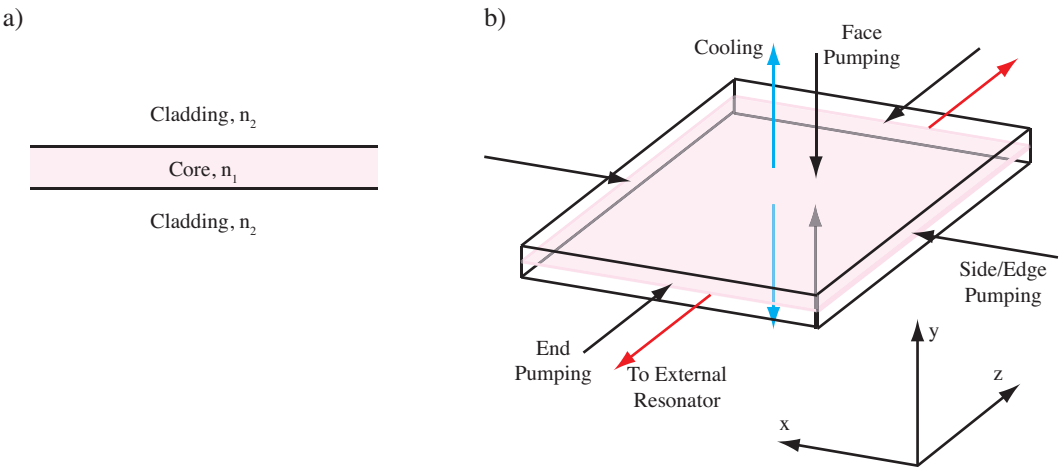

Figure 1.1 – a) Side view of a planar waveguide structure with infinite claddings. b) Schematic of different pumping schemes and cooling of planar waveguide lasers.

Even waveguide modes, where the mode number, m, is an odd number can be expressed using equation 1.1.

$$W_i(y_1) = E_0 \cos\left(\frac{m\pi y_1}{2a_1}\right) \exp(-i\beta_i z) \tag{1.1}$$

Similarly, the odd waveguide modes, where m is an even number can be expressed using equation 1.2 where $W(y)$ is the profile of the waveguide mode.

$$W_i(y_1) = E_0 \sin\left(\frac{m\pi y_1}{2a_1}\right) \exp(-i\beta_i z) \tag{1.2}$$

The longitudinal propagation constant, β_i can be expressed using equation 1.3. Whilst the waveguide core height, a_1, depends on the waveguide being either strongly or weakly guiding [27]. E_0 is the amplitude of the mode profile. For weakly guiding waveguides, a correction factor to the waveguide core height is required to compensate for the strong evanescent field contribution according to equation 1.4, whereas for strongly guiding waveguides, a_1 is simply the physical half-width of the guide.

$$\beta_i = \frac{\lambda \pi i^2}{4 n_2 a_1^2} \tag{1.3}$$

$$a_1 = a + \frac{\lambda}{2\pi NA} \tag{1.4}$$

A naming convention is defined to identify each waveguide mode, consisting of the polarisation and number of anti-nodes within the mode profile. The fundamental TE mode has a single anti-node, and as such is labelled TE_1, similarly, the first odd TM mode has 2 anti-nodes, labelled TM_2. The TE and TM polarisations are nearly degenerate, therefore, within this thesis, all calculations are performed on TE polarisations but are equally applicable to TM polarisations. Previous work on a large-core Nd:YAG planar waveguide [28] showed the waveguide only supports TE polarised mode and this was attributed to stress induced to the waveguide during manufacture.

There are two common types of planar waveguide, single-mode and multi-mode. The number of modes a waveguide will support depends on the R parameter given by equation 1.5 [26].

$$R = k_0 a_1 NA \tag{1.5}$$

Where $k_0 = \frac{2\pi}{\lambda}$ and $NA = \sqrt{n_2^2 - n_1^2}$. The number of guided modes, n, is calculated using $n = \frac{2R}{\pi}$. The maximum core height a waveguide can have, whilst maintaining single mode operation can be expressed as a_{max}, given by equation 1.6. This is calculated by setting $n = 1$ and shows that the maximum allowed core thickness for single-mode operation decreases with increased NA.

$$a_{max} = \frac{\lambda}{4NA} \tag{1.6}$$

Within this thesis, two planar waveguides are used, both with large core height giving multi-mode operation. The first is a weakly guided planar waveguide with a 200 μm Nd:YAG core surrounded by undoped 0.4 mm YAG claddings. In this case, the core refractive index is $n_1 = 1.8216$ with the cladding refractive index $n_2 = 1.8212$, this results in a significant evanescent field contribution, increasing the core height by

5.4 μm. The second waveguide used within in this thesis consists of a 150μm Yb:YAG core ($n_1 = 1.82$) and 1 mm sapphire claddings ($n_2 = 1.77$), giving strong guiding with minimal evanescent cladding contribution to the waveguide height.

1.3.3 Diode-Pumping and Cooling

The planar waveguide structure utilises a thin core which can be pumped using diode lasers in a number of ways as shown in figure 1.1b) with the structure cooled through the largest two faces. For high power solid-state lasers, two types of diode laser are typically used, diode bars and diode stacks. A diode bar consists of multiple single diode emitters all packaged in the same device side by side, currently a single bar can have an output power up to 100 W. A diode stack consists of multiple diode bars packaged on top of each other to form a stack, diode stacks are currently available with output power up to 1 kW from a stack consisting of ten diode bars.

Cooling of the waveguide structure can be achieved through the use of either cold water flowing directly over the largest surfaces or direct contacting of water cooled heatsinks to the surfaces. Both techniques have been employed within this thesis with face-pumping enabled using the direct water cooling technique and side pumping with direct contact heatsinks.

In-plane Pumping

In-plane pumping using diode bars can be achieved using one of two methods, butt coupling or imaging. Diode bars offer an ideal pump source for a planar waveguide laser due to it matching the shape of the waveguide.

Butt coupling offers low-loss coupling of the pump light into the guiding core. However, diode lasers diverge rapidly in the fast-axis, if the divergence is high enough, the pump light can quickly couple out of the waveguide core and into the claddings. Double clad planar waveguide structures can be used to overcome this problem, by guiding the pump light via the larger, outer core as shown in figure 1.2 [29]. A disadvantage of butt-coupled pumping is the mis-match of the pump light with the laser mode.

Imaging the diode bar or stack into the planar waveguide offers an alternate solution for in-plane pumping. The imaging system adds complexity and introduces coupling loss into the pumping scheme, however, the imaging system can be designed such that the pump light is guided within the waveguide core without coupling into the claddings. Within this thesis, in-plane pumping using an imaging system with custom aberration correction phase-plates resulting in more than 90% of the pump-light coupling into the waveguide core. Sueda *et al.* [6] have also utilised in-plane

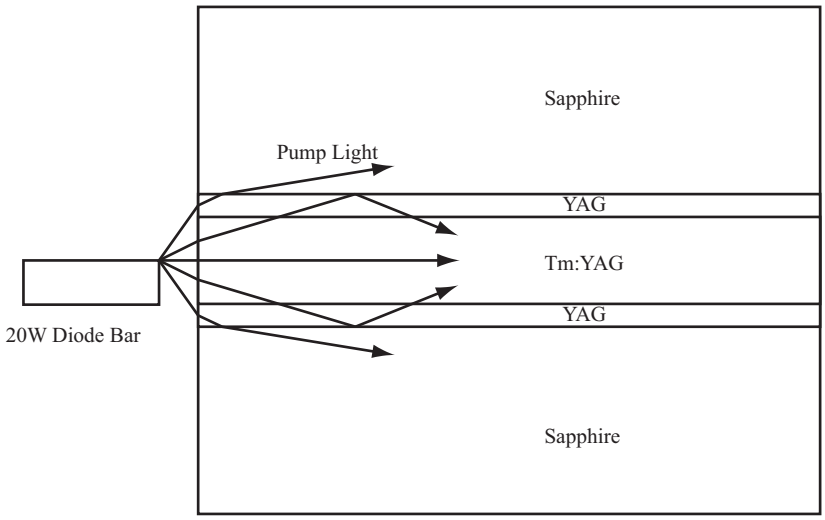

Figure 1.2 – Butt coupled diode pumping of a double clad planar waveguide. Figure adapted from [29].

pumping, coupling two 8-bar diode stacks into a 500 μm core height Yb:YAG planar waveguide clad with sapphire, giving an optical to optical efficiency of 42%.

Face Pumping

Multi-bar face pumping, developed by Faulstich *et al.* [12], enabled efficient pumping of Nd doped planar waveguide. This work introduced the idea of direct coupling the diode stacks to the largest waveguide faces, with a slotted mirror over the stack and second mirror on the opposite side of the waveguide enabling multi-pass face pumping. Lee *et al.* [13, 28] incorporated this design into pumping the Nd:YAG planar waveguide laser used in chapter 2 of this thesis. Figure 1.3 shows a schematic of the pumping configuration. All six faces of the planar waveguide are precision polished. The waveguide is sealed into a pump chamber with a 1 mm gap to two fused silica windows with cooling water pumped laterally through this gap. Above the waveguide a 10 bar diode stack emitting 450 W is aligned to a slotted reflector and aligned to the largest waveguide face. The opposite side of the waveguide has a second reflector positioned to reflect the pump light back towards the diodes, due to the high divergence of the pump light in the fast axis, only a small fraction of the light re-enters the pump diodes with the majority reflected back from the slotted reflectors. This configuration pumps the entire core uniformly with an estimated pump absorption of 70% and a pump density of 2.8 kWcm^{-3}. Face pumping is mainly applicable to 4-level laser systems, as the 3-level nature of materials such as Yb:YAG require a much higher intensity to reach the transparency threshold.

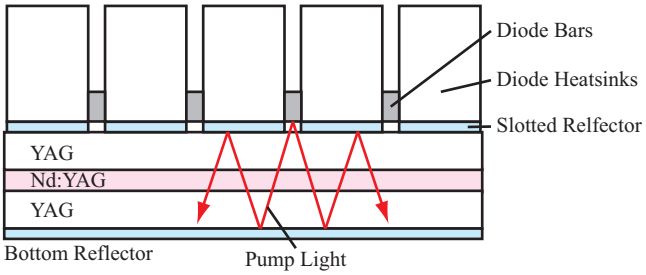

Figure 1.3 – Face pumping of large core planar waveguide structures. The diode pitch should be significantly greater than the mounted mirror separation for the pump transfer efficiency to be high [28].

Cooling

Heating of the waveguide structure causes a change in refractive index. J. Lee [28] has shown the heating causes a parabolic refractive index profile to form which increases in strength with heat and is very dependant on the core thickness. The guided modes within a parabolic guiding structure are Hermite-Gaussian [26], and are no longer apertured by the step-index structure when the spot-size becomes $\pi w \leq 2a$. To avoid thermal guiding, a thin core is required. The maximum heat density, Q_{max}, before the step-index of the planar waveguide has no effect on the guided mode is defined by equation 1.7 [28] for both TE and TM polarisations.

$$Q_{max} = \frac{\lambda^2 \pi^2 k}{\left(\frac{dn_0}{dT} + \frac{1}{2} n_0^3 (q_{m1} + q_{m3}) \frac{E\alpha}{(1-v)}\right) n_0 a^4} \tag{1.7}$$

Where m=1 denotes the TE polarisation, m=2 denotes the TM polarisation, $\frac{dn_0}{dT}$ is the variation in core refractive index with temperature, α is the thermally induced stress, k is the thermal conductivity of the core, q is the piezo-optic tensor for the core material, v is Poisson's ratio and E is Young's modulus.

Figure 1.4 shows the solution to equation 1.7, solved by F. Monjardin for YAG planar waveguides, with the water cooling limit of 300 Wcm^{-2} included [30]. The two shaded regions represent the areas at which Nd and Yb doped YAG are operated within this thesis. Both the Nd:YAG planar waveguide with a 200 μm core and the Yb:YAG planar waveguide with 150 μm core height can handle significantly more pump power than that applied within this thesis before reaching the thermal guiding limit and cooling limits.

1.4 Planar Waveguide Laser Resonators

This section reviews the theory of waveguide coupling and different types of resonator that have been used in the past to efficiently extract power from a planar waveguide

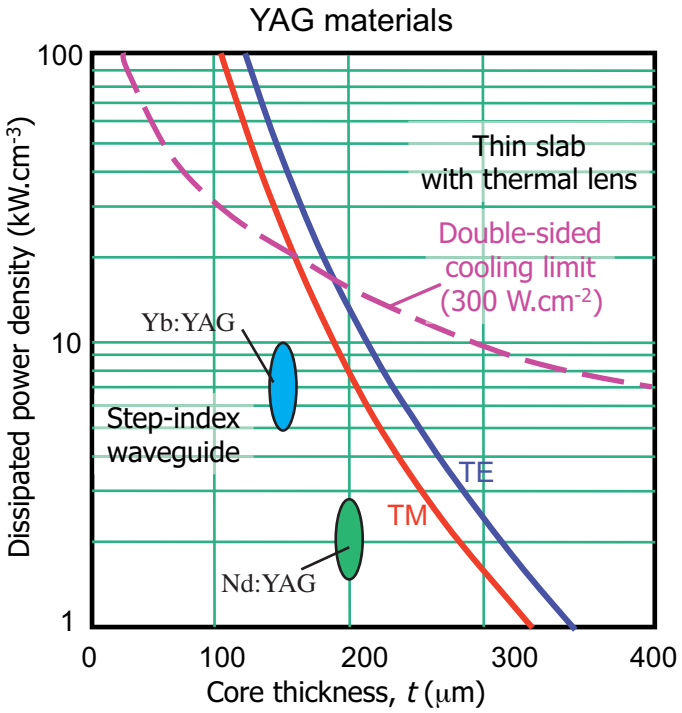

Figure 1.4 – The transition from step-index guiding to thermal guiding for YAG materials for TE and TM polarisations. Figure extracted from [30].

gain medium. This section only considers resonators utilising external coupling mirrors, not monolithic devices where the ends of the waveguide itself form the resonator mirrors. Monolithic cavities are suitable for single-mode waveguides, where the guide itself gives spatial mode selection, whereas, multi-mode waveguides require external coupling to limit operation to only low-order modes.

1.4.1 Waveguide coupling

This section discusses the coupling of a waveguide mode into free-space, then efficiently coupling it back into the core of the guiding structure, thus creating feedback for creating a waveguide resonator. The method used here is a modified version of the technique proposed by Degnan and Hall [8], presented by J. Lee [28]. This method uses the Huygens integral, equation 1.8, to couple the waveguide mode into free-space.

$$F_i(x_2) = \int_{-a}^{a} W_i(x_1) K(x_1, x_2) dx_1 \tag{1.8}$$

Where $F_i(x_2)$ is the free-space mode after the waveguide mode, $W_i(x_1)$, has propagated into free-space with $K(x_1, x_2)$ being the Huygens kernel in one-dimension. Siegman [31] shows the Huygens kernel can be written including the components of an ABCD matrix as shown in equation 1.9, this allows for an arbitrary waveform to be propagated through a generalised ABCD system.

$$K(x_1, x_2) = \sqrt{\frac{i}{B\lambda}} \exp[-i\frac{\pi}{B\lambda}(Ax_1^2 + Dx_2^2 - 2x_1x_2)] \tag{1.9}$$

A, B, and D are the components of an ABCD matrix, x_1 is the transverse direction at the end-facet, whilst x_2 is the transverse direction at an arbitrary distance from the end facet. In this case of waveguide coupling, the ABCD matrix is for propagation over a free-space distance, reflection from a mirror of arbitrary curvature, then reverse propagation back to the waveguide facet. ABCD matrices for each of these stages are given by Siegman [31]. The coupling efficiency of this returned mode can be determined by performing an overlap integral on the return mode as shown in equation 1.10.

$$c_{ij} = \int_{-a}^{a} W_i F_j^* dx \tag{1.10}$$

Where F_j^* is the complex conjugate of F_j. The coupling efficiency of the returned mode into the initial waveguide mode can be calculated using equation 1.11, where both W_i and F_j are normalised so the integral over the waveguide core is equal to one.

$$\eta_{ij} = 1 - c_{ij}c_{ij}^* \tag{1.11}$$

To determine the radius of curvature a mirror requires and its separation from the waveguide facet for efficient coupling, the mirror curvature must closely match the curvature of the phase front associated with the fundamental waveguide mode. It has been shown [28] that a Gaussian TEM_{00} mode of width $0.7a$ has 99.6% overlap with the fundamental waveguide mode. Therefore, the curvature of the phase front after propagation from the waveguide facet a distance z can be approximated using equation 1.12.

$$R = z\left[1 + \left(\frac{z_r}{z}\right)^2\right] \tag{1.12}$$

Where z_r is the Rayleigh range, defined by $z_r = \frac{\pi a^2}{2\lambda}$. Figure 1.5a) [28] shows a plot of the normalised curvature required for a given distance from the waveguide facet for the 200 μm core height Nd:YAG waveguide used for the work performed in chapter 2. For each mirror curvature and corresponding separation, the coupling efficiency for the fundamental TE_1 waveguide mode can be seen in figure 1.5b) [28]. The minima on each figure for the case III condition is slightly below a normalised mirror distance of one, this is due to the waveguide mode not completely matching a Gaussian. If a TEM_{00} Gaussian beam is used for the calculations, the minima occurs at exactly one.

Any thermal lensing within the planar waveguide structure will further deviate the minima from this ideal position.

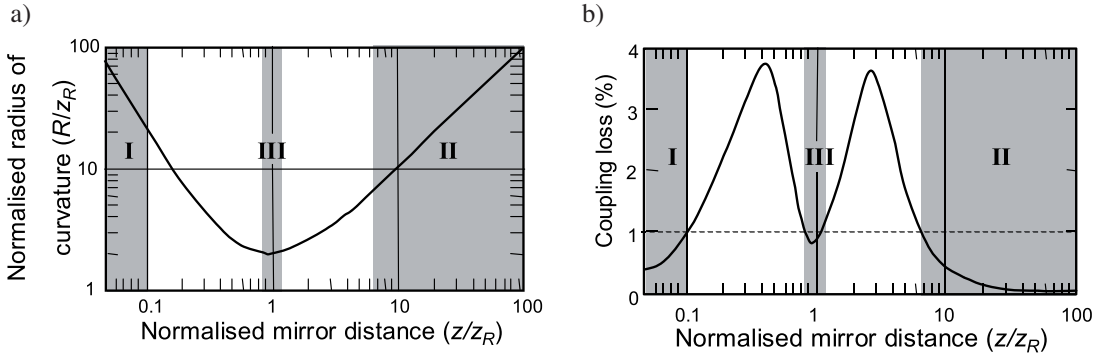

Figure 1.5 – a) Mirror curvature required to match the phase front of the fundamental waveguide mode after propagation through free-space to a distance z. b) Waveguide coupling loss associated with each mirror position. The three shaded areas represent the areas in which a low-loss waveguide resonator can be formed. Figure extracted from [28].

These results confirm the three low loss waveguide resonator conditions where coupling losses are less than 1% identified by Degnan and Hall [8]. The case I condition consists of a mirror with very large, effectively flat, curvature a short distance from the waveguide facet. Case II requires the radius of curvature of the mirror to match the mirror to facet separation known as the concentric condition, it also requires the mirror to be in the far-field, more than 6-7x the Rayleigh range. Both of these cases efficiently couple back all waveguide modes, meaning external mode control such as an intra-cavity slit is required to control the transverse beam-profile when used with a multi-mode waveguide.

The third low loss condition, case III, is the point at which the mirror is placed one Rayleigh range from the waveguide facet with a curvature two times the Rayleigh range known as the confocal position. This position efficiently couples the TE_1 mode whilst coupling higher order modes back into the core with poor efficiency, offering natural mode selection, decreasing the number of intra-cavity components required for single-mode operation of a multi-mode planar waveguide. Ideal Case III operation offers a fundamental mode with an M^2 of 1.12, the diffraction limited beam quality associated with the fundamental waveguide mode.

Figure 1.6 shows a schematic of the 3 low-loss waveguide coupling conditions. Fundamental mode selection requires either case II coupling with an intra-cavity slit or case III coupling. Case I coupling does not provide mode selection, therefore monolithic cavities require a single mode waveguide core [22]. Using single-mode planar waveguides is not suitable for scaling to high powers beyond 100 W due to the increased intensity within the waveguide core approaching the damage thresholds for

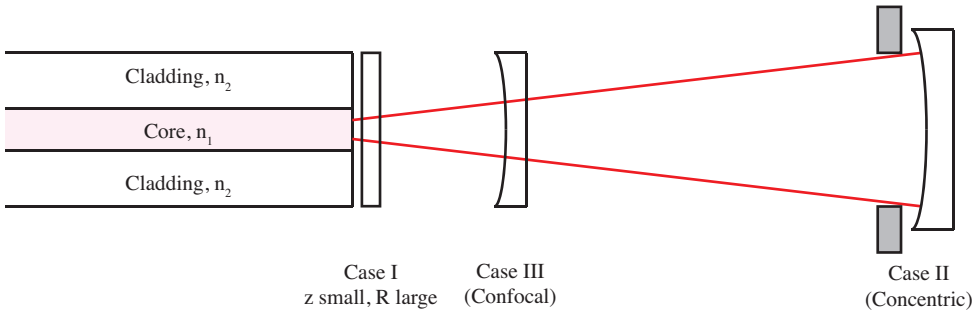

Figure 1.6 – The three low-loss waveguide coupling conditions, case I requires a large curvature mirror placed very near to the laser facet, case II requires the mirror curvature to match the facet-mirror separation whilst case III requires the mirror to be placed one Rayleigh range from the facet with curvature twice the Rayleigh range.

typical solid-state laser materials. To overcome this, large core, multi-mode planar waveguides are required with case II or case III resonators for power scaling towards 1 kW average power with near diffraction limited beam quality.

The beam propagation method presented here, coupling an arbitrary waveform through a general ABCD system is the method utilised to compare the measured planar waveguide laser mode structure with the theoretical mode structure in chapter 5 of this thesis. This allows the mode structure of the laser output to be determined.

1.4.2 Resonators for Planar Waveguide Lasers

The large width to height aspect ratio of the planar waveguide causes difficulties in creating a resonator for a planar waveguide laser with very different resonators in the lateral and transverse directions required. Laterally, the active region is very wide, requiring a resonator that can both extract energy from a large area and give good beam quality. In the transverse direction, the low-loss waveguide coupling conditions must be satisfied. The simplest resonator utilising a plane-plane Fabry-Perot cavity is useful for extracting power, however, in the transverse direction there are many spatial waveguide modes present, whilst in the lateral direction the beam is highly multi-mode due to the large width of the active region. A more complicated option is to use a concave case II rear mirror with a plane output coupler, using a mode-selecting slit to only allow the fundamental mode to propagate as shown in figure 1.6. However, in the lateral direction, fundamental mode operation also requires an intra-cavity aperture, with the fundamental mode no longer filling the full width of the active region limiting the gain that can be extracted.

Early studies of laser cavities focussed on stable resonator operation. Ananev *et al.* [32] introduced the concept of an unstable resonator to provide mode control, referring

to it as a telescopic resonator. Further work on the unstable resonator proved it to have near diffraction limited beam quality whilst still managing to efficiently extract energy from a wide active region [33, 34]. A key development in unstable resonators was the confocal unstable resonator developed by Krupke and Sooy [33], giving a near diffraction limited, collimated output beam.

Confocal unstable resonators are particularly useful as they have a collimated output beam and are the type used within this thesis. The confocal resonator also has the useful property of any ray starting on the resonator axis will walk out of the resonator sweeping out the majority of the available energy in the lateral direction, making it extremely useful for large active area lasers. Confocal unstable resonators can be separated into two categories, positive branch and negative branch. Figure 1.7 shows a schematic diagram for the two types of confocal unstable resonator, whilst equations 1.13 and 1.14 show how the positive branch and negative branch resonators fulfil the confocal condition respectively. R_1 and R_2 are the curvatures of the two mirrors where positive is defined as the centre of curvature facing toward the centre of the resonator and L is the air-equivalent cavity length, defined below. The negative branch resonator has a disadvantage in that the intra-cavity focal point causes a high-intensity region within the cavity risking optical damage to intra-cavity components, it is however, significantly more tolerant to misalignment than the positive branch resonator as discussed by Krupke and Sooy [33]. The confocal resonator consists of an unstable periodic focussing system, in which the light is eventually coupled from the edge of one mirror. Output coupling is achieved by either using a hard or soft edged mirror [31], the hard edged mirror is smaller in dimension than the opposite mirror, enabling the trapped light within the cavity to eventually couple out around the edges. Soft edged coupling is achieved through varying the reflectivity of the output coupler across its width, typically High-reflectivity (HR) in the centre with a Gaussian reflectivity profile becoming an anti-reflectivity (AR) coating at the edges. Hard edges have the disadvantage of causing a weak diffraction pattern in the output beam, whereas soft edged mirrors are expensive to produce due to the complexity of the optical coating required.

$$R_1 - R_2 = 2L \tag{1.13}$$

$$R_1 + R_2 = 2L \tag{1.14}$$

Equation 1.15 defines the magnification of the unstable resonator, this is an important factor as it defines the equivalent output coupling of a one-dimensional unstable resonator as shown in equation 1.16. The magnification is also used in the selection

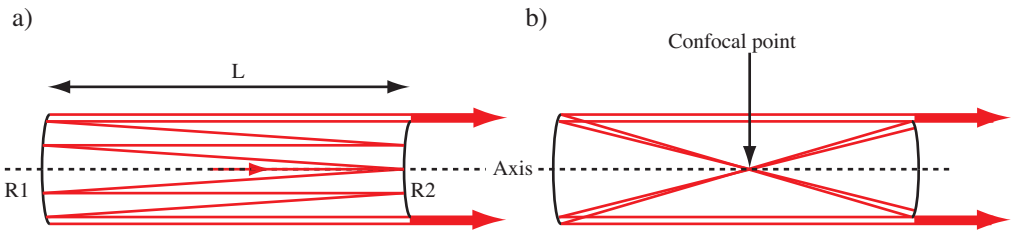

Figure 1.7 – a) Positive branch confocal unstable resonator. b) Negative branch confocal unstable resonator.

of suitable mirror curvatures to satisfy the confocal condition giving a resonator with the desired output coupling as shown by equations 1.17 and 1.18 [31] for a negative branch unstable resonator. The extra terms d_1 and d_2 represent the separation distance of each mirror to the waveguide facet, whilst L_{wg} is the length of the planar waveguide itself. Distances d_1 and d_2 have to be carefully chosen to satisfy the waveguide coupling conditions whilst still forming a confocal unstable resonator.

$$M = \left| \frac{R_2}{R_1} \right| \tag{1.15}$$

$$OC = 1 - \frac{1}{M} \tag{1.16}$$

$$R_1 = \frac{2}{M+1} \left(d_1 + d_2 + \frac{L_{wg}}{n_1} \right) \tag{1.17}$$

$$R_2 = \frac{2M}{M+1} \left(d_1 + d_2 + \frac{L_{wg}}{n_1} \right) \tag{1.18}$$

Slab shaped gain media allow the use of a one-dimensional unstable resonator which can be output coupled from only a single edge, as shown in figure 1.8. Ananev [35] has shown single-sided output coupling to create an output beam with lower divergence and better beam quality than the annular beam extracted from a double-edge coupled unstable resonator. To have a collimated output beam from a confocal unstable resonator, the length of the resonator must satisfy the confocal condition. If the resonator is either too long or too short, a converging or diverging output beam will be formed. Figure 1.9 shows a positive branch confocal unstable resonator represented by equivalent lenses for the confocal condition and both the slightly too long and too short conditions.

Bourne and Dyer [36] utilised a novel 'hybrid' resonator layout for efficiently extracting energy from a slab laser. This resonator consisted of an unstable resonator in the lateral direction combined with a stable resonator in the transverse direction. This design was improved upon by the Laser and Photonics Applications (LPA) group

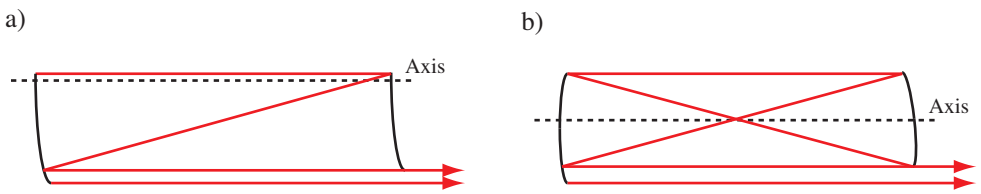

Figure 1.8 – a) Positive branch confocal unstable resonator. b) Negative branch confocal unstable resonator.

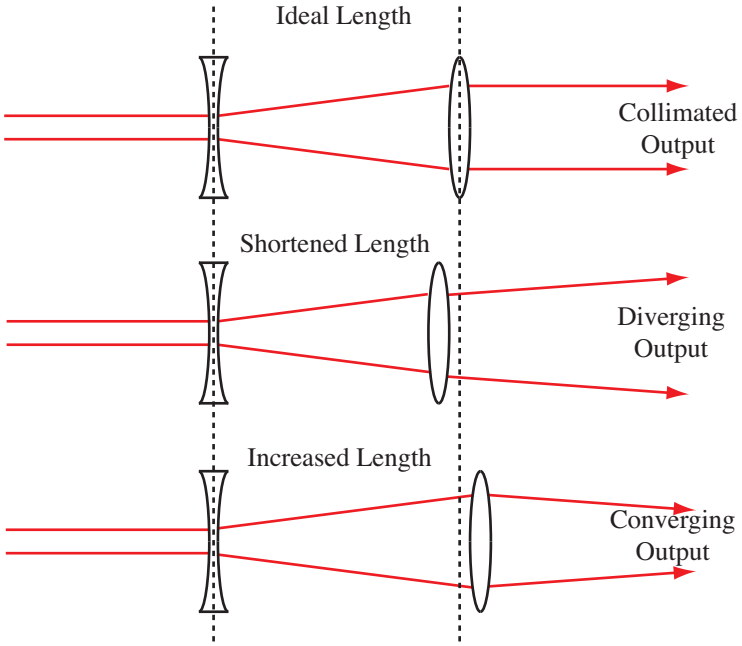

Figure 1.9 – Positive branch confocal unstable resonator represented by equivalent lenses for 3 resonator lengths, confocal, shortened and lengthened.

in 1989 [37] by utilising the guiding properties of a CO_2 planar waveguide with the waveguide coupling conditions introduced by Degnan and Hall [8] satisfied in the transverse direction. This configuration was the first demonstration of a waveguide-unstable hybrid resonator.

Lee *et al.* [13] utilised a positive branch unstable resonator with case I waveguide coupling with an Nd:YAG planar waveguide and face pumping technique described above to obtain an output power of more than 100 W when pumped at 450 W. This represented a factor of ten increase in output power for a diode-pumped solid-state planar waveguide. The laser output had beam propagation factor, M^2 of 2.3 (lateral) by 4.6 (transverse). This was later improved upon by utilising the negative branch hybrid unstable resonator shown in figure 1.10 with case II waveguide coupling at the output coupler end and case I coupling at the rear. The use of an intra-cavity transverse mode selecting slit and more tolerant lateral alignment gave excellent beam quality of $M^2 = 1.5$ in both directions maintaining more than 100 W of output power. Improvements to the pump chamber [4] which decreased the turbulence present in the water flow increased the CW output from this device to 175 W multi-mode and 125

W in single mode operation [15]. Currently, the hybrid waveguide-unstable resonator is the most efficient way of extracting high-power with good beam quality from a solid-state planar waveguide laser.

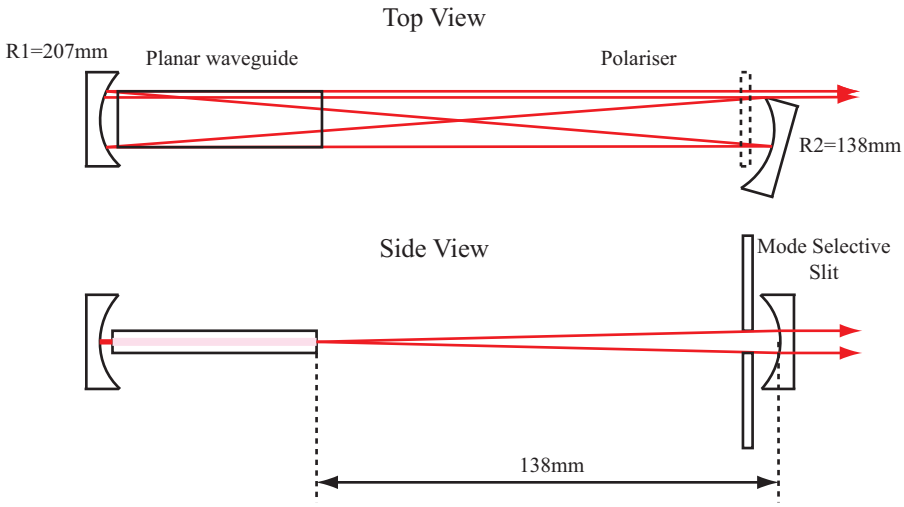

Figure 1.10 – Hybrid waveguide-unstable negative branch resonator.

MacKenzie and Clarkson [38] recently proposed a novel resonator for a Nd:YLF slab laser giving circular output. The resonator is designed so the beam is highly elliptical whilst propagating through the slab with roughly an order of magnitude change in aspect ratio to ∼1 at the output coupler, resulting in excellent overlap between the pump and laser field within the waveguide and circular output. The resonator includes two mirrors which introduce a high-degree of astigmatism to the cavity, achieving the aspect-ratio transformation. Figure 1.11 [38] shows a diagram of the optical resonator. This configuration gave an output power of 50 W with an M^2 of less than 2.

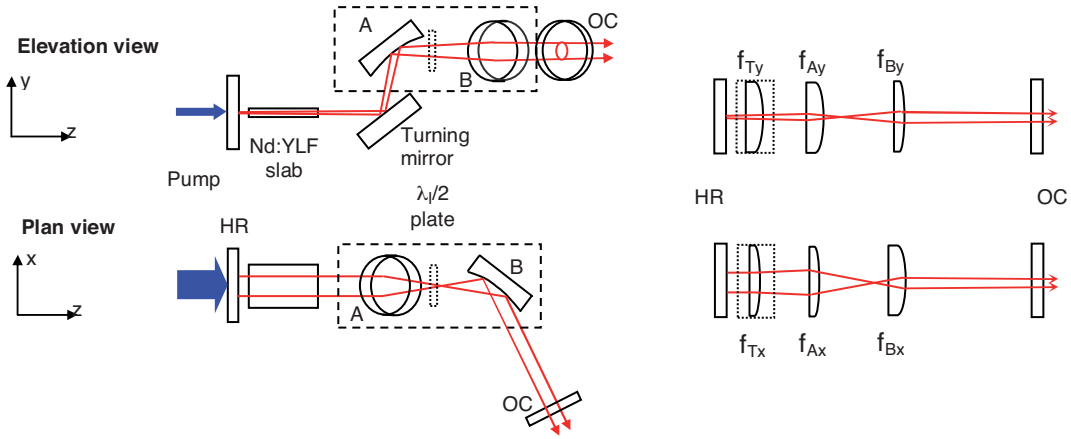

Figure 1.11 – Schematic of the highly astigmatic laser cavity, including equivalent lens diagram, resulting in a circular beam from an Nd:YLF slab laser. Figure extracted from [38].

1.5 Solid-state planar waveguide materials

Solid-state planar waveguide lasers have been produced from many different materials. Laser operation has been achieved using rare earth doped oxides such as YAG, GGG, Al_2O_3, YVO_4 and $GdVO_4$, fluorides such as YLF and LaF_2, KYW tungstate and various types of glass. These materials can be doped with rare earth ions such as Nd, Er, Tm, Yb and Ho to give a wide range of emission wavelengths. The two materials used within this thesis are Nd:YAG and Yb:YAG and are discussed in detail within this section.

Neodymium was first used as a laser ion in doped glass in 1961 [39], a few years later, a laser based on Nd:YAG was introduced in 1964 [40]. Nd:YAG lasers are available with a range of wavelengths from the visible to the infra-red, capable of operating in CW or pulsed modes with power levels ranging from the milli-watt level to the multi-kilowatt level. Nd:YAG is the most commonly used solid-state laser material due to its good combination of optical, thermal and mechanical properties and is the gain medium used within this thesis for Q-switching. Nd:YAG continues to be used in many laser systems, however, Nd:YVO_4 and Yb doped materials are beginning to see increased use over YAG due to the optical and mechanical advantages these materials have.

Nd:YAG was extremely popular in the early days of solid-state lasers due to its ease of pumping, it can be pumped by either flash lamps or diode lasers. More recently, Ytterbium doped materials are becoming popular, the simplified energy level scheme of Yb compared to Nd results in a higher quantum efficiency, with less heat generation due to quenching and upconversion as shown in figure 1.12 [41]. The energy level structure of Yb:YAG is discussed in detail in chapter 4 section 4.4.2. Yb also has the advantage of a significantly increased upper-state lifetime, resulting in greater energy storage for pulsed operation. Significant interest in the Yb doped laser materials has only developed since the 1990's due to the availability of cheap, high-power diode laser pump sources. The Yb ion operates as a quasi-3 level laser system, as such it requires intense pumping in a very narrow spectral band which would be very difficult to achieve using flash lamp pump sources. Table 1.1 shows a comparison of various key parameters for both materials adapted from Krupke's review of Ytterbium solid-state lasers [41]. Yb has a lower quantum defect of 0.11 compared to 0.24 resulting in less pump power going into the direct heating of the gain medium. The upper-state lifetime of Yb:YAG is considerably longer at 0.97 msec compared to 0.24 msec for Nd:YAG, resulting in improved energy storage which is useful for pulsed and amplifier operation. The minimum pump intensity for transparency in Yb:YAG is considerably higher at 2.8 $kWcm^{-2}$ compared to effectively 0 $kWcm^{-2}$ for Nd:YAG

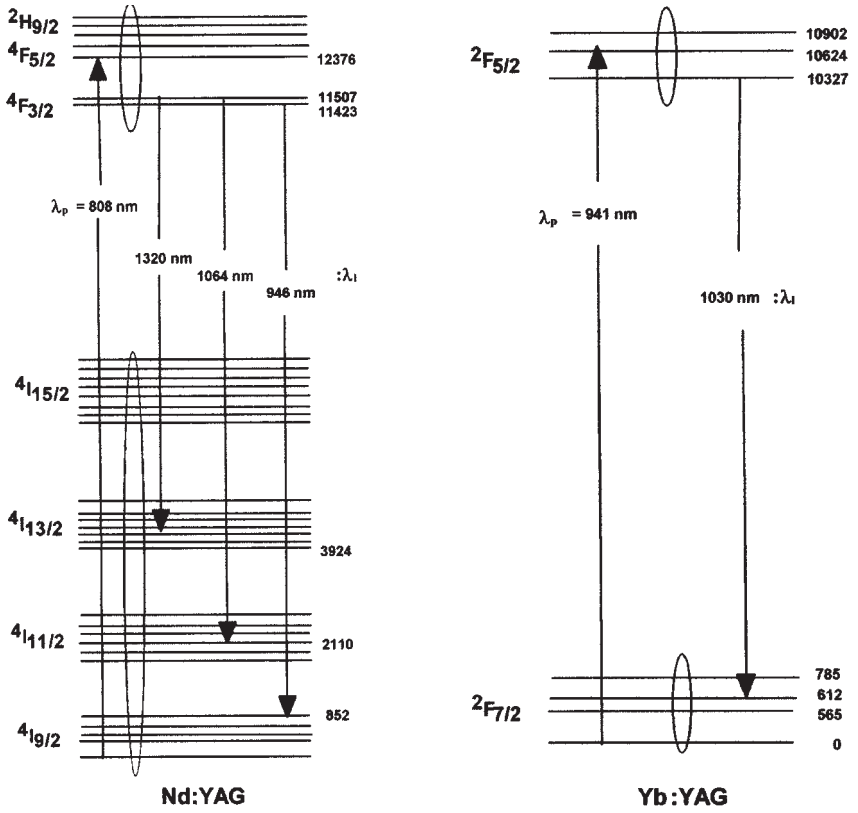

Figure 1.12 – Energy level diagrams of Nd:YAG and Yb:YAG materials. Upwards arrows represent pump transitions, whilst downwards arrows represent laser transitions [41]. Nd:YAG operates on a 4-level laser transition, whilst Yb:YAG operates with a quasi-3 level laser transition.

due to the quasi-3 level nature and ground state absorption in Yb:YAG, this means Yb:YAG requires considerably more incident pump intensity to achieve population inversion and high gain. The specific heat parameter for Nd:YAG is 3 times that of Yb:YAG, however, to achieve the same gain from both Nd:YAG and Yb:YAG, the Yb:YAG must be pumped to a population inversion that is 14 times higher than that of Nd:YAG, compensating for the laser cross-section which is 14 times lower [41]. This results in both a Nd:YAG and an Yb:YAG laser operating with the same gain having roughly the same specific waste heat value.

1.5.1 Optical Ceramics

Optical ceramics offer a promising alternative to single crystal laser gain materials. Single crystal laser materials are expensive, take considerable time to grow, and are limited in size. Transparent ceramic materials have emerged recently giving many benefits over their single crystal counterparts. Ceramics can be manufactured using a significantly cheaper process, they can be of any shape and size, high doping concentrations can be achieved and certain materials can offer very high thermal conductivity, such as Nd:Y_2O_3, which cannot be manufactured as a single crystal [42].

Parameter (units)	Nd:YAG	Yb:YAG
Pump transition wavelength (nm)	808	940
Pump transition cross-section (10^{20} cm^2)	6.7	0.7
Pump transition line-width (nm)	<4	18
Pump saturation intensity (kWcm^{-2})	12	28
Minimum pump intensity (kWcm^{-2})	∼0	2.8
Laser transition wavelength (nm)	1064	1030
Laser transition cross-section (10^{20} cm^2)	28	2.1
Laser transition line-width (nm)	∼0.6	∼6
Laser saturation fluence (Jcm^{-2})	0.6	9
Laser saturation intensity (kWcm^{-2})	2.6	9.5
Upper laser level lifetime (msec)	0.26	0.97
Quantum defect fraction	0.24	0.11
Chi (Specific heat fraction per excited state)	0.37	0.11
Specific waste heat @ 0.05 cm^{-1} gain (Wcm^{-3})	51	55

Table 1.1 – Comparison of key parameters for Nd:YAG and Yb:YAG laser gain materials [41].

The first group to fabricate a transparent, polycrystalline YAG material using a solid-state reaction method, was the Ikeuse group in Japan, demonstrating the first laser operation from a ceramic gain medium giving an output power of 70 mW [43]. However, fabrication using this method resulted in low quality, small samples with high scattering losses. More recently, Konoshima Chemical Company Ltd. [44] developed a vacuum-sintering manufacture technique which involves a liquid-phase chemical reaction to produce the nano particles found in the ceramic. Homogeneous nano particles greatly reduced the scattering losses within the ceramic materials with the manufacturing process being scaled up to 1x1 m^2 with a thickness of less than 2 cm. Ueda *et al.* have demonstrated a 1.46 kW ceramic laser [45] and developed Nd:YAG slabs with ceramic Sm:YAG claddings formed during the sintering process which absorb at 1064 nm, limiting parasitic oscillation and ASE within the slab [46]. Utilising 5 of these Sm:YAG clad Nd:YAG slabs, Lawrence Livermore National Laboratory in the University of California have built a pulsed laser with an average power of 67 kW [47]. Ceramic materials are now readily available commercially from the Konoshima Chemical Company [44], offering ceramic YAG doped with a range of active ions such as Nd^{3+}, Yb^{3+}, Er^{3+}, Sm^{3+} and Cr^{3+}. Using a bonding technique, performed during sintering, it is possible that cheap, large-scale ceramic solid-state planar waveguides will become a possibility.

1.6 Pulsed Lasers

Pulsed lasers are important for many laser applications, such as laser communications, ranging, drilling and micro-machining. There are many methods used to obtain laser pulses, with bulk (rod, thin disc, slab and planar waveguide) solid-state lasers most commonly used for high pulse energies. This is due to the large cross-section allowing for high energy storage compared to that of a typical fibre laser which are limited to the low pulse energy regime. Generating high energy pulses in the near IR and visible part of the spectrum is typically done by Q-switching doped YAG materials with visible emission obtained through frequency doubling, Q-switched pulse duration is typically in the 10 to 100 ns regime with pulse energies ranging from millijoules up to the joule range. Nanosecond pulses in the UV can be obtained using Excimer lasers. There is increasing interest in shorter pulses in the femtosecond and picosecond regime, this is due to the laser material interaction time being extremely short, resulting in a very small heat affected zone and very precise machining. To obtain very short pulses, mode-locking is used, which can be performed on many laser types such as bulk solid-state, fibre, or semiconductor lasers. Mode-locking achieves very short pulses with low pulse energies, to obtain higher pulse energies systems such as regenerative amplifiers and cavity-dumping are used.

1.6.1 Q-switching

Q-switching was first demonstrated in 1962 by Hellwarth and McClung [48] and later theorised by Wagner and Lengyel in 1963 [49]. Q-switching is the process of misaligning the resonator temporarily, effectively destroying the Q of the cavity with an intra-cavity element whilst pumping the gain medium. This causes the gain medium to store the pump energy in the upper state without lasing. The cavity is then suddenly realigned by adjusting the intra-cavity element and the laser emits a giant short pulse of laser radiation [50].

Q-switching can be achieved through a number of methods, both passive and active. Passive methods include using an intra-cavity saturable absorber, which causes Q-switching once the intra-cavity radiation levels reach a high enough level to make the saturable absorber bleach, allowing radiation to oscillate around the resonator building up the pulse. Passive Q-switching of a planar waveguide laser has been demonstrated by MacKenzie and Shepherd [51], in which a double-clad Yb:YAG planar waveguide had a short section of Cr:YAG saturable absorbing material bonded within the structure of the waveguide, giving an average power of 2.3 W, with 30 μJ pulse energy at a repetition rate of 77 kHz. The most common methods of active Q-switching are the use of an acousto-optic modulator (AOM) or an electro-optic

modulator (EOM), such as a crystal which becomes birefringent when an electric field is applied. The AOM is generally used when high repetition rates of >10kHz are required of the Q-switched laser, whilst EOMs tend to be used when a faster switching speed is required, however, EOMs are limited in size due to the high voltages required to drive the modulator resulting in the need to use AOMs for large apertured lasers such as kW class industrial Nd:YAG rod lasers.

1.6.2 Mode-Locking

Mode-locking is used to produce ultra-short optical pulses which cannot be achieved through the use of Q-switching which is limited to the ns regime. Pulses as short as as 1.6 fs [52] after external cavity compression have been achieved using mode-locking techniques. Mode-locking is achieved through the combination of several in-phase longitudinal laser modes. By combining these in-phase modes, the temporal intensity profile of the summation of multiple modes has a repetitive pulsed nature. The larger the gain bandwidth, the more modes can be phase-locked resulting in a shorter optical pulse. Many techniques have been developed to achieve mode-locking, the simplest is the use of an intra-cavity shutter which opens at regular intervals timed such that the electric field of all modes is at a maximum intensity simultaneously, ensuring the pulses are in-phase. The cavity length is adjusted such that the round-trip time matches the temporal separation of the mode-locked pulses. Both active and passive techniques are utilised. Active methods use AOMs or synchronous pumping whilst passive techniques involve Kerr lens mode locking and semiconductor saturable absorbers. Mode locking has been achieved in a number of waveguide lasers such as Nd:$LiNbO_3$ [53], Ti:Er:$LiNbO_3$ [54], and Er doped Phosphate glass [55].

1.7 Overview of modern solid-state laser geometries

This section gives a brief overview of two solid-state laser geometries which compete with the planar waveguide format. Both are motivated by the need to improve the thermal properties of the solid-state laser, enabling power scaling without thermal effects causing complications.

1.7.1 Thin Disc Lasers

The modern thin disc laser was first developed by Giesen [56] in 1994. The geometry of a thin disc laser requires the thickness of the gain medium to be less than the diameter of the laser mode, one face of the disc is bonded directly to a heatsink, offering excellent thermal management. An HR dielectric mirror is also coated onto

this surface creating the plane rear resonator mirror. This configuration is often referred to as an 'active mirror' [57] due to it effectively being a mirror with gain. The thickness of an Yb:YAG thin disc is typically in the 100-200 μm range resulting in a small temperature rise for a given dissipated power. The heat flows directly into the heat sink resulting in temperature gradients perpendicular to the disc surface resulting in minimal beam distortion due to thermal effects. Pumping is achieved through the face opposite the HR mirror, and is typically performed in a multi-pass configuration to increase the effective length of the disc resulting in better pump absorption. The thickness of a typical Yb:YAG thin-disc laser is comparable to the core height of the Yb:YAG planar waveguide reported within this thesis.

The thin disc laser configuration has excellent power scalability, either by utilising multiple discs in a single resonator or by increasing the pump spot size whilst maintaining the pump power density. Thin disc lasers are commercially available with 4 kW CW average power from a single disc and 16 kW from multiple discs [10]. Recently, Boeing have demonstrated a thin disc laser system operating at more than 25 kW with nearly diffraction limited beam quality demonstrating future scalability towards 100 kW [58]. Further power scaling is possible, however, ASE needs to be suppressed within the disc. Many thin disc lasers now operate with an anti-ASE cap bonded to the upper AR surface of the disc, this cap couples the ASE from the gain region, preventing it from being trapped by total internal reflection, clamping the gain [59]. Current power scaling theory predicts the ability to obtain more than 10 kW CW per disc with pulsed operation giving energies of more than 1 J [60]. Thin disc lasers also operate well when pulsed, with a high power mode-locked thin disc laser recently being demonstrated with an average output power of 76 W, producing 25.9 μJ pulse energy and 928 fs pulse duration [61].

1.7.2 Fibre Lasers

One of the first lasers demonstrated was a simple form of fibre laser [39], consisting of a 1 m long Nd:glass rod clad with undoped glass allowing waveguiding to take place. Advances in the manufacture of low-loss optical fibres lead to efficient rare-earth doped single mode fibres and advances in efficient diode pump sources have driven the development of fibre lasers. Fibre lasers consist of a doped core region with a lower refractive index cladding creating an optical fibre with gain, a resonator is commonly formed by either coating the ends of the fibre or using external mirrors, fibre Bragg gratings can also be used as reflectors integrated into the fibre. Increased pump efficiency can be obtained by utilising a double-clad structure with one core giving optical gain whilst the second core guides the pump light [62, 63]. Pump absorption is typically greater than 90% as the length of the fibre can be increased

until all pump light is absorbed.

Fibre lasers are extremely good high-power CW lasers with 50 kW CW lasers available commercially [64], they also make good amplifiers due to the long gain length that can be obtained. High-power is obtained due to the high surface-to-volume ratio, offering excellent cooling of the active area and the waveguiding effect avoiding aberrations due to thermal gradients.

There are a number of issues with fibre lasers compared to bulk solid-state lasers, these include uncontrolled birefringence, in which the temperature of the fibre must be carefully controlled otherwise polarisation controllers must be adjusted with changing temperature [65]. Fibre lasers are not suitable for producing high-peak power due to the small volume available for energy storage compared to a bulk solid-state laser, they can, however, be used very effectively as pulsed laser amplifiers due to the long gain length available. Planar waveguide lasers offer an advantage over fibre lasers in the pulsed regime due to the greater active volume and stored energy available.

Chapter 2

Active Q-Switching of an Nd:YAG Planar Waveguide Laser

2.1 Introduction

This chapter discusses active Q-switching of an Nd:YAG planar waveguide laser. Utilising an acousto-optic modulator (AOM) and hybrid negative-branch unstable resonator allows the planar waveguide geometry to be Q-switched. Many applications require a good quality beam, with an average power in the 100 W range with pulsed operation resulting in the ability to laser process materials at a faster rate. Examples of these applications include high-speed marking, non-linear optics and laser radar, all of which require pulses in the $5 - 50$ ns regime. The Nd:YAG large core planar waveguide laser has been shown to be a good method for achieving a good beam quality, high power laser [13]. This chapter looks at extending its operation from CW into the Q-switching regime.

The results reported within this chapter were taken in conjunction with other members of the Laser and Photonics Applications Group of Heriot Watt University. Prof. J. Xu, a former Research Associate within the group incorporated the acousto-optic modulator (AOM) into the resonator design, determining that the AOM may be placed in two different intra-cavity positions, one providing better diffraction efficiency, the other providing better optical switching speed. Mr. Adam Russell modified the pump chamber used to house and pump the Nd:YAG planar waveguide, improving the CW laser output to 175 W due to improved water flow allowing for better cooling and providing more homogeneous pump distribution. Prof. Howard Baker performed theoretical modelling work, determining theoretical pulse build up time and the maximum gain allowed before the onset of prelasing. The experimental results obtained and the analysis of these results reported within this chapter arise from work conducted by the author with the help of Dr. Jesus Valera, a former Research Associate within the group. The work presented within this chapter has also resulted

in a publication in the IEEE Journal of Selected Topics in Quantum Electronics [15].

2.2 Laser Configuration

This section discusses the characteristics of the planar waveguide used, the diode pumping scheme and the design of the resonator, allowing for the incorporation of an intra-cavity AOM, to provide active modulation of the cavity Q factor.

2.2.1 Waveguide Characteristics and Pumping Configuration

The planar waveguide used comprises of 1% doped Nd:YAG core region surrounded by undoped YAG cladding regions. The dimensions of the entire waveguide device are 63 mm x 1 mm x 11 mm with a waveguide core thickness of 200μm and 400μm thick claddings. The active region is thus a large-core, low numerical aperture (NA), multimode waveguide for the transverse direction and a large area free-space section in the lateral direction. All faces of the waveguide are precision optically polished to $\frac{\lambda}{10}$ surface quality. The planar waveguide was manufactured by Onyx Optics [21] using a contact bonding technique, discussed in the previous chapter.

The pumping for this structure has been reported previously [12, 13, 66] and is described in detail in chapter 1 and reference [13]. The waveguide is face pumped with the pump unit comprising of a 10-bar diode stack giving a total output power of 430 W at 808 nm. The multi-pass pumping is achieved by placing the waveguide structure between two plane-parallel high reflective dielectric-coated mirrors at 808 nm. The non-collimated diode light is inserted into this chamber through 10 slots of $\sim$200 μm width in the mirror adjacent to the diode stack. This pump chamber also incorporates direct water cooling to the waveguide surface by lateral flow between two silica windows within the chamber. The combination of this planar waveguide with face pumping has previously been demonstrated to produce 175 W in low-order multimode CW operation and 120 W with an M^2 of 1.3 in the transverse direction by 1.5 in the lateral direction when pumped by 430 W of diode pump light with the output only limited by available pump power [67].

2.2.2 Resonator Configuration

The resonator used for this work consists of a hybrid negative branch unstable resonator, and is based on the resonator developed by Lee and Baker [28, 68]. The modified resonator layout was introduced by Xu, allowing the introduction of an AOM and complimentary polariser into the resonator. The resonator mirrors consists of an R= 207 mm spherical rear mirror placed 1.5mm from the waveguide facet

Length	Distance (mm)
L1	0.5
L2	63 ($n = 1.82$)
L3	22
L4	52
L5	35
L6	See text
L7	Variable, see text

Table 2.1 – Intra-cavity component separations, for cavity configuration A) as shown in figure 2.1.

and an R= 138 mm spherical output coupler with single edged output coupling placed 149.4 mm from the waveguide facet accounting for the additional optical length caused by placing an AOM and polariser within the cavity. This creates near case 1 waveguide coupling with the rear mirror and case 2 waveguide coupling for the output coupling mirror, with a negative branch unstable resonator, magnification M= 1.5, in the unguided direction. The distances between components and the cavity configuration can be seen in table 2.1 and figure 2.1. An adjustable slit can also be introduced near the output coupler to offer mode selectivity in the waveguide direction.

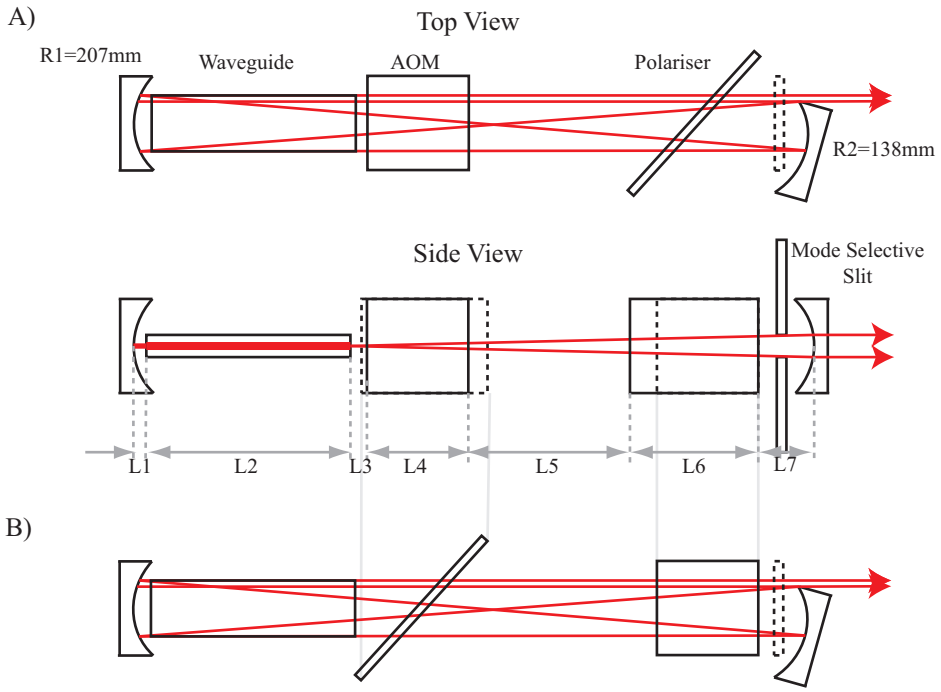

Figure 2.1 – A) Resonator configuration for maximum switching speed with silica in the high intensity region and B) Configuration for maximum diffraction efficiency with the polarisers dielectric coating in the high intensity region.

An AOM is used for Q-switching due to its adequate switching time, large aper-

ture and high damage threshold. Ideally, an EOM would be used due to its faster switching time, however, at the time of writing there were no EOM's available with a sufficiently large aperture of at least 11 mm to work with the planar waveguide device. Xu [69] showed that the Gooch and Housego QS-12C model compressional acoustic mode AOM has two placement options, either A) near the waveguide facet, or B) the conventional position near the output coupler, the placement of the AOM and its complimentary polariser must be such that that no dielectric optical coatings are within the intra-cavity cross over point of the negative branch unstable resonator due to the high intensity created in this region risking optical damage. With the AOM in position A, the laser mode of average width 0.4 mm interacts with only 2 ultrasound wavelengths giving an acoustic transit time of 67 ns. Position B gives a larger beam interacting with the ultrasound but a slower acoustic transit time of 0.3 μs, as shown in figure 2.2. The AOM is designed to have maximum diffraction efficiency on the TE polarisation, as such the resonator has only been aligned to operate in this mode. The AOM is driven using a 100 W 27 MHz RF driver.

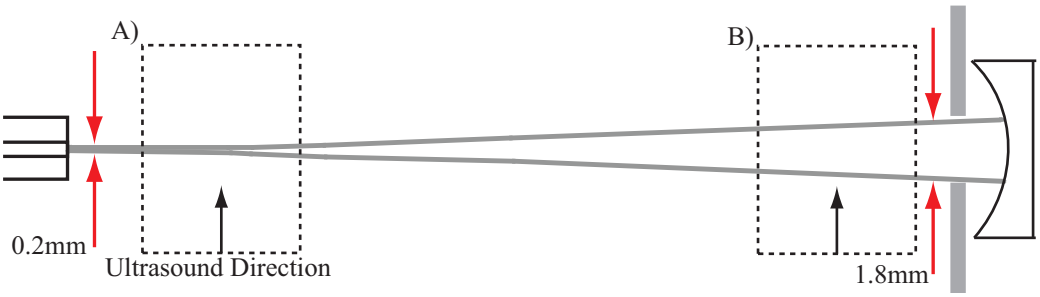

Figure 2.2 – Intra-cavity beam size as it expands leaving the waveguide, the dotted box represents the two AOM positions. Position A) acts on a beam of diameter 0.4 mm with an acoustic transit time of 67 ns, Position B) acts on a much larger beam with an acoustic transit time of 0.3 μs.

The polariser within the cavity must be rotated to its optimum transmission angle α within the resonator to minimise loss. However, this introduces an astigmatic effect to the confocal unstable resonator and the case II waveguide condition. The polariser has thickness t=3.8 mm and refractive index, $n_p = 1.51$. The internal angle is given by equation 2.1, modifying the physical length of the resonator, L_c, given by equation 2.2.

$$\beta = sin^{-1}\left(\frac{sin(\alpha)}{n_p}\right) = 34.59° \tag{2.1}$$

$$L_c = L_1 + L_2 + L_3 + L_4 + L_5 + t \cdot \frac{cos(\alpha - \beta)}{cos(\beta)} + L_7 \tag{2.2}$$

Where $L_{1...7}$ are shown in table 2.1. This gives a cavity length of L_c =215.14 mm. Using Siegmans off-axis ray transfer matrices [31] gives two matrices for the polariser,

one in the lateral direction and one in the transverse direction, P_L and P_T given by equations 2.3 and 2.4.

$$P_L = \begin{pmatrix} \frac{cos(\alpha)}{cos(\beta)} & 0 \\ 0 & \frac{cos(\beta)}{cos(\alpha)} \end{pmatrix} \begin{pmatrix} 1 & \frac{L_6}{n_p} \\ 0 & 1 \end{pmatrix} \begin{pmatrix} \frac{cos(\beta)}{cos(\alpha)} & 0 \\ 0 & \frac{cos(\alpha)}{cos(\beta)} \end{pmatrix} \tag{2.3}$$

$$P_T = \begin{pmatrix} 1 & 0 \\ 0 & 1 \end{pmatrix} \begin{pmatrix} 1 & \frac{L_6}{n_p} \\ 0 & 1 \end{pmatrix} \begin{pmatrix} 1 & 0 \\ 0 & 1 \end{pmatrix} \tag{2.4}$$

This gives two effective intra-cavity lengths for the polariser, the lateral 'length', P_L =1.196 mm which shortens the physical optical length and the transverse 'length', P_T =3.057 mm which lengthens the physical optical length. This means that the polariser prevents the resonator from being both confocal in the lateral direction and case II in the transverse direction at the same time. The ideal confocal length gives L_7 =38.14 mm whereas the ideal concentric length (Case II) gives L_7 =36.43 mm. The ideal concentric case gives lower loss and is the ideal position to operate in, however, the shorter cavity length will cause the unstable resonators lateral output beam to diverge as discussed in chapter 1. Siegman's geometric unstable resonator model [31] allows the radius of curvature of the wavefront leaving the resonator to be calculated from the round-trip propagation matrix of the unstable resonator using equation 2.5, where M is the magnification of the unstable resonator.

$$L_7 \cdot C^2 + (M + \frac{1}{M}) \cdot C = 0 \tag{2.5}$$

Setting L_7 to the ideal concentric length gives a lateral output beam with a wavefront curvature of 4 m. By performing a simple ray trace of the cavity, the angles of the rays at the extreme edges of the lateral waveguide were calculated, showing the edge rays to have an angle of 0.059°, resulting in a reduction of fill factor of ∼0.0001%. Therefore the resonator is best operated in the minimal loss concentric condition causing a slightly diverging output beam in the lateral direction.

2.3 AOM Characteristics

This section develops an out of cavity method of characterising the AOM. Both the diffraction efficiency and switching speed of the AOM for both resonator configurations is studied to determine the optimal AOM position for efficient Q-switching. Utilising a low power Nd:YAG laser, the fundamental waveguide mode is simulated and studied in both the temporal and spatial domains after a double pass through the AOM.

2.3.1 Experimental configuration

The Elforlite laser used for these experiments is a 200 mW CW Nd:YVO_4 laser emitting at 1064 nm. An optical isolator was used to ensure that any back reflected light would not re-enter the laser aperture and cause it to become unstable in either the temporal or spatial domain. A $\frac{\lambda}{2}$ plate was used in combination with a polarising cube to allow the polarisation and power of the laser to be controlled.

The beam from the laser was focussed using an f= 150mm lens, allowing the M^2 of the laser to be measured. The M^2 was measured by imaging the laser spot on a diffusive screen at various points through the beam waist and the M^2 calculated by measuring the size of the beam at these points and a graph of beam width against distance plotted. By fitting equation 2.6 to this curve, the M^2 of the laser can be found.

$$\omega(z)^2 = \omega_0 + \sqrt{M^2 \frac{\lambda^2}{\pi^2 \omega_0^2}(z - z_0)^2} \tag{2.6}$$

Where $\omega(z)$ is the beam size at position z, w_0 is the size of the beam at the waist and λ is the wavelength of the laser, in this case 1064 nm. By fitting equation 2.6 to the data obtained for the size of the beam at distance z from the lens the M^2 of the laser is obtained as $M^2 = 1.5$ as shown in figure 2.3. An error is introduced into this measurement due to the small spot size at the beam waist. Spots of this size are approaching the instrumentation limit of the CCD camera where 1 pixel images approximately 10 μm. Small spot sizes have a tendency to 'bleed' into adjacent pixels, increasing the apparent size of the laser spot. Manufacturer data states this laser to have an M^2 value of 1.1. However, measuring an M^2 this low is very difficult as the beam quality in the experiment is limited by the quality of the focussing lens used to measure the M^2.

The beam waist created by the lens is designed to create a waist equivalent to the size of the waveguide mode leaving the waveguide facet. The sinusoidal fundamental waveguide mode is a close approximation to a Gaussian beam with a width of 100 μm. By adjusting the lens position it was possible to obtain a beam waist closely approximating the fundamental waveguide mode with a beam profile as shown in figure 2.4 and waist size shown in figure 2.3.

Double Pass Attenuation and Switching Speed Measurements

All measurements in this section were taken with the RF power to the AOM at 100 W. Using the Elforlite laser, a low power, close approximation to the fundamental waveguide mode has been created which can be used as a tool to examine the properties of the AOM. A 200 μm slit was placed at the beam waist to simulate the waveguide

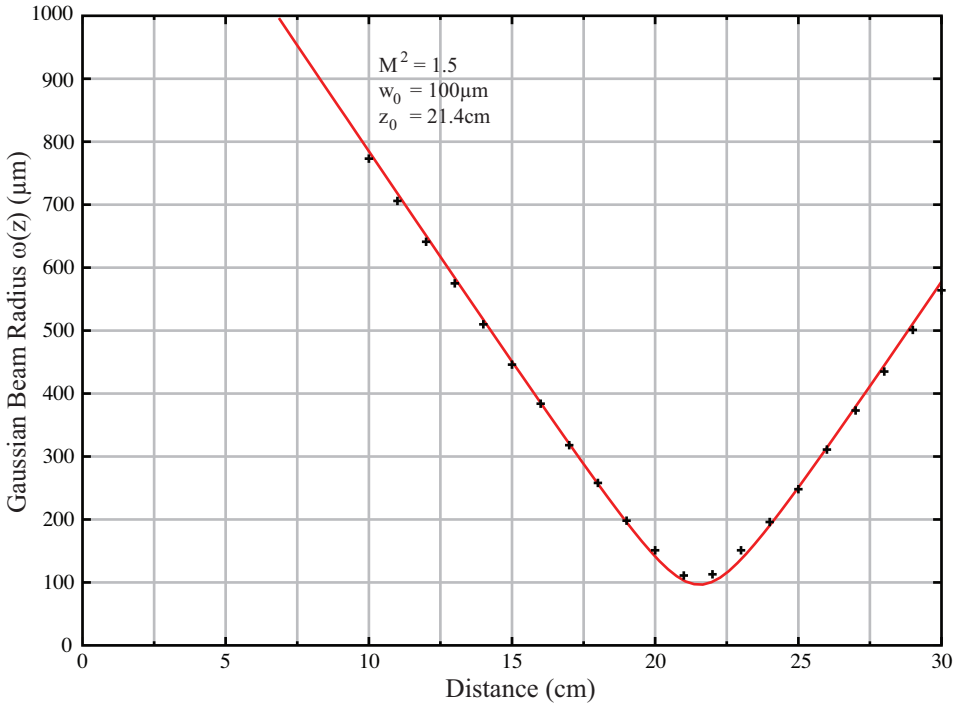

Figure 2.3 – Beam size against distance from the focussing lens. Equation 2.6 is fitted to this data giving an M^2 of 1.5 in the transverse (waveguide) direction.

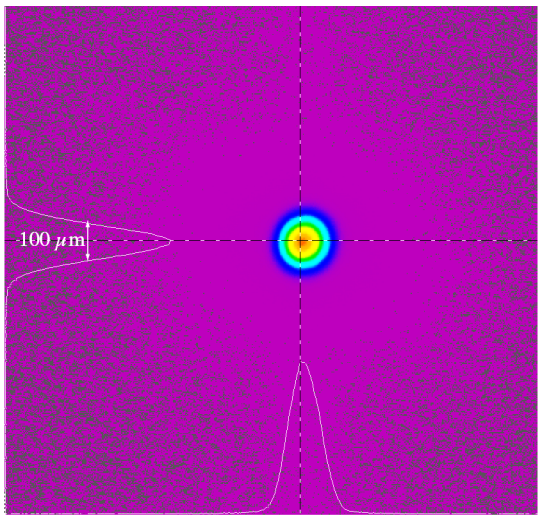

Figure 2.4 – Beam profile of the Elforlite laser at the beam waist.

facet, the AOM was then placed at a distance from the slit equivalent to its distance from the waveguide facet for both resonators A) and B). This configuration allows double pass attenuation and switching speed measurements through the AOM to be carried out. This was achieved by placing the resonator output coupler, HR coated at 1064 nm with a curvature of R=138 mm at a distance of 149.4 mm from the slit, the mirror was aligned so the beam returned through the 200 μm slit. A 50/50 beam splitter deflects the reflected beam through an imaging lens and onto a rotating disk. A camera is focussed on the rotating disc, which images the returned mode at the slit plane allowing the profile of the returned beam to be measured, by replacing the

camera with the fast InGaAs photodiode the switching speed is measured. The double pass experimental configuration can be seen in figure 2.5.

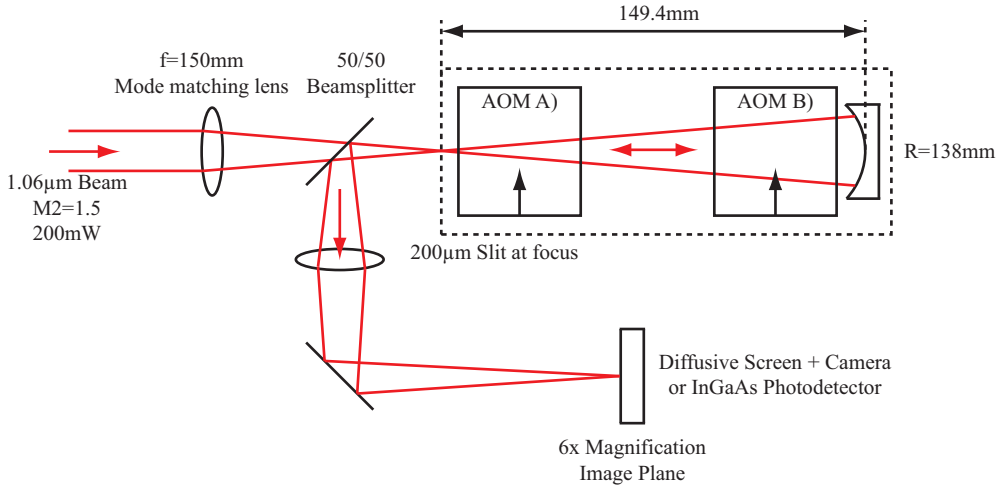

Figure 2.5 – Experimental configuration for double pass measurements of the AOM with both resonator configurations.

2.3.2 AOM Attenuation and Uniformity

Resonator A

With the AOM in the position required for resonator A, figure 2.6 shows the beam profile obtained with Spiricon beam profiling software, the transverse direction data from Spiricon was then exported and plotted in figure 2.7 with the Waveguide core size overlaid on the graph. With the modulator in this position it can be seen that diffraction does occur, however, the effect is not strong enough to clearly separate the different orders with approximately 15% of the beam still returning to the waveguide core. This experiment was then repeated with a varying modulator angle with respect to the incident laser and the feedback into the waveguide core recorded, the results of this can be seen in figure 2.8. As can be seen from this graph, the minimum feedback occurs with the AOM at 0° after two diffraction events, one in the forward direction and one with reverse propagation.

Resonator B

The same experiments were carried out with the modulator set up to simulate resonator B, the results of this can be seen in figures 2.9 and 2.10. With the modulator in this position, the beam passing through it is larger, therefore interacting with more of the ultrasound within the modulator giving clear separation of the diffraction orders, however, the feedback into the waveguide core remains the same at approximately 15%.

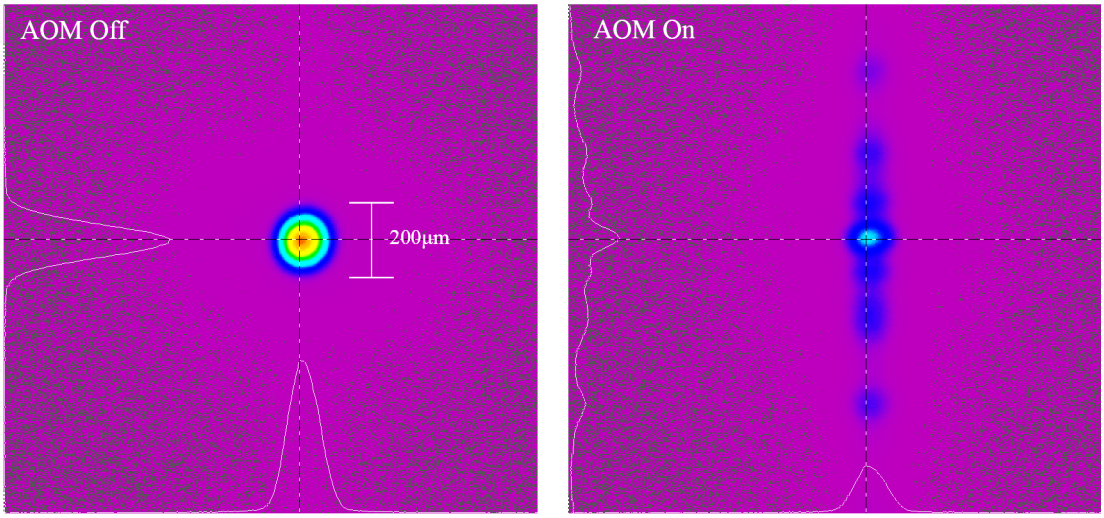

Figure 2.6 – Beam profile returning to the slit after a double pass through the AOM with the RF signal both off and on with the AOM in position A, close to the waveguide facet.

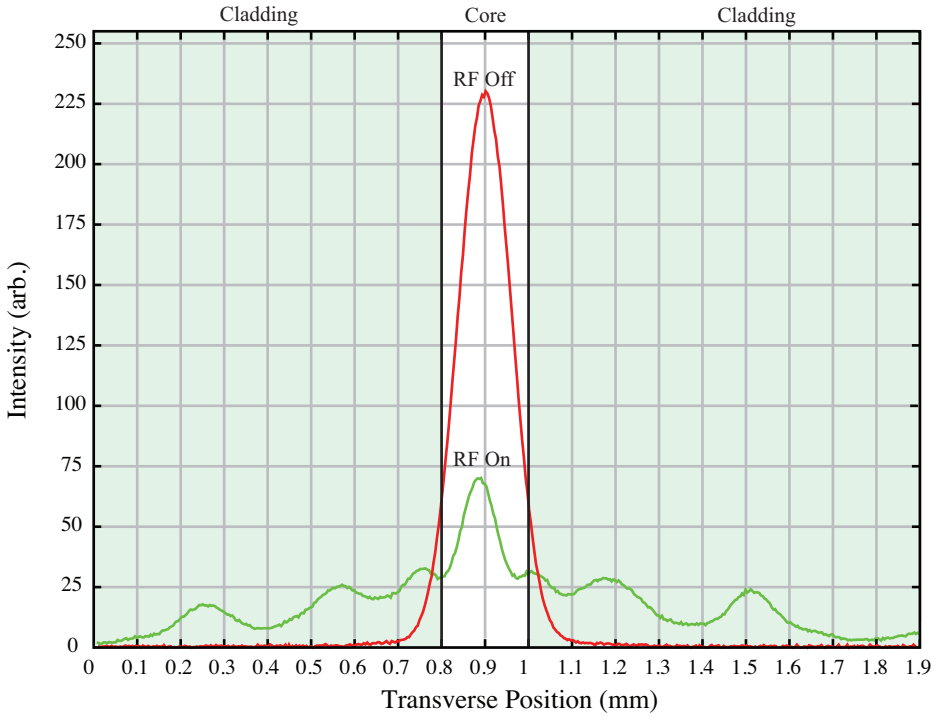

Figure 2.7 – Transverse beam profile returning to the waveguide facet after a double pass through the AOM in position A, the shaded region represents the cladding region of the waveguide.

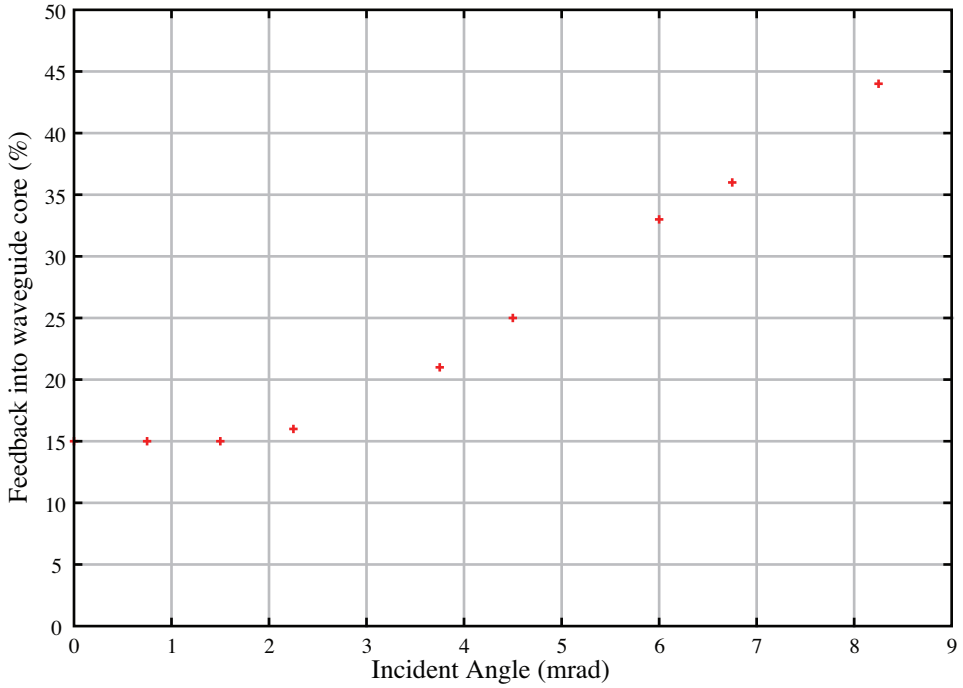

Figure 2.8 – Feedback into the waveguide core after a double pass through the AOM set at various angles.

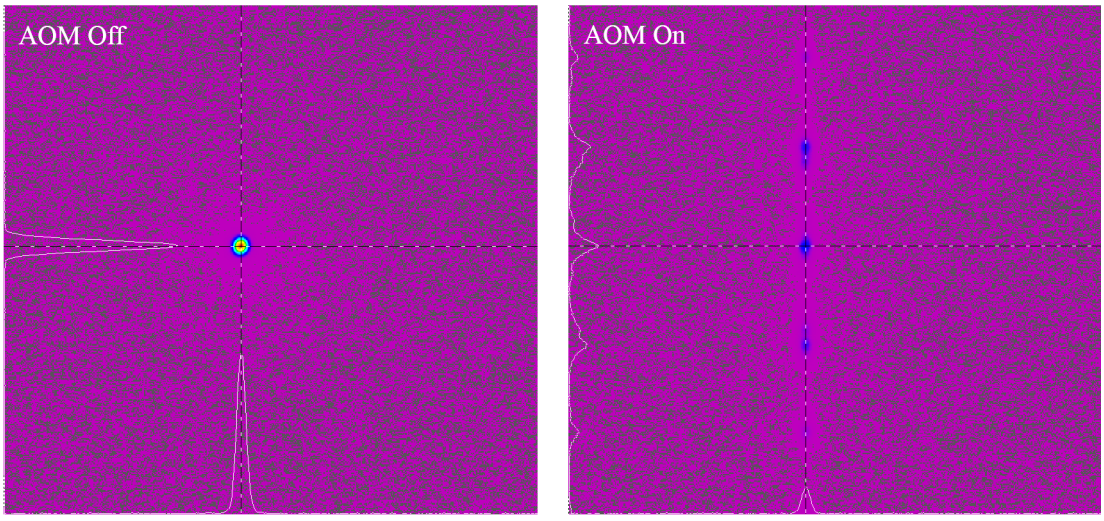

Figure 2.9 – Beam profile returning to the slit after a double pass through the AOM with the RF signal both on and off with the AOM in position B, close to the output coupling mirror.

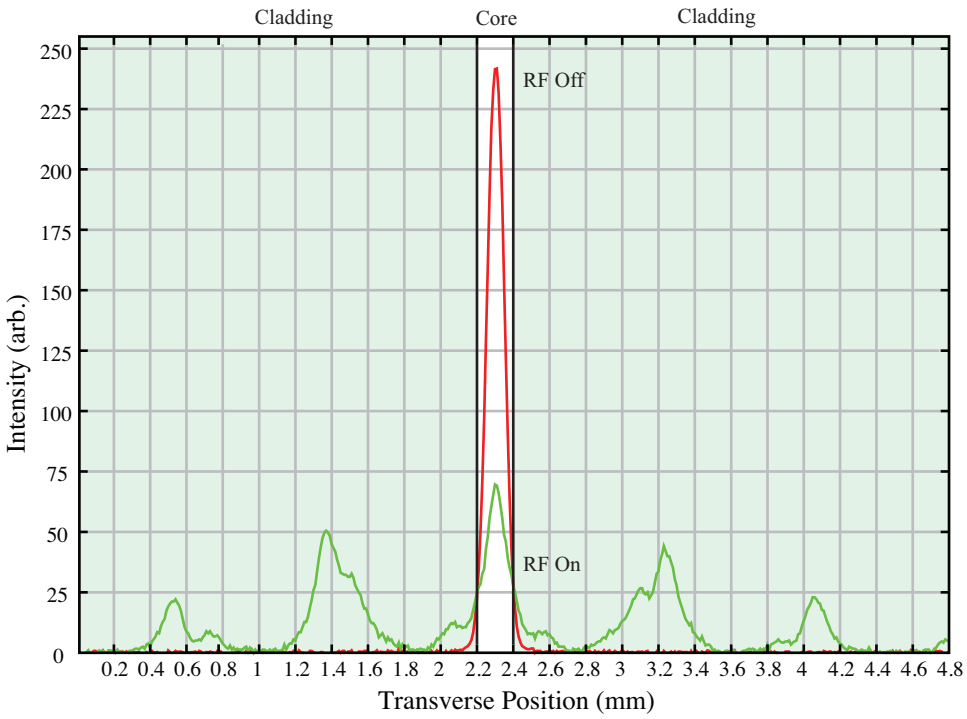

Figure 2.10 – Transverse beam profile returning to the waveguide facet after a double pass through the AOM in position B, the shaded region represents the cladding region of the waveguide.

Ultrasound Uniformity

The uniformity of the ultrasound within the AOM in the lateral direction was measured by translating the modulator across the Elforlite beam. The intensity incident on a diffusive screen over the area equivalent to the height of the waveguide core was measured using Spiricon beam profiling software. The results of this experiment can be seen in figure 2.11. These results show that only the central 10 mm of the modulator is active, with a transmission efficiency of $\sim 20\%$. This is due to the structure of the AOM, the piezo transducer is positioned in the centre of the modulator and the ultrasound radiates outwards from this position resulting in poor diffraction efficiency at the edges of the device.

2.3.3 Double Pass AOM Switching Speed

The switching speed of the AOM was measured using a fast InGaAs photodiode connected to an oscilloscope giving a 1 ns response time. Measurements were taken with the AOM in both position A) and position B). Figure 2.12 shows the photodetector response to the AOM switching, this shows that position A) is faster than position B) with a 10-90% rise time of 100 ns compared to 500 ns for position B). The rise time is measured by modelling the switching curve as 3 intersecting straight lines and measuring the 10-90% rise time of this line. Modulation of the detector signal at 27MHz

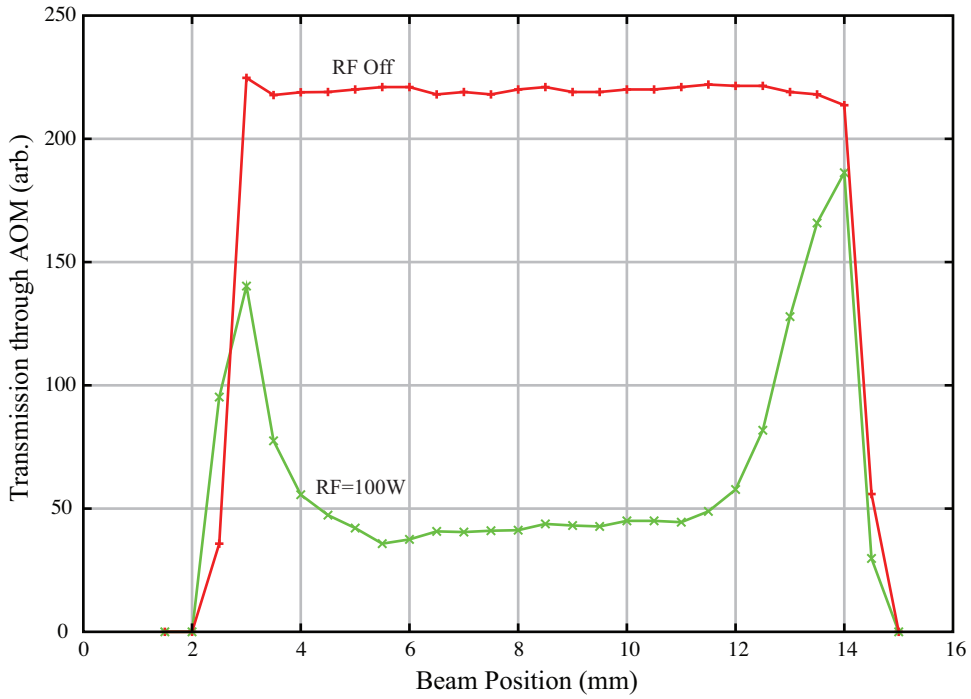

Figure 2.11 – AOM transmission as a function of lateral position through the modulator input face.

with the AOM in position A) can be seen when the RF is on, this is due to beating between the fundamental mode and the diffracted beam because of the lower separation of the diffracted orders with the modulator in this position, this is confirmed by the modulation not being present when the modulator is in position B) where greater diffraction efficiency prevents overlap between the diffracted modes. The RF cut off time was also measured as shown in figure 2.12 giving a fast ultrasound dissipation of 70 ns.

2.3.4 AOM Placement within the Resonator

The results in this section have shown position A) to be better for a fast switching speed, essential for a high gain Q-switched laser due to the short pulse build-up time, however, this position does not give good diffraction efficiency with 15% of the modulated beam still returning into the waveguide. There is no need for greater diffraction efficiency as the returned profile does not efficiently couple into the fundamental mode, either entering the claddings as loss or exciting higher order waveguide modes which are suppressed by the intra-cavity slit. Position B) provides similar diffraction efficiency but slow switching. From these results, it was decided configuration A) should be used due to the faster switching speed.

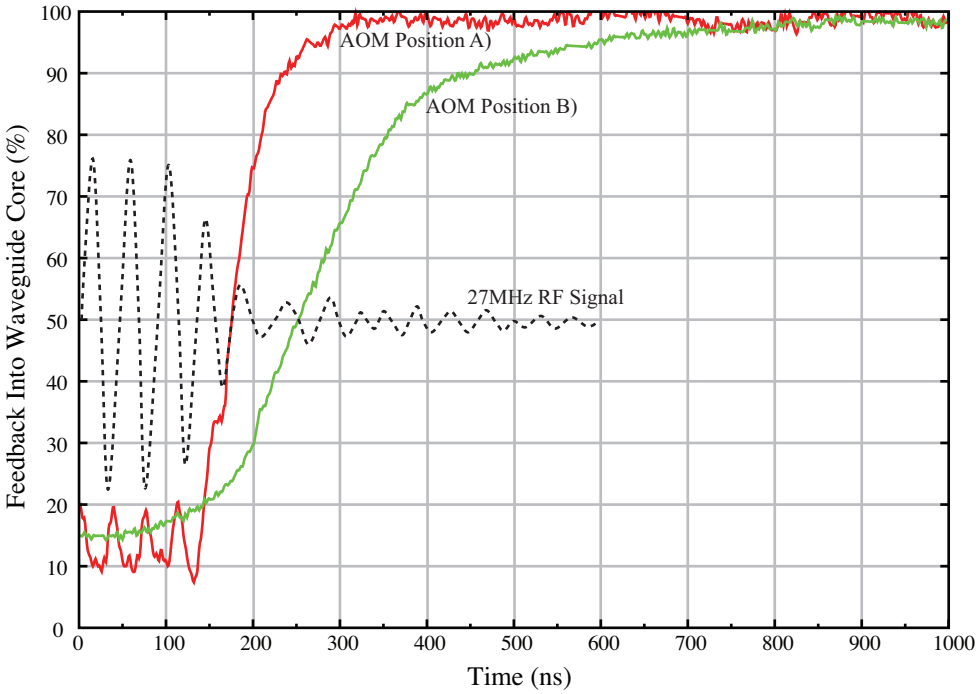

Figure 2.12 – Optical feedback to the waveguide core when the RF is turned off for both resonator positions. The RF signal is represented by the dotted black line with an arbitary y-axis. Beating can be seen for position A) during the time the RF is on due to the lack of separation of diffraction orders, this position gives a switching speed of 100 ns. Position B) has no beating due to clear separation of diffraction orders.

2.4 Pulse Build Up

Due to the high gain within the Nd:YAG planar waveguide, pulse build-up time is short which can risk the pulse interacting with the slowly dissipating ultrasonic wave due to the slow, ∼70 ns, RF switch off within the AOM. This can cause double-pulsing and pulse modulation effects such as broadening. The high-gain can also cause pre-lasing, which occurs when the intra-cavity losses due to the AOM are not sufficient to hold-off CW lasing, resulting in a pulsed laser with significant CW background noise. This section presents the results of a model determining the Q-switching dynamics of the Nd:YAG planar waveguide laser, developed by Baker [67], based on the standard model presented by Koechner [2] adapted to include the modulator transmission measured in section 2.3 and modified to incorporate the high gain possible within the planar waveguide.

The AOM transmission function can be seen in equation 2.7. This is based on a Fermi-Dirac shape with a super-imposed 27 MHz frequency introduced when the RF power is applied to the modulator. Within this function, t is time and t_0 is the time at which the RF power to the AOM is switched off, giving a ∼70 ns switching speed,

whilst f is the RF frequency of 27 MHz. This function can be seen in figure 2.14 and closely matches that observed experimentally in section 2.3.

$$M(t) = \left(0.95 - \frac{0.7}{1 + exp(\frac{t-t_0}{\Delta t})}\right) + 0.1 \cdot sin(2\pi ft) \cdot \left(\frac{1}{1 + exp(\frac{t-t_0}{\Delta t})}\right) \tag{2.7}$$

The model calculates the pulse energy at 3 points within the laser resonator for each round-trip after an initial seed of 10 photons is introduced as $\rho_{1,0}$ at time $t = 0$ as shown in figure 2.13. This pulse energy is then propagated through the gain section, with double-pass amplification factor G, where $G = \frac{\ln(g)}{2}$, with g being the small signal gain coefficient. This gives pulse energy $\rho_{3,n}$ which then has loss due to the modulator transmission $M(t)$ applied to it, starting the next round-trip with pulse energy $\rho_{1,n+1}$. The small signal gain coefficient, g, is also modified according to the incident pulse energy for each round trip. This process continues until $t = t_0$, at which point the RF to the AOM is switched off resulting in an optical pulse building within the laser, the energy of this pulse is monitored through recording the pulse energy, $\rho_{1,n}$, for each round-trip, n. Pulse energies ρ_1, ρ_2 and ρ_3 in terms of number of round trips, n, are expressed in equations 2.12,2.8 and 2.10 respectively, whilst the small signal gain coefficient, g, in terms of number of round-trips is expressed in equations 2.9 and 2.11 based on modulator transmission in terms of number of round-trips, M_n.

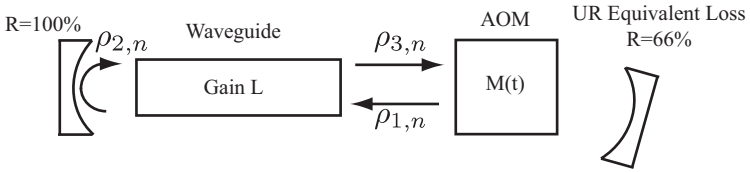

Figure 2.13 – Simplified resonator diagram detailing the pulse energies to be calculated at various positions around the resonator.

$$\rho_{2,n} = ln[1 + (exp(\rho_{1,n}) - 1) \cdot exp(g_n)] \tag{2.8}$$

$$g_{1,n} = g_n - (\rho_{2,n} - \rho_{1,n}) \tag{2.9}$$

$$\rho_{3,n} = ln(1 + (exp(\rho_{2,n}) - 1)exp(g_{1,n})) \tag{2.10}$$

$$g_{n+1} = g_n - (\rho_{3,n} - \rho_{1,n}) \tag{2.11}$$

$$\rho_{1,n+1} = \rho_{1,0} + R \cdot M_n \cdot \rho_{3,n} \tag{2.12}$$

Figure 2.14 shows a plot of pulse energy, ρ_1 against time for double-pass amplification factor $G = 3$ and $G = 6$, this shows that with a higher gain, the pulse delay (build-up time) is short enough that the pulse formation interacts with the dissipating ultrasonic wave due to the 70 ns RF switch-off time. The pulse delay is measured from $t = t_0$ to the point at which the pulse forms. By performing this calculation with varying double-pass amplification factor, the point at which ultrasound interaction occurs is with a double pass amplification factor of $G = 3.5$, representing a small-signal gain coefficient of $g = 0.27$ m^{-1}. Increasing G to more than 6.4, shows pre-lasing to take place, this can be seen in figure 2.15, this is due to the high gain allowing the laser to oscillate through the loss introduced by the AOM. The model results of pulse build-up time and pulse energy for various values of G can be seen in figure 2.16.

The results of this model show that pre-lasing should occur due to the high gain present within the resonator, assuming no additional loss is introduced within the experimental configuration. Pulse interaction with the dissipating ultrasonic wave within the AOM will also occur when pulse build-up times are less than 100 ns. These results suggest the device should be operated in the high repetition rate regime, where there is not sufficient time for the gain within the waveguide to reach these values, causing a combination of pulse-broadening and pre-lasing.

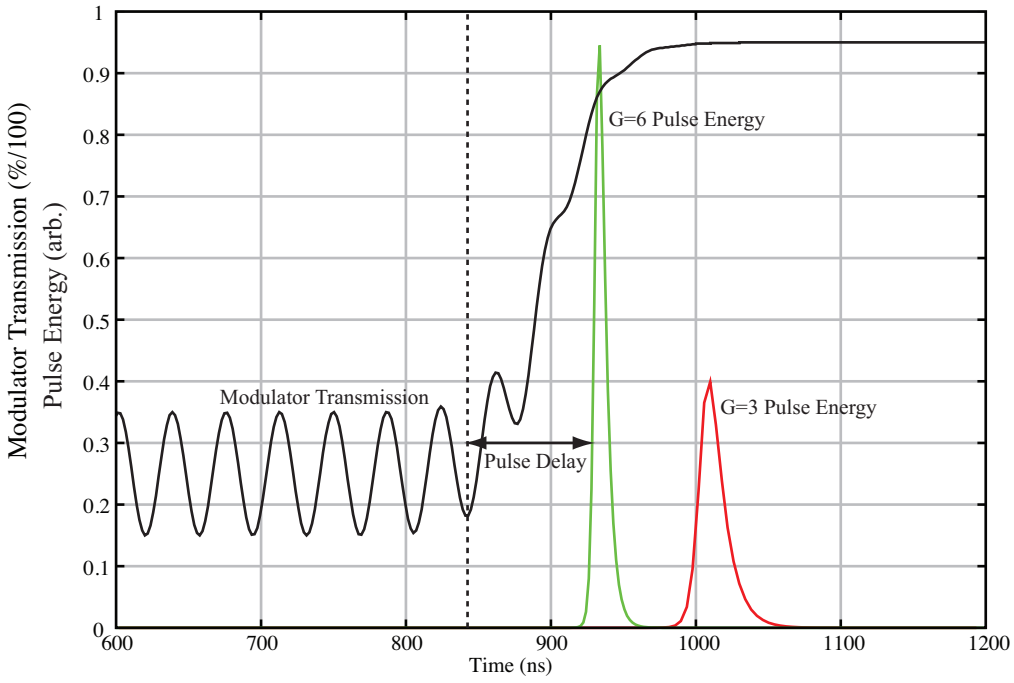

Figure 2.14 – Q-switch pulse dynamics for double pass amplification factors of $G = 6$ and $G = 3$.

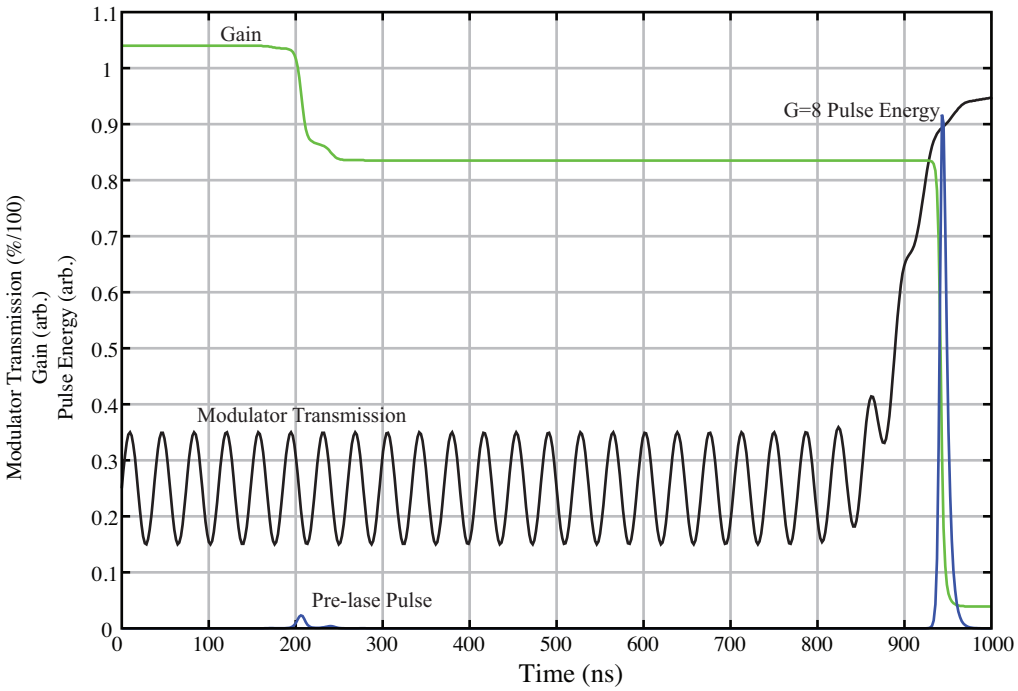

Figure 2.15 – Pre-lase pulse formation occurring when double pass amplification factor, G, is greater than 6.4.

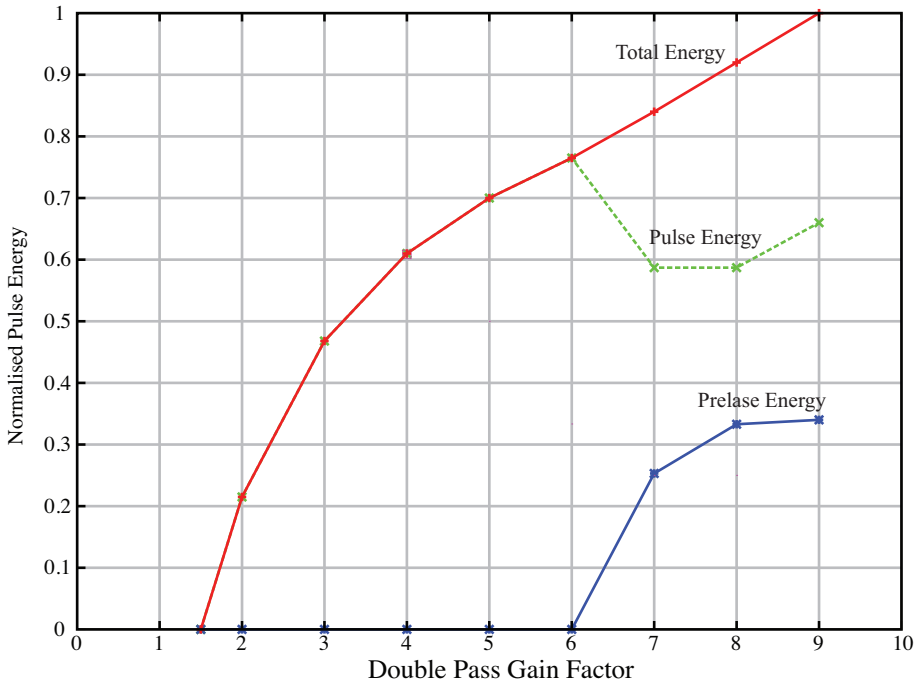

Figure 2.16 – Pulse energy from the laser with variable double-pass amplification factor, G. With a double-pass amplification factor of >6, prelasing occurs reducing the energy in the main Q-switched laser pulse.

2.5 Prelasing, Postlasing and Parasitic Oscillation

2.5.1 Prelasing and Postlasing

Prelasing occurs when the Q of the cavity is not spoiled sufficiently to hold off laser oscillation as predicted in section 2.4. To test for prelasing, the laser cavity was built as shown in figure 2.1 with the RF to the AOM off. The resonator was aligned giving a maximum CW power of 100W with an M^2 of 1.3, showing a loss of 17% due to the additional insertion loss from the polariser and AOM. The AOM was then turned on at 27MHz with varying RF power and the change in the laser output power was monitored. The results of this experiment can be seen in figure 2.17. It can be seen that with an RF power of <60W lasing continues with reduced power due to pre-lasing. With the RF power >60W lasing is stopped showing that this is the required power to introduce sufficient cavity losses to prevent prelasing. The model in section 2.4 predicted pulses being emitted with CW RF applied to the AOM, indicating prelasing should occur, however, the additional insertion loss of the AOM and polariser is sufficient to prevent prelasing from occurring.

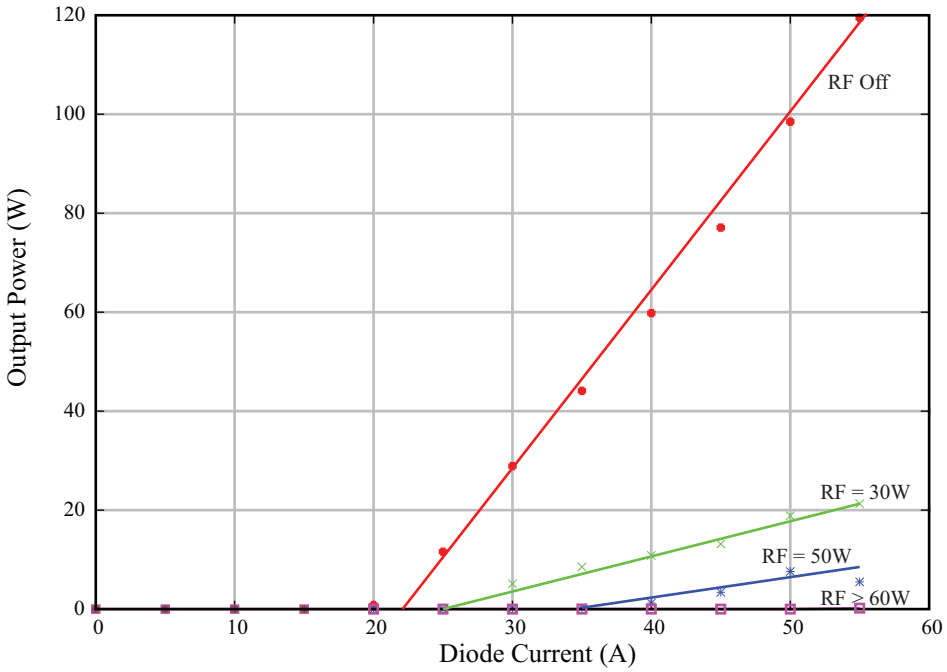

Figure 2.17 – CW output power from the laser with the RF on CW at various power levels. Values of RF above 60W show that laser oscillation is completely held off, whilst values below 60 W will cause prelasing to occur.

Postlasing is the process in which a pulse train forms due to slow closing of the modulator. After the Q-switched pulse is formed, if the RF to the AOM is not turned on quickly enough, additional pulses are formed due to the CW pumping of the gain medium. Postlasing was prevented by adjusting the duty factor of the signal generator

modulating the RF signal to the AOM. The pulses from the laser were monitored using the InGaAs photodetector on an oscilloscope with the AOM RF signal overlaid on a second channel, the pulse-width was then varied until post-lasing was prevented and the RF switching on did not interfere with the tail of the Q-switched laser pulse. The process can be seen in fig. 2.18.

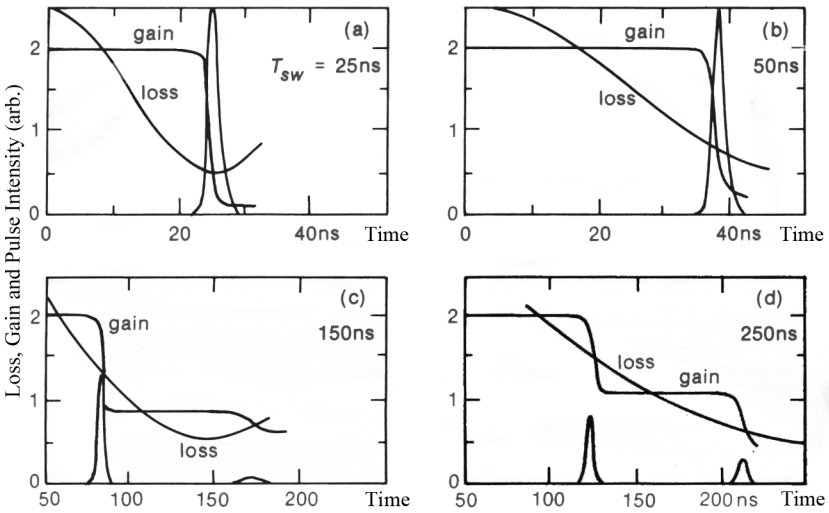

Figure 2.18 – This figure describes the post-lasing process. A) shows the case where the switching time (T_{sw}) is sufficiently short such that the output pulse occurs when the cavity loss is at a minimum. B) shows the case of a longer switching time, resulting in a pulse occurring before cavity loss reaches a minimum. C) shows the case of a significantly longer switching time, resulting in an initial pulse with half the intra-cavity gain leaving enough gain within the cavity for a second pulse to form. D) shows a similar situation to C) but for a longer switching time. Figure extracted from [31].

2.5.2 Parasitic Oscillation

Parasitic oscillation is a common problem with slab shaped solid-state lasers. Unwanted round-trips can form within the gain medium which compete for gain with the resonator mode. Due to the grazing incident angles of the parasitic rays on the waveguide side facets, simply AR coating the sides of the waveguide is not sufficient to suppress parasitic oscillation. The AR coating would have to function at all incident angles from 0° to 90°. At low repetition rates, parasitic oscillation was detected from the planar waveguide laser. With a repetition rate of <10 kHz a glow around the waveguide was observed on an IR detector card, this glow was characterised by placing a power meter and photodiode in the positions shown in figure 2.19. The results of this can be seen in figure 2.20 and 2.21, at low repetition rates a clear threshold can be seen on the power meter with a spiking behaviour observed in the time domain corresponding to the same pump threshold, this process is consistent with relaxation oscillations from a solid state laser [65]. This parasitic oscillation competes for gain

with the resonator mode and can be seen clamping the pulse energy of the Q-switched pulses in section 2.6.

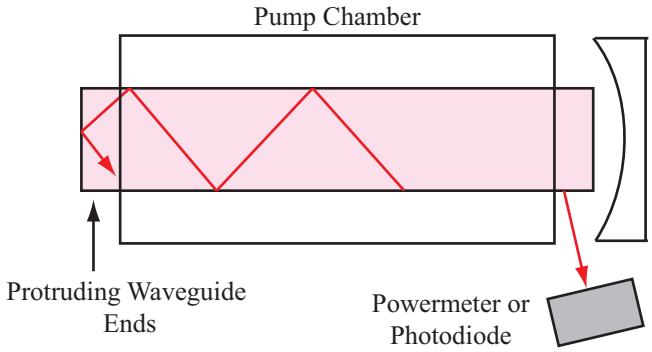

Figure 2.19 – Parasitic oscillation within the waveguide. The ends of the guide protruding from the pump chamber enable the parasitic light to escape the waveguide and allows detection using the photodetector in the position shown.

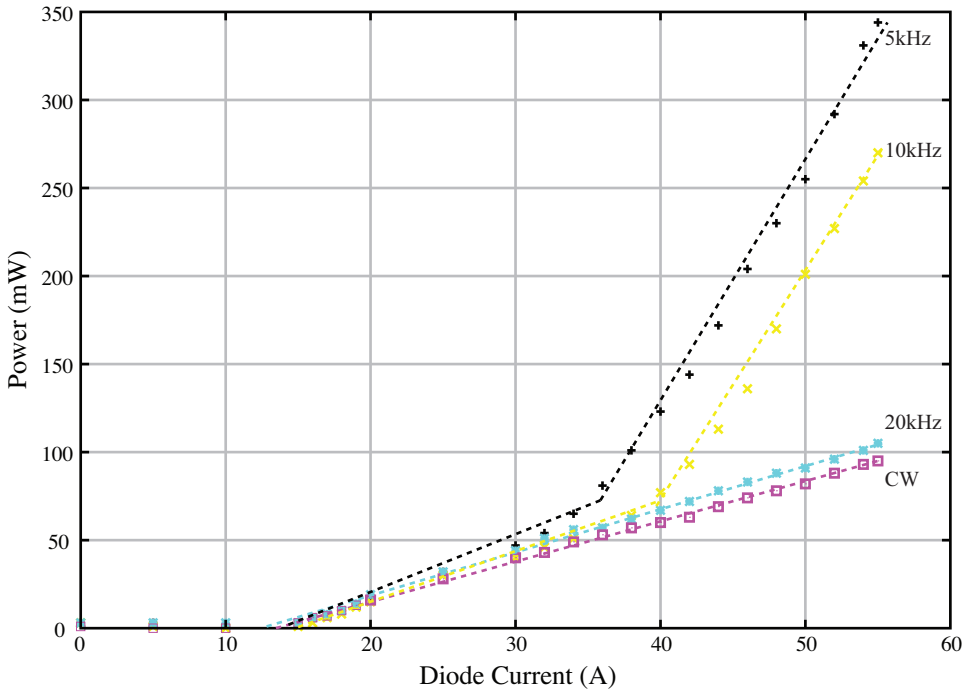

Figure 2.20 – Detected parasitic oscillation power at the position shown in figure 2.19, at repetition rates below 20 kHz, a clear threshold is observed with typical laser behaviour.

Parasitic oscillation was previously observed by Lee [28] using a Nd:YAG planar waveguide with similar dimensions lasing CW. He observed that scratching the side facets of the waveguide with abrasive paper increased the side-wall reflection loss of the parasitic oscillation sufficiently to prevent it clamping the gain. The roughening of the waveguide structure increased the small signal gain coefficient, g_0, of the laser from $10m^{-1}$ to $20m^{-1}$, however, the waveguide laser reported here has no parasitic oscillation suppression therefore is operating with a gain limited by parasitic oscillation.

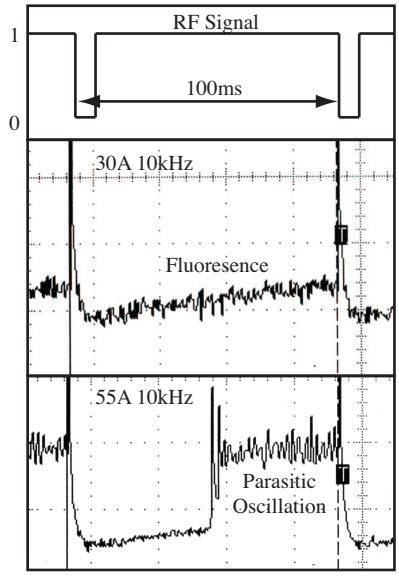

Figure 2.21 – Parasitic oscillation detection in the time domain with the photodetector positioned as shown in figure 2.19. With a diode stack pump current of <35A, no parasitic oscillation is detected, the oscilloscope picture shows a steady increase in fluorescence with time. When the diode current is >35A, a clear spiking behaviour can be seen in the time domain indicating lasing taking place.

2.6 Q-Switching Characteristics and Stability

This section discusses the characteristics of the Q-switched planar waveguide laser. Pulse energy and duration, average power and the stability of the laser have been measured. The laser resonator was set up as shown in figure 2.1, configuration A and aligned to give maximum CW output power. A mode selective slit was then placed within the cavity giving mode control in the waveguide direction giving an output beam with near diffraction limited beam quality factor, M^2, of 1.3 in the unstable resonator direction and 1.5 in the waveguide direction, matching that previously demonstrated by Lee [28] with the laser operating CW.

2.6.1 Average Power, Pulse Energy, Pulse Duration and Build-Up

The average power of the laser was measured by coupling the beam from the laser into a water cooled power meter, an additional diverging lens was placed in the beam path to increase the size of the laser mode on the power meter surface to prevent it from being damaged due to the high incident intensity and pulse energy. The results of this experiment can be seen in figure 2.22. With a repetition rate >100kHz the output power matched the power emitted with the RF off, lasing in the CW state. With lower repetition rates the average power starts to roll over at lower pump densities

due to the onset of parasitic oscillation.

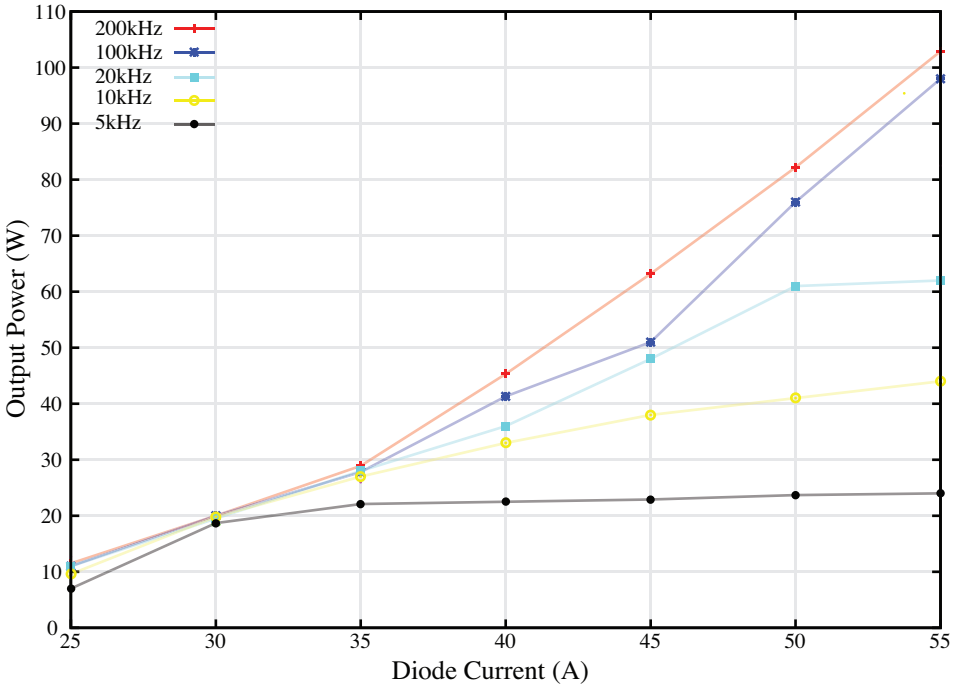

Figure 2.22 – Average power of the laser at various repetition rates. At low repetition rates the output stops increasing due to a combination of the onset of parasitic oscillation with the short build up time causing the pulse to collide with the dissipating RF introducing additional loss into the cavity.

The pulse width of the laser pulses was measured by looking at the scatter from the surface of the power meter with an InGaAs fast photodiode. The FWHM of the pulses was taken as the width and plotted in figure 2.23. These results show a minimum pulse width of around 15 ns, the pulse width is limited by the slow opening of the Q-switch causing pulse broadening and pulse width modulation due to the 27 MHz frequency in the modulator transmission function.

The pulse energy was calculated by using the equation, $E = P \cdot t$, where E is the pulse energy, P is the average power and t is taken from the corresponding pulse duration. Figure 2.24 shows a plot of these results, again, the graph shows a rolling over effect due to the onset of parasitic oscillation at low repetition rates. A maximum pulse energy of 4.5 mJ was obtained with a 5kHz repetition rate, 100kHz rep. rates showed up to a 1mJ pulse energy which could be improved through more powerful pumping diode lasers. Extrapolating the previous 3 graphs to double the pump density shows the possibility of operating at 200kHz with an average power of 200W with 1mJ, 50ns width pulses, or 40kHz operation with 4mJ <20ns pulses.

The pulse build-up time was measured using a HeNe laser as a timing beam, it was launched co-axially into the resonator so it passed through the AOM at the height of the laser mode, through the waveguide core and out through the rear mirror,

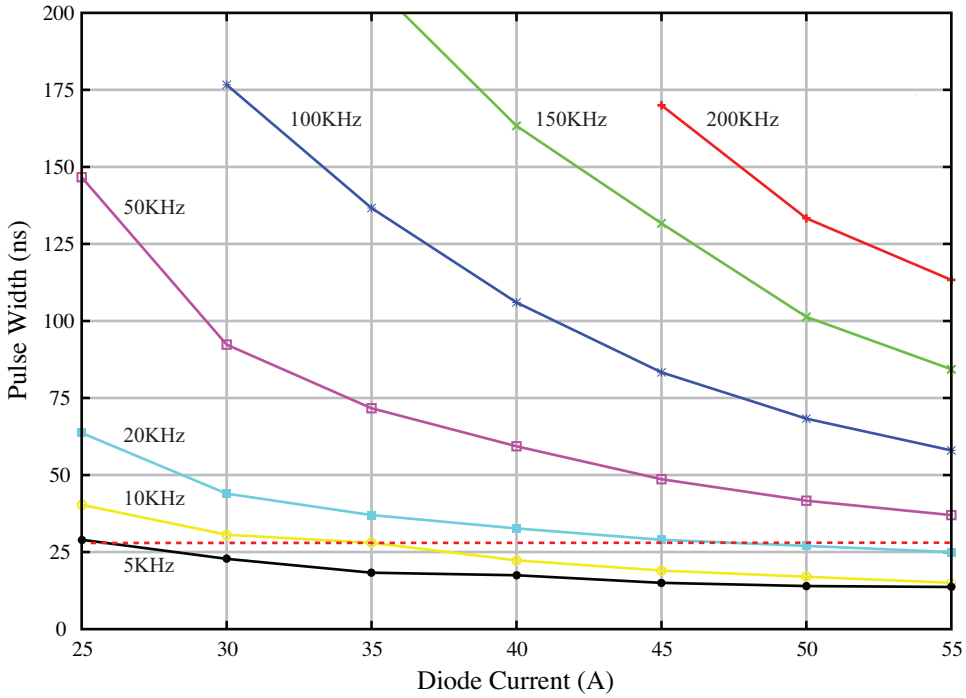

Figure 2.23 – Pulse width for various repetition rates. The dotted red line represents the point at which the build up time for each pulse is short enough that collision with the dissipating RF occurs resulting in a minimum pulse width of ∼15 ns.

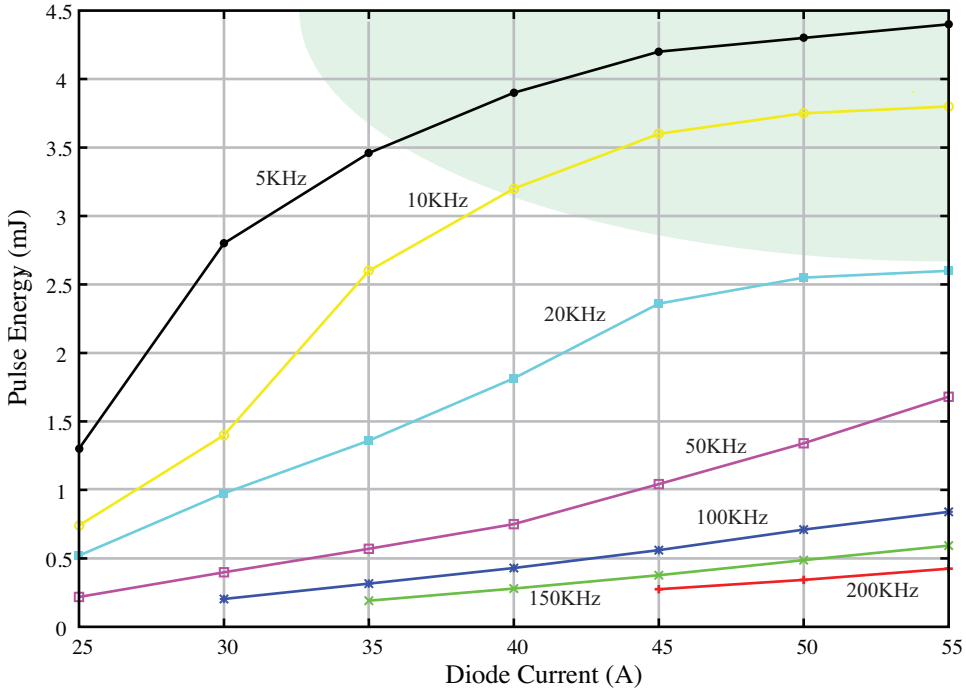

Figure 2.24 – Pulse energy for various repetition rates. The shaded region represents the area at which parasitic oscillation was detected, effectively clamping the available gain.

a beam splitter was then used to deflect the HeNe probe beam onto a fast silicon photodetector. This HeNe probe beam was used to monitor the AOM giving an optical timing reference of the RF signal being turned off and on. The scatter from

the Q-switched pulses striking a power meter was then monitored using an InGaAs photodetector and the delay between the AOM switching and the pulse striking the power meter was measured. The build-up time is shown in figure 2.25, this shows that the build-up time and subsequently the pulse-width is limited by the slowly opening AOM. Figure 2.26 shows oscilloscope traces for pulses with build-up times both above and below the AOM switching time, with a build-up time <100 ns, pulse shape starts to occur.

The pulse to pulse stability was obtained by taking a sample of 100 pulses at various repetition rates and measuring the height of each pulse. Analysing these pulse heights showed a variation in height of <5%, comparable to that of commercial 100 W class Nd:YAG Q-switched laser systems such as the GSI Group JK100P [70]. The laser presented within this chapter significantly improves on commercially available Q-switched lasers due to the excellent beam quality compared to an M^2 of ∼30 available in commercial systems.

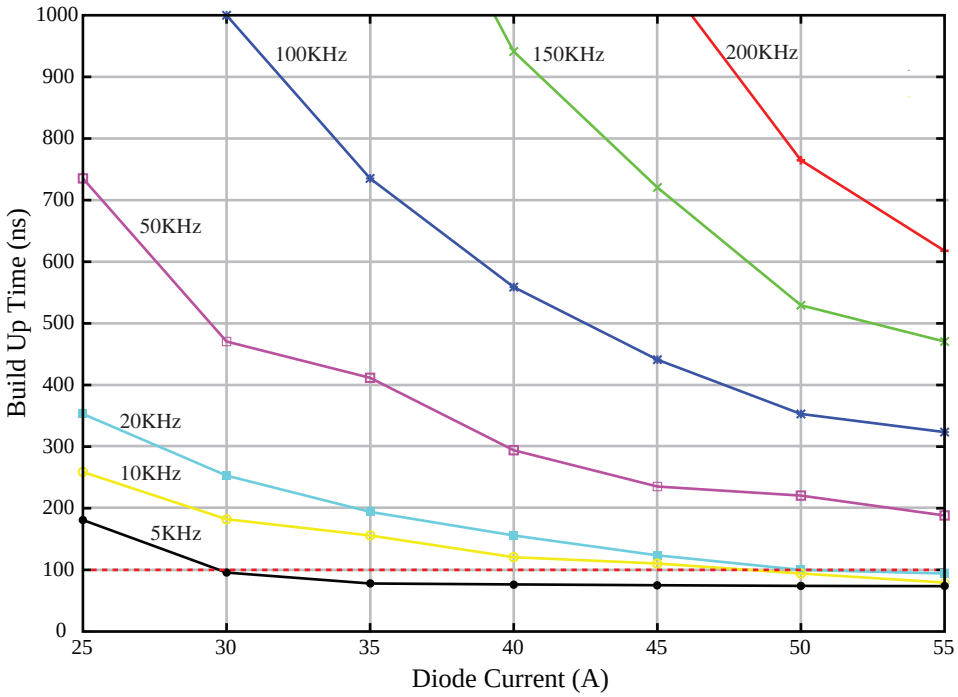

Figure 2.25 – Pulse build up time for various repetition rates. The dotted red line represents the time taken for the AOM to fully open at 100 ns, any pulses with a build up time below this will interact with the dissipating RF resulting in a broadened or double pulse.

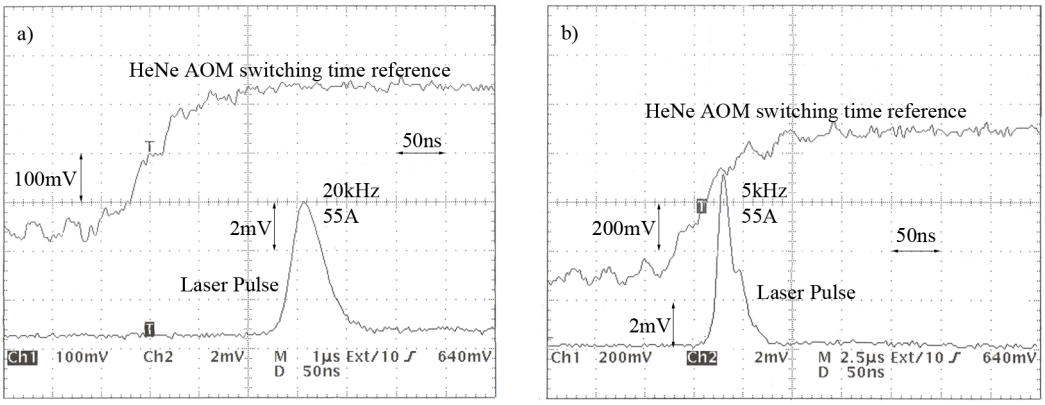

Figure 2.26 – a) Oscilloscope trace of a Q-switched pulse using 55A of diode current and a repetition rate of 20 kHz. b) Oscilloscope trace of a pulse using 55A at 5 kHz, the pulse is broadened through collision with the opening AOM.

2.6.2 Intra-Cavity Pulse Build Up

Utilising the HeNe timing reference beam that was used for measuring build up time, it was possible to monitor the intra-cavity pulse build up. The rear mirror (R>99.9%) had slight leakage of the intra-cavity radiation. By translating the InGaAs fast photodiode laterally across this leakage, it was possible to compare the pulse at the time of leakage with the HeNe timing reference. The minimum delay between AOM switching time and pulse detection corrected to a time delay of 0 ns with other delays measured from this point. The results of this are plotted in figure 2.27.

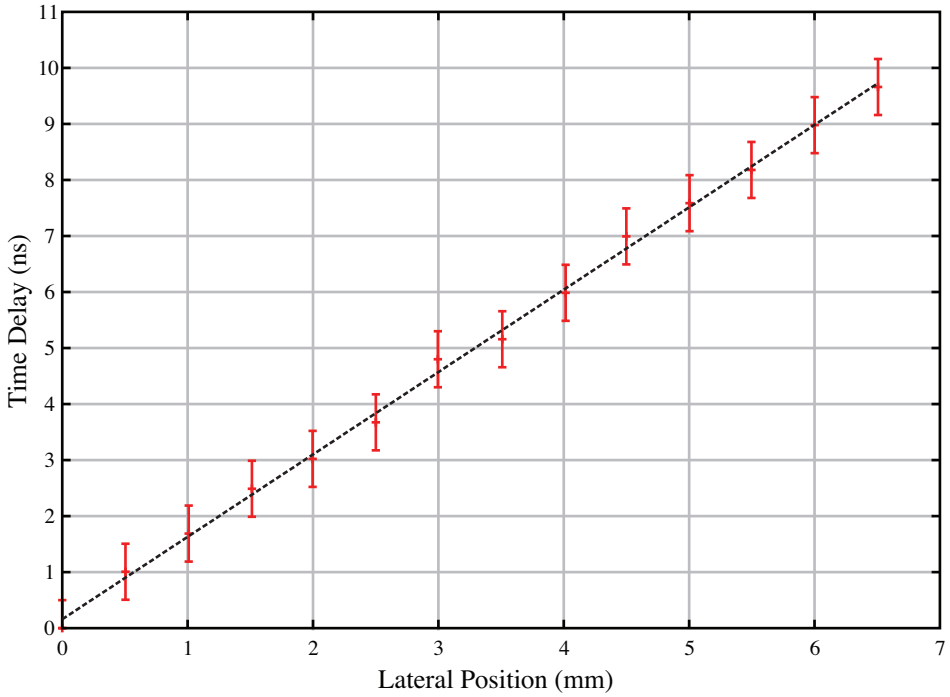

Figure 2.27 – Timing jitter associated with each repetition rate.

As can be seen in figure 2.27, a linear time delay is seen across the resonator with

a minimum delay on the optical axis at 0 mm. As the detector is moved away from the optical axis the time delay increases gradually until it reaches 10 ns at the output coupling edge of the front mirror. This delay corresponds to the time calculated for a ray to start on axis and 'walk' its way out of the resonator equivalent to 6 round trips, calculated using a method of injecting a Gaussian beam back into the unstable resonator [71]. These results confirm the idea that the Q-switched pulses form on axis within the unstable resonator and gradually 'walk' out of the cavity.

Section 2.3.2 showed the ultrasound within the AOM does not operate on a beam with the full width of the planar waveguide. These results show the pulses to form on axis and walk from the cavity, confirming that the lateral uniformity of the ultrasonic wave within the AOM is not critical to achieving good Q-switched operation of an unstable resonator.

2.7 Conclusions and Future Work

The work presented within this chapter shows the Nd:YAG planar waveguide laser to have excellent Q-switching properties when used with a hybrid unstable resonator. In the low repetition rate regime (<20 kHz), pulse energies as high as 4.5 mJ have been achieved, limited by parasitic oscillation within the planar waveguide. Pulse durations as short as 15 ns have been recorded, limited by the RF switch off time of the AOM. In the future, with improved modulators and electronics this time can be reduced by a factor of 2, synchronising the modulator switch off to the 27 MHz modulation will also improve the timing jitter of the output pulses. It is also possible to use an AOM which operates on an RF of 47 MHz giving improved switching time, however, the change in the scattering properties and diffraction efficiency would need to be determined. Improvements to the design of the planar waveguide itself can suppress parasitic oscillation, allowing for higher gain, giving higher pulse energy and shorter pulses, however, even with improved AOM drive electronics, this will cause the pulse-build-up time to reduce causing issues with the RF switch-off time. A longer resonator could be utilised to increase the build-up time, however, this in turn will increase the pulse duration. Currently, the only limitation when operating in the high repetition rate regime is the available pump power. In the future it will be possible to replace the pump diode bars with 100 W output per bar, increasing the available pump power to 1 kW, extrapolating the results obtained within this chapter increase the average power output to >200 W, maintaining the near diffraction limited beam quality and allowing 1 mJ pulse operation at 200 kHz with a pulse duration of ∼50 ns.

To improve the laser efficiency, Yb:YAG can be used as the active medium. This has the advantage of a better quantum efficiency and longer upper-state lifetime,

allowing for increased energy storage and higher gain. However, the issues with the AOM remain, meaning the laser can only be operated in the high repetition rate regime.

Chapter 3

Diode Side Pumping of an Yb:YAG Planar Waveguide Laser

3.1 Introduction

Within this chapter, solid-state planar waveguide laser development is continued using an Yb:YAG gain medium. Yb:YAG is desirable to use as a replacement for the Nd:YAG laser due to its improved quantum efficiency giving better laser efficiency. Yb:YAG also has a significantly longer upper-state allowing greater energy storage for efficient, high-power, high-energy Q-switching.

Yb:YAG has only become commonly used as a laser crystal since the early 1990's [41] due to the common availability of low cost, high average power diode lasers. Unlike Nd:YAG, Yb:YAG operates as a quasi-3 level laser meaning it has a minimum pump intensity required before it becomes transparent at the laser wavelength of 1030 nm. Due to this, diode side pumping at 940 nm is utilised instead of the face pumping technique previously utilised for Nd:YAG planar waveguides. Novel diode laser pump sources with custom beam corrective phase plates have been used enabling the coupling of up to 450W into each waveguide side facet, giving sufficient incident intensity to surpass the transparency threshold.

This chapter discusses laser operation of two Yb:YAG planar waveguides with both stable and unstable resonators. A study of parasitic oscillation is carried out resulting in the waveguide structure being re-polished to suppress this oscillation resulting in the laser efficiency being limited by resonator constraints.

The project presented within this chapter was worked on by several members of the LPA group. The initial design of the laser presented within this chapter was carried out by Prof. Howard Baker, Dr. Fernando Monjardin and Dr. Jesus Valera before the author began working within the group. Once the work presented within chapter 2 was complete, both Dr. Monjardin and Dr. Valera left the LPA group and the author took over the project, from section 3.3 onwards. The work on parasitic

oscillation presented in section 3.4 was performed in collaboration with Natalia Trela, a three month summer project student who is now a fellow PhD student within the LPA group.

3.2 Laser Design

This section discusses the planar waveguide used for the work presented within this chapter, the micro-channel water cooled heatsinks used for cooling and the novel diode pump units. The pump units were developed by Dr. Fernando Monjardin and Dr. Jesus Valera, former research associates within the LPA group, the heatsinks were designed by Dr. Monjardin and the planar waveguide geometry designed by Prof. Howard Baker.

3.2.1 Waveguide Characteristics

This work uses two planar waveguides, both comprising of 2% doped Yb:YAG core ($n = 1.82$) with a sapphire cladding ($n = 1.77$) giving much stronger waveguiding and a higher numerical aperture (NA) than the Nd:YAG - YAG waveguide used in the previous chapter. One waveguide has dimensions 6 mm wide, 13 mm long and 2.15 mm thick consisting of two 1 mm thick sapphire claddings with a 150 μm high core region. The second waveguide has a width of 12 mm with all other dimensions remaining the same. The width scaled waveguide was manufactured by joining two 6 mm width waveguide together using the same Onyx Optics bonding technique used to make the waveguide structure itself, this produced a 12 mm width with no detectable boundary, however, there is a possibility of a doping gradient being present across the interface.

Two plane-parallel ends of the waveguide are AR coated at 1030 nm for resonator coupling, whilst the opposite two edges are AR coated at 940 nm for diode pump light coupling. One side facet (940 nm) coated edge is angled at 7° from the vertical to aid in the suppression of parasitic oscillation by coupling light from the waveguide core into the claddings. The non-optical surfaces of the waveguide have no precision polishing, remaining as ground for contact with the heatsinks. Figure 3.1 shows the complete waveguide structure.

3.2.2 Heat-sink Structure

Yb:YAG requires a high incident pump intensity to reach transparency, requiring an edge pumping technique rather than the face pumping used for Nd:YAG. This results in the only surfaces available for heat removal being the top and bottom (largest)

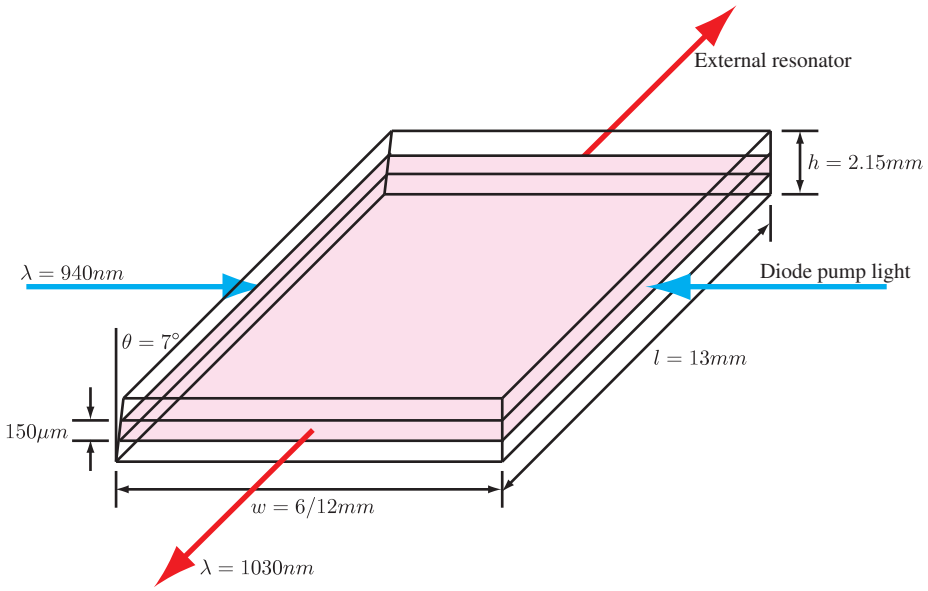

Figure 3.1 – Yb:YAG planar waveguide structure. Two waveguides have been produced, one with 6 mm width, the second with 12 mm width.

surfaces, this allows direct contact cooling with a copper water cooled heatsink and 1-dimensional heat flow from the waveguide core. These heatsinks were designed by Dr. Fernando Monjardin, a former research associate within the LPA group. The heatsink was designed so that the water is forced through micro-channels near to the surface of the heatsink giving a greater internal surface area for the water to remove the excess heat. The water flow through the heatsink is in the same direction as the laser mode giving a thermal gradient in the longitudinal direction. A diagram of one of the two identical heatsinks can be seen in figure 3.2. These are then used to house the waveguide connected with rigid stainless steel rods. The two heatsink halves are held together utilising a nut with two spring washers tightened onto a thread on each of the four stainless steel rods allowing the heatsink to self-align to the plane of the waveguide with a compressive force of 340 N. The contact area between the copper heatsink and the sapphire surface of the waveguide has a 50 μm thick layer of Indium foil placed in between. When the heatsink is pressed into the waveguide, the Indium is compressed with sufficient force for it to flow into any gaps or scratches in the interface between the highly polished copper heatsink and the frosted sapphire surface. This process gives an improved thermal interface between the heatsink and the waveguide removing the possibility of hot spots being created in areas where trapped air could act as an insulator. A photograph of the completed heatsink structure is shown later within this chapter in figure 3.9.

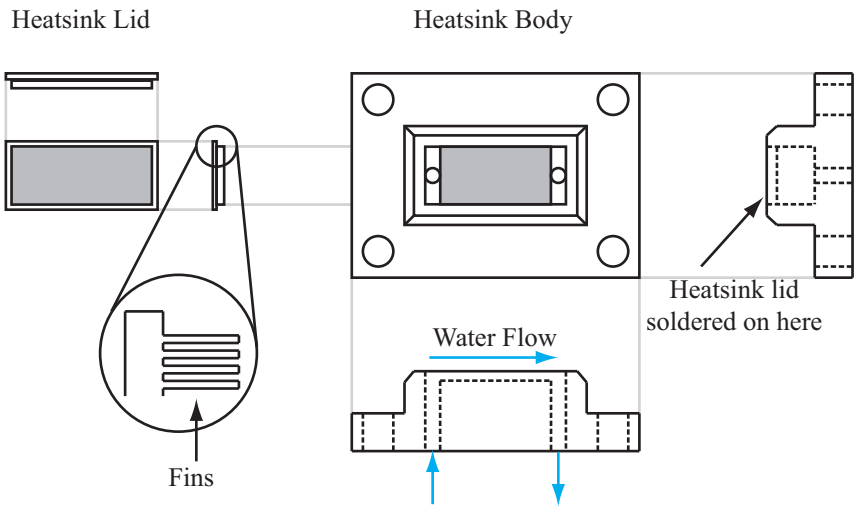

Figure 3.2 – Heatsink structure, two of these are used to cool the waveguide, one in contact with the top surface, the second in contact with the bottom surface. Indium foil is used at the sapphire - copper interface, giving improved thermal transfer.

3.2.3 Pump Unit Design

Edge pumping enables a higher pump intensity to be achieved within the waveguide than face pumping techniques along with the ability to angularly multiplex diode bars enabling pump scaling. The edge pumping arrangement also allows pumping from both sides of the waveguide. The main disadvantage of this method is the non-uniform pump profile in the lateral direction across the waveguide due to Beer's law absorption, and the difficulty in achieving multi-pass pumping when pumping from more than one side, without the use of complex polarising optics.

Two pump units were designed and built by Dr. Fernando Monjardin and Dr. Jesus Valera, previous research associates within the LPA group. Each unit consists of 6 diode bars of 80 W per bar with 49 emitters per bar giving a total of 480 W per stack with a width of ∼13 mm, matching the length of the waveguide. Each stack is then focussed using a cylindrical lens with an EFL of 38 mm, the aberrations from the cylindrical lens and the diode stack such as smile and collimation errors were corrected by creating a custom aberration correcting phase plate for each stack [72]. To control the divergence of the slow axis, a pair of gold reflectors are used to overlap the edge beams back into the waveguide creating a more uniform profile in the longitudinal direction of the waveguide. This configuration gives a line focus of <150 μm in height by 13 mm long, efficiently coupling more than 90% of the available pump light from each stack into the waveguide core. Each stack is capable of producing an incident intensity of 22.2 kWcm^{-2} on the side facet of the Yb:YAG waveguide at a diode pump current of 90 A. Each stack can operate at up to 105A of pump current to give a maximum output power of 480 W but were rarely operated

above 90 A to minimise the risk of accidental damage to each diode stack and to extend the operational lifetime. A photograph of a complete pump unit can be seen in figure 3.3.

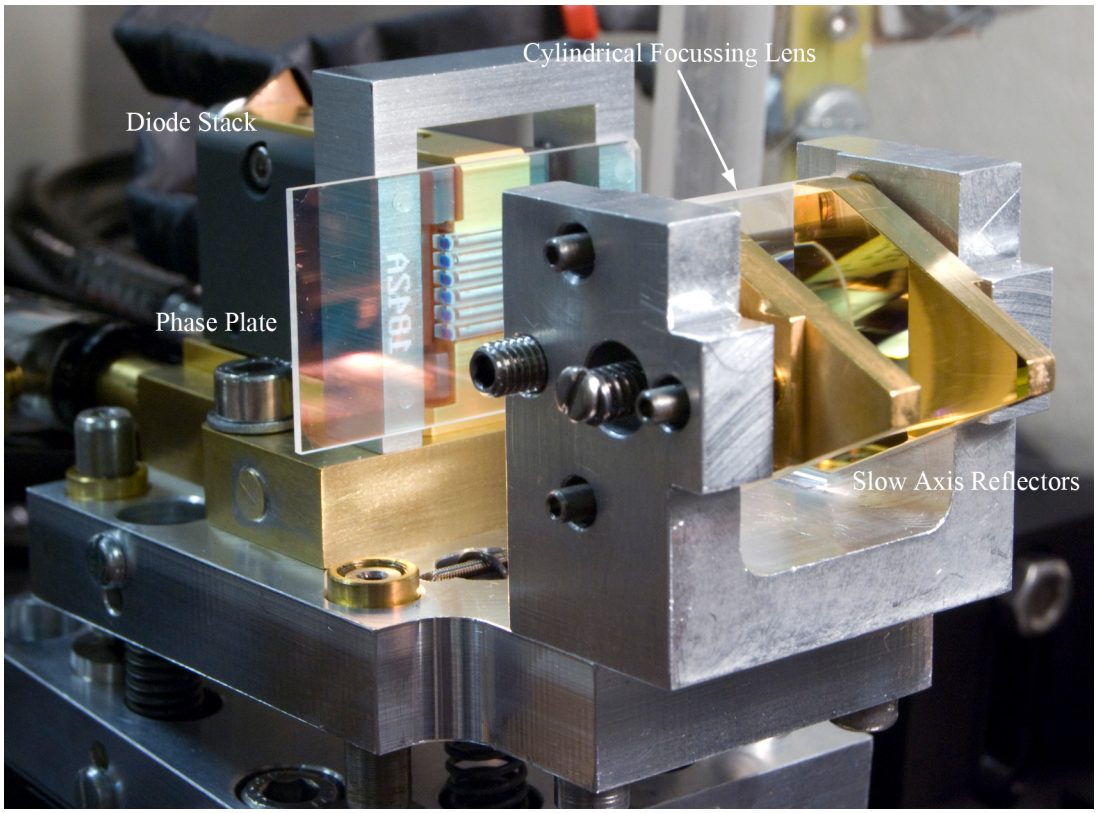

Figure 3.3 – Complete diode pump unit, designed and built by Dr. Fernando Monjardin.

The output power and corresponding emission spectra of each diode stack with respect to diode current was measured through direct coupling of each of the two pump unit's emission into a power meter and monitoring the centroid of the output spectrum with an Ocean Optics HR4000 spectrometer. The results of this experiment can be seen in figures 3.5 and 3.6. Both stacks were operated at the maximum temperature the diode chiller would allow ($27 \pm 0.3°C$) to tune the diode emission as close to the peak absorption of Yb:YAG centred at 941 nm as shown in the Yb:YAG absorption and emission spectra shown in figure 3.4 [41]. Both stacks only tune to this wavelength at full power, meaning they pump the weaker absorption band running from ~930 nm to ~940 nm. The wavelength variation shown in figure 3.6 'steps' upwards with increasing current. This effect occurs in a single diode emitter and is due to longitudinal mode hopping, however, it should not occur with a diode stack made up of 294 individual diode lasers. A possible explanation for this occurrence is injection locking due to small back-reflections from the phase-plate. This effect will lock the various emitters onto the same wavelength.

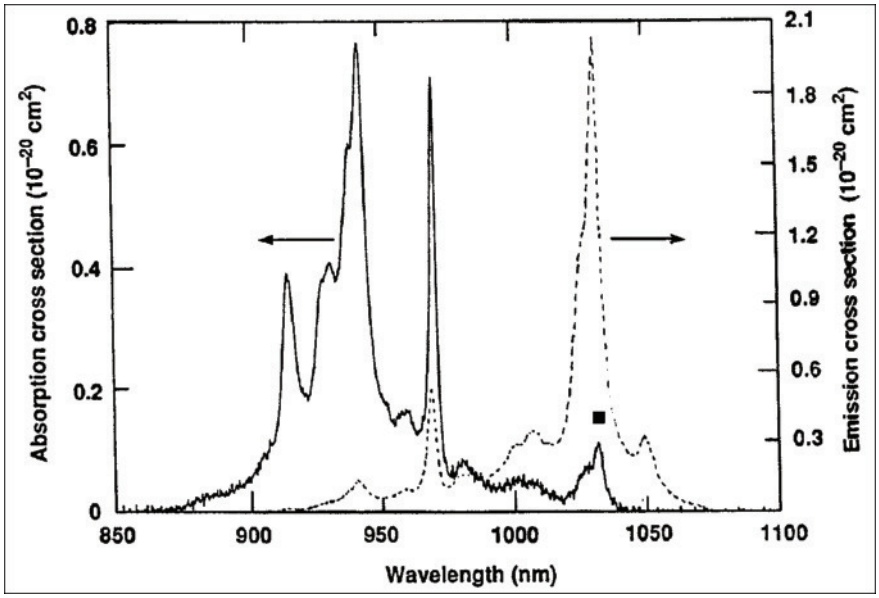

Figure 3.4 – Emission and absorption spectra for Yb:YAG at room temperature. Figure extracted from [41].

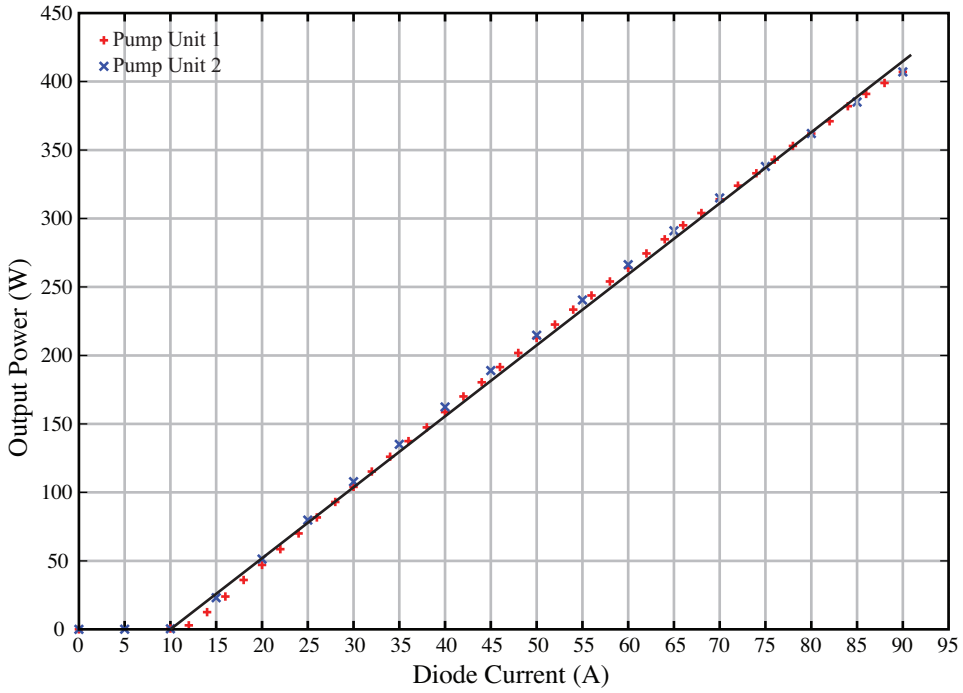

Figure 3.5 – Diode stack output power with varying diode pump current for both pump units.

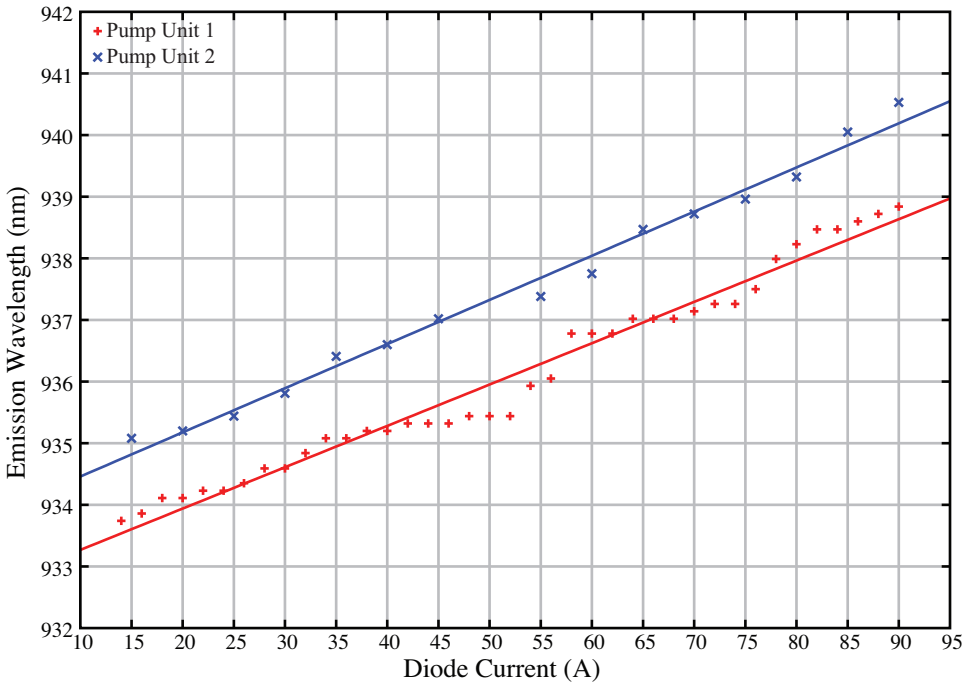

Figure 3.6 – Centroid wavelength for each diode stack with varying diode pump current.

3.3 Initial Laser Configuration

This section discusses early trials of the laser, utilising the 6 mm wide waveguide with single sided pumping. The pump absorption from a single pass through the waveguide is measured along with two resonators being tested giving laser operation. Initial experimental work within this section was performed by Dr. Fernando Monjardin with assistance from the author, at this point, the author began working on the project, aligning and obtaining results from the hybrid unstable resonator, designed by Prof. Baker discussed in section 3.3.2. After this, the work presented within this chapter was entirely performed by the author unless otherwise stated.

3.3.1 Pump Absorption

The pump unit labelled stack 1 in section 3.2.3 was aligned to the 7° facet of the waveguide. The pump unit was angled in the vertical direction so that the light within the waveguide is guided as shown in figure 3.7. Using Snell's law, the angle of the diode stack relative to the horizontal is $\theta_{air} - 7° = 5.85°$. The angle of the pump unit was set by measuring the height difference between the front and back of the diodes kinematic mount and adjusting until the angle is correct. The lateral alignment of the stack was performed using a CCD camera focussed on the waveguide facet and adjusting the stack laterally until both gold side reflectors were in-line with the waveguide edges, to ensure the stack is parallel to the waveguide a pair of vernier

callipers was used to measure the distance from the waveguide to the diode stack at each side and adjusted until both distances were equal.

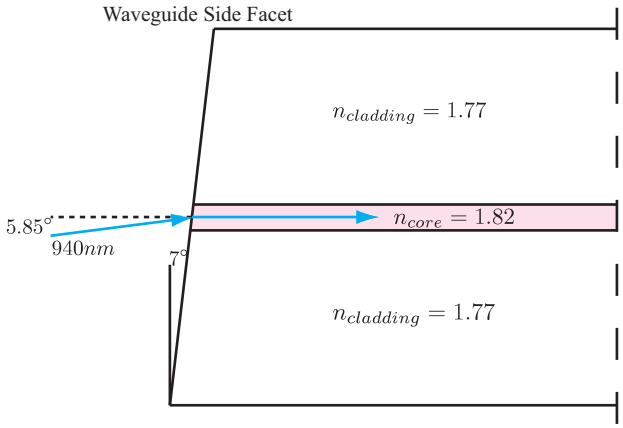

Figure 3.7 – Optimal launch angle of the pump light, giving parallel propagation through the waveguide core.

The diode stack was then pumped at low current (20A) to optimise the alignment without risk of damaging any equipment. A power meter was placed at the opposite facet to monitor the transmitted (unabsorbed) diode light. The focus, rotation and angle of the stack was then tweaked to give minimum power transmitted through the waveguide representing the maximum absorption. The diode current was then varied and plotted against transmitted power, giving 50% absorption in a single pass through the waveguide as shown in figure 3.8. Increasing the doping concentration of the Yb:YAG would improve this absorption, however, at the time of purchasing the waveguide only 2%at. doped Yb:YAG was available. A photograph of the complete pump and waveguide set up can be seen in figure 3.9.

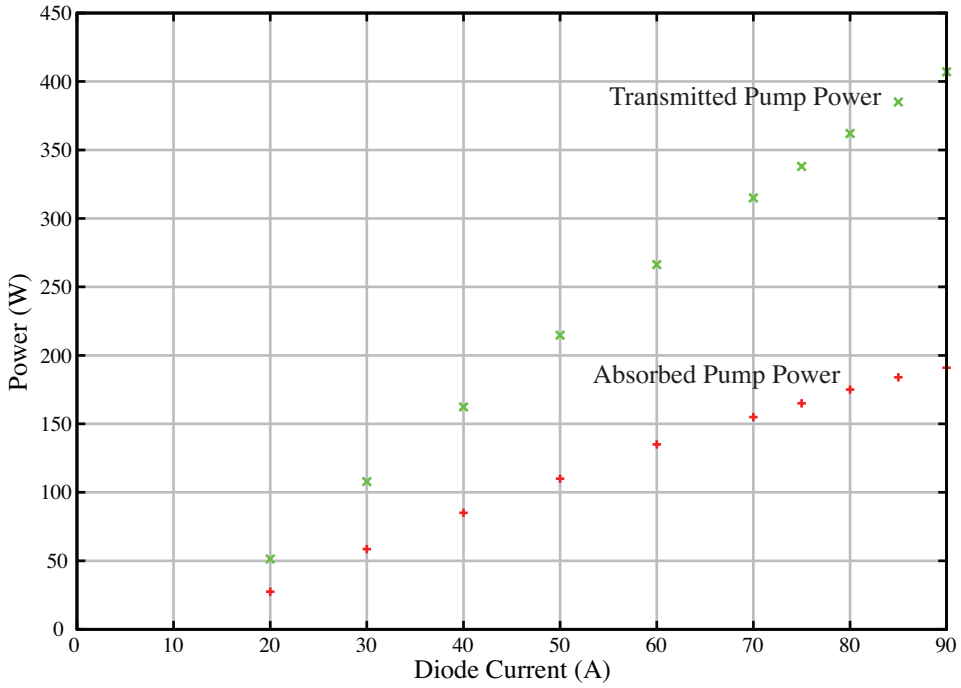

Figure 3.8 – Diode pump absorption in a single pass through the 6 mm wide Yb:YAG planar waveguide [30].

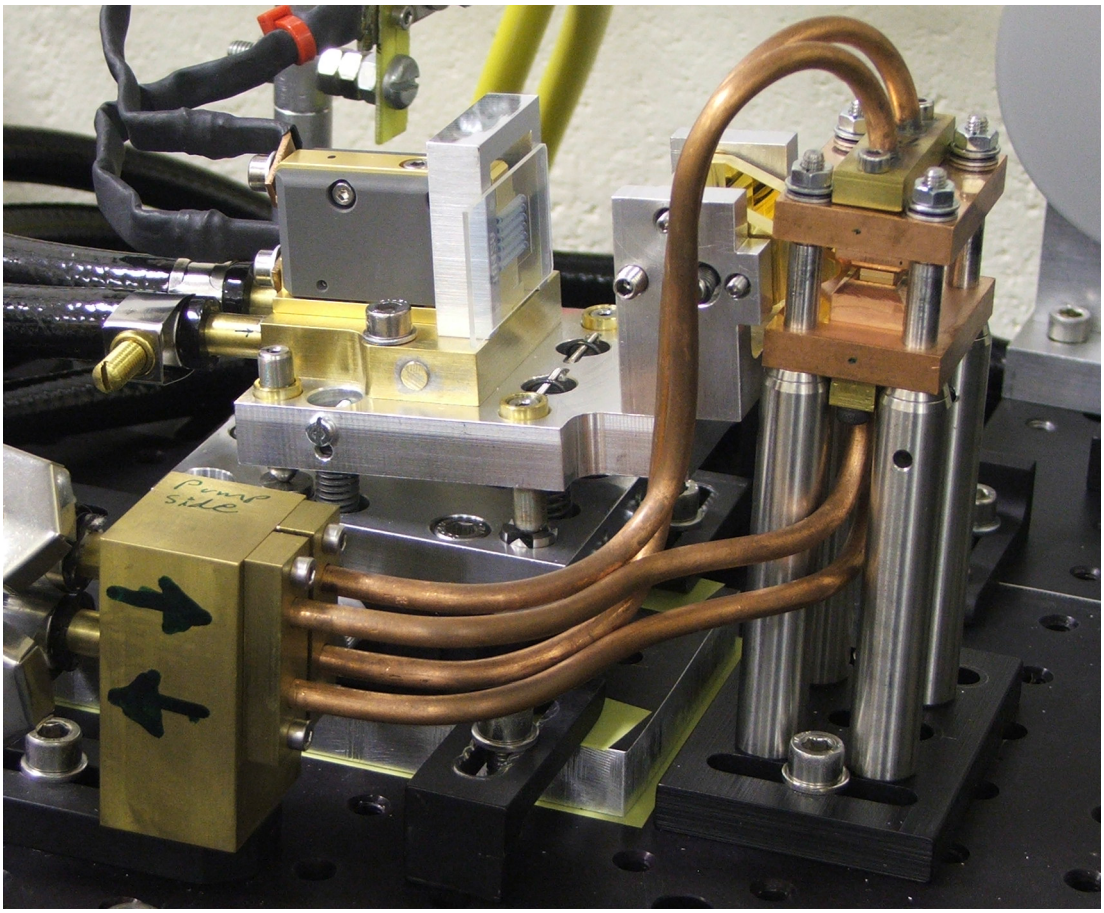

Figure 3.9 – Complete waveguide housed in heatsink structure with a pump unit aligned for single sided pumping.

3.3.2 Lensed Hybrid Negative Branch Unstable Resonator

Initial work on the Yb:YAG planar waveguides utilised a hybrid negative branch unstable resonator, similar to that used for the Nd:YAG planar waveguide discussed in chapter 2. The resonator is adapted for use with the Yb:YAG waveguide through the use of a cylindrial lens as shown in figure 3.10, this lens is required to lengthen the rear section of the resonator as the heatsinks prevent close-coupled optics. Improved heatsinks are designed in chapter 4 of this thesis which eliminate the need for this lens, allowing close-coupled optics. The lens gives case II coupling from the rear mirror and compensates for the shorter waveguide length of 13 mm compared to the 63 mm of the Nd:YAG planar waveguide reported in chapter 2.

The resonator utilises the same R_1 =207 mm and R_2 =138 mm curvature spherical mirrors as used in the Nd:YAG laser reported in chapter 2. The intra-cavity cylindrical lens has EFL=15.38 mm, it was purchased from Thorlabs with an AR coating on both faces giving $\sim 1\%$ loss per pass through the coating, this loss could be decreased at additional cost by getting a custom AR coating applied to the lens.

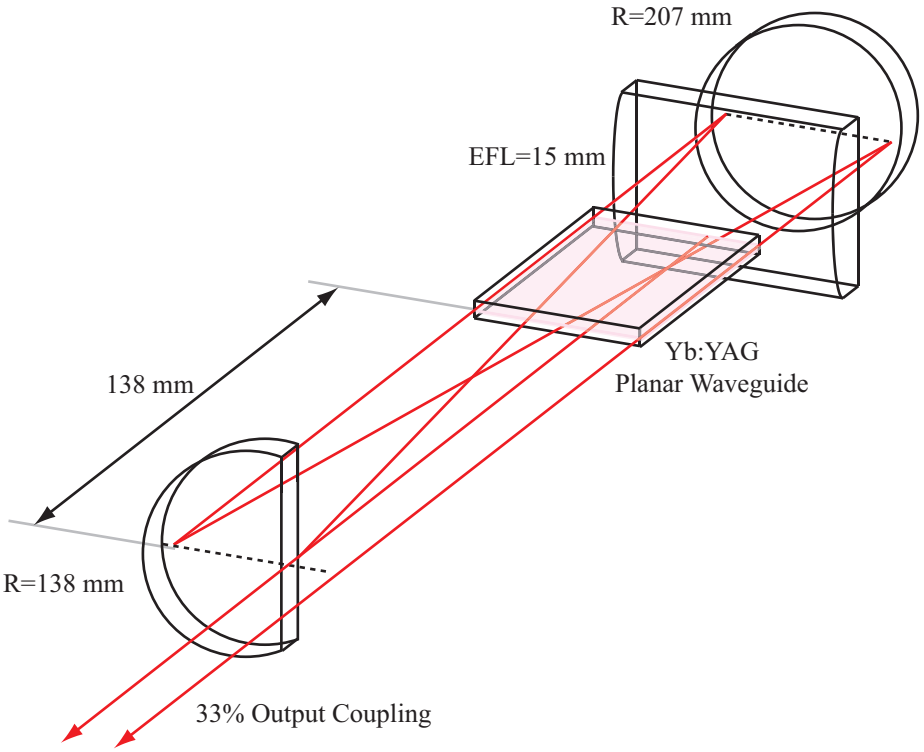

Figure 3.10 – Hybrid unstable resonator configuration for the Yb:YAG planar waveguide laser.

The lensed hybrid unstable resonator shown in figure 3.10 was aligned to the waveguide with the cylindrical lens fixed in place and aligned so it is rotated about the optical axis parallel to the waveguide. The pump diode was then set to give an absorbed power of 50 W, giving an incident intensity of 5.6 kWcm^{-2}, well above the

transparency threshold of Yb:YAG at 2.8 $kWcm^{-2}$. The resonator was then adjusted to give maximum output power. The threshold for laser oscillation was found to be 25 W absorbed corresponding to 2.8 $kWcm^{-2}$ incident intensity with only 20 W of useful laser output achieved from 240 W of absorbed pump representing less than 10% efficiency.

Monitoring the fluorescence spectra from the waveguide using a fibre coupled high resolution spectrometer showed the presence of parasitic oscillation, which has been shown to occur in the Nd:YAG planar waveguide discussed in chapter 2. This competes with the laser mode, depleting gain within the waveguide and thus introducing significant loss to the laser causing poor efficiency. This oscillation was detected as a tall, narrow peak in the fluorescence spectrum centred at 1030 nm, the peak wavelength in the gain bandwidth of Yb:YAG as shown in figure 3.11. This oscillation was seen to occur with both the resonator aligned and no resonator aligned with a threshold of 50 W absorbed pump light. This parasitic peak increased linearly with incident pump power as expected for laser oscillation. The power in the parasitic oscillation was also sampled through the use of a small thermal power meter with a detection diameter of 19 mm, placed 300 mm from the laser facet of the waveguide. The output power of the parasitic oscillation as a function of absorbed power can be seen in figure 3.12 with up to 0.25 W detected in just a small portion of the light field that surrounds the planar waveguide. This shows that a single side facet with an angle of 7° is not sufficient to suppress parasitic oscillation within the waveguide core due to the large difference in refractive index between the core and cladding, and hence high critical angle for total internal reflection.

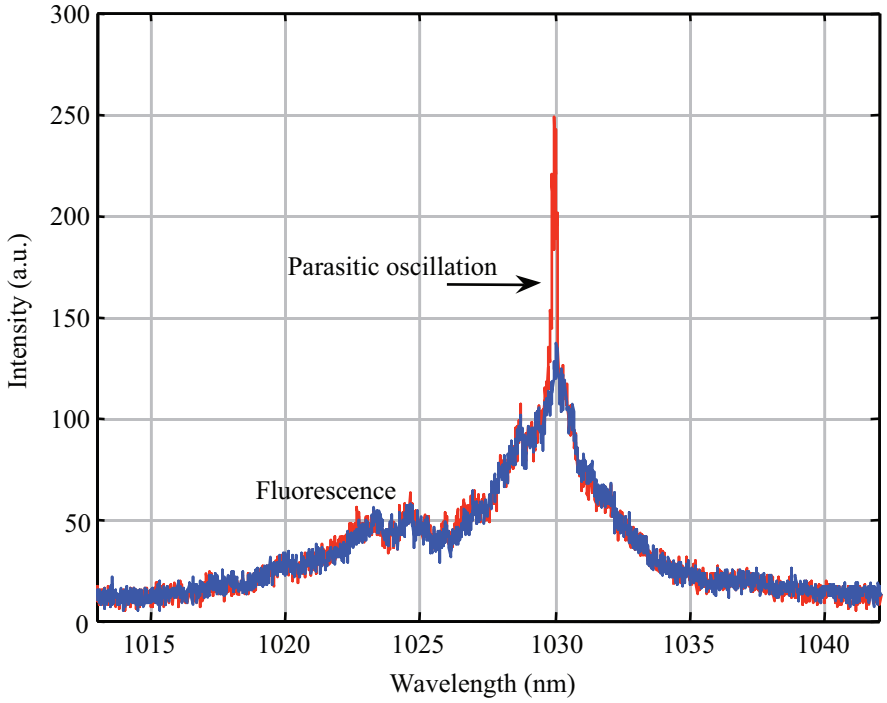

Figure 3.11 – Fluorescence spectra with no resonator aligned, above and below the parasitic oscillation threshold. The red spectra represents the fluorescence spectra with more than 50 W absorbed pump power, whereas the blue spectra represents the fluorescence spectra below the 50 W absorbed pump power parasitic threshold.

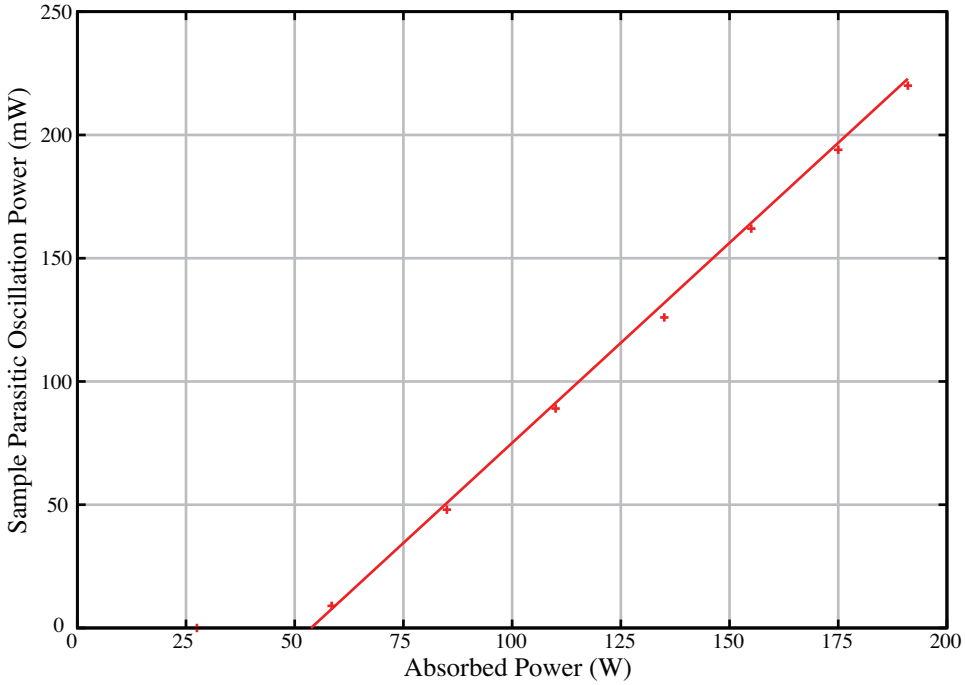

Figure 3.12 – Output power measured of a small sample of the parasitic oscillation with varying absorbed pump power.

3.3.3 Hybrid Stable Waveguide Resonator

To reduce losses within the laser resonator so the laser mode can compete more strongly with the parasitic oscillation, ideally suppressing it, a new resonator was designed. Two cylindrical lenses of curvature R=36.2 mm were coated with a dielectric coating of 95% reflectivity at 1030 nm. Using a pair of matched cylindrical mirrors a plane-plane resonator is formed in the lateral direction to give a large fill factor within the waveguide, in the transverse direction, the two cylindrical lenses are placed 36.2 mm from each laser facet giving case II waveguide coupling. This configuration gives 5% output coupling from each mirror and reduces the number of intra-cavity components to a minimum, reducing losses due to surface scatter and minimising the number of components which can cause alignment losses. The resonator configuration can be seen in figure 3.13.

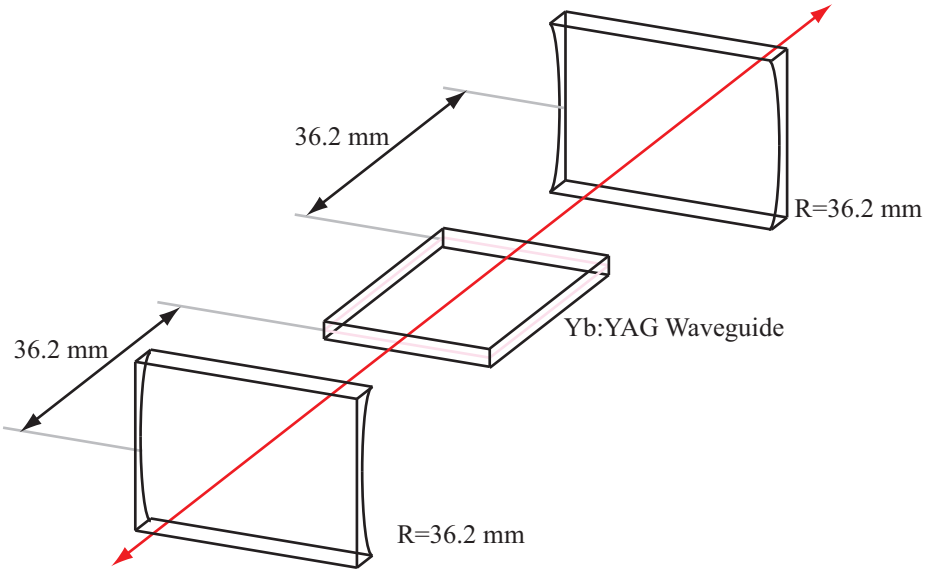

Figure 3.13 – Waveguide resonator configuration, in the lateral direction a plane-plane resonator is formed, whilst in the transverse direction, a case II waveguide resonator is formed.

The resonator was aligned to the planar waveguide with a photograph of the complete laser shown in figure 3.14. The output power as a function of absorbed power was measured and is shown in figure 3.15, giving a threshold of 20 W and an output power of 40 W, more efficient than the hybrid unstable resonator. The output beam from this resonator was very multimode in both lateral and transverse directions due to the lack of mode selection within the resonator. The power output from the laser is not directly proportional to the input power, this is due to competition with the parasitic mode within the waveguide. The spectra of the output beam was measured and found to have multiple emission peaks at 1030 nm and 1032 nm, this is due to the competition for gain between the laser mode and the parasitic oscillation, the gain of

Yb:YAG at 1030nm is quite broadband so the laser mode 'hops' from one wavelength to the next in an effort to extract the maximum gain. The emission wavelength with varying pump power is marked on figure 3.15. Using this resonator, better output power was achieved than that obtained using the lensed unstable resonator, however, the efficiency is still poor, limited by both parasitic oscillation and difficulty in aligning the rotation of the cylindrical output coupling mirrors.

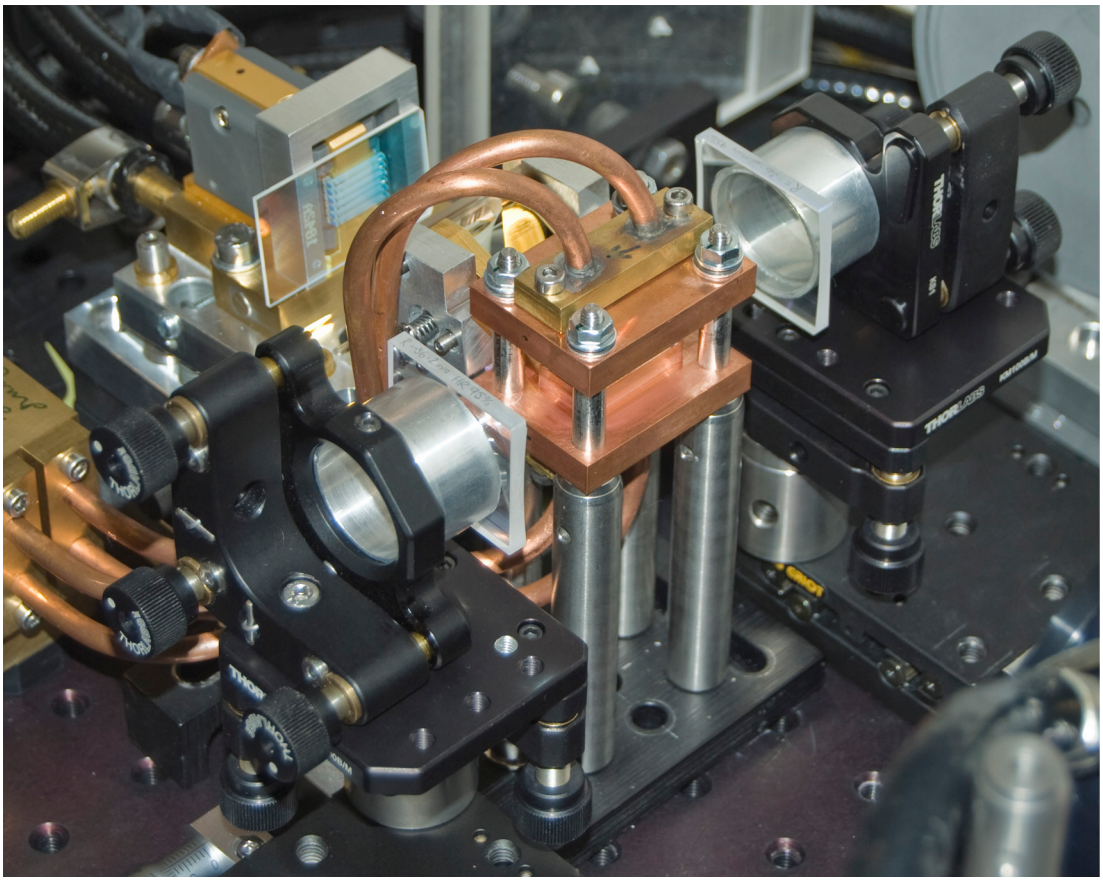

Figure 3.14 – Complete Yb:YAG planar waveguide laser, with single sided pumping using a case II/stable resonator.

3.4 Parasitic Oscillation

Parasitic oscillation has been shown to have an adverse effect on the Yb:YAG planar waveguide laser. This oscillation has previously been detected operating within the Nd:YAG planar waveguide as discussed in chapter 2 where light trapping occurs from reflection with the 'dirty' YAG surfaces in contact with the cooling water. The parasitic oscillation has a much greater effect on the Yb:YAG waveguide structure due to the higher confinement obtained from having a sapphire cladding (n=1.77). In this section, a model is developed to determine the path length of trapped rays within the Yb:YAG core, and hence their affect on competing for gain with the external cavity mode. The model also determines the effect of varying the side facet angles in an

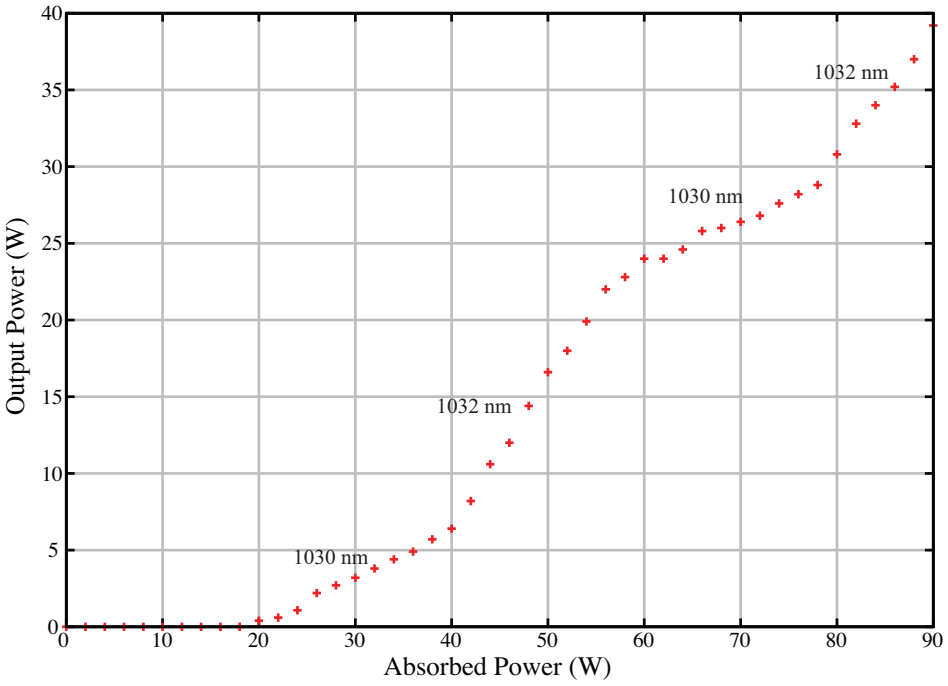

Figure 3.15 – Output power from the Yb:YAG planar waveguide laser utilising a case II/stable resonator. The central emission wavelength from the laser is denoted for each section of the power transfer curve, with 1030 nm emission having a lower slope efficiency than 1032 nm emission.

attempt to minimise the path length of the parasitic rays and hence their effect on gain. This model was developed in collaboration with Natalia Trela.

3.4.1 Trapped Ray Model

The initial design of the waveguide had a single side facet angled to 7° in an attempt to promote coupling of parasitic modes from the waveguide core and into the cladding where it will not affect the gain available for the resonator mode. Clearly, from the results in the previous section, a single 7° facet is not sufficient to suppress parasitic oscillation. To simulate these trapped rays, Zemax ray tracing software was used. Both the 6 mm and 12 mm wide waveguides were created in Zemax with a source file created in Matlab, generating any required number of rays within the core region with random placement and random initial angle, simulating spontaneous emission. Each ray was then traced until it no longer satisfied the TIR condition, at which point the ray would leak through one of the 6 surfaces of the core region to be lost into either the Indium at the heatsink interface or into air. This model was designed to only look at the degree of trapping within the core of the waveguide, and as such does not attempt to model gain, surface scatter, Fresnel reflection or leaky rays. Up to 100,000 rays were generated using Matlab and traced using Zemax with the path length of each ray measured using Zemax then imported into Matlab to allow

statistical analysis to be carried out. The greater the path length of a trapped ray, the more it is amplified, thus longer internal rays will reduce the gain significantly more than short path length rays. Figure 3.16 shows a sample ray trace for a single ray trapped within the waveguide core.

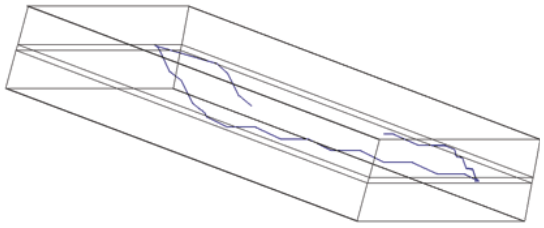

Figure 3.16 – Sample 3-dimensional ray trace of a trapped ray within the planar waveguide core. The ray can be seen to be trapped by reflection off both the Yb:YAG-Sapphire interfaces and the end/side faces of the waveguide structure.

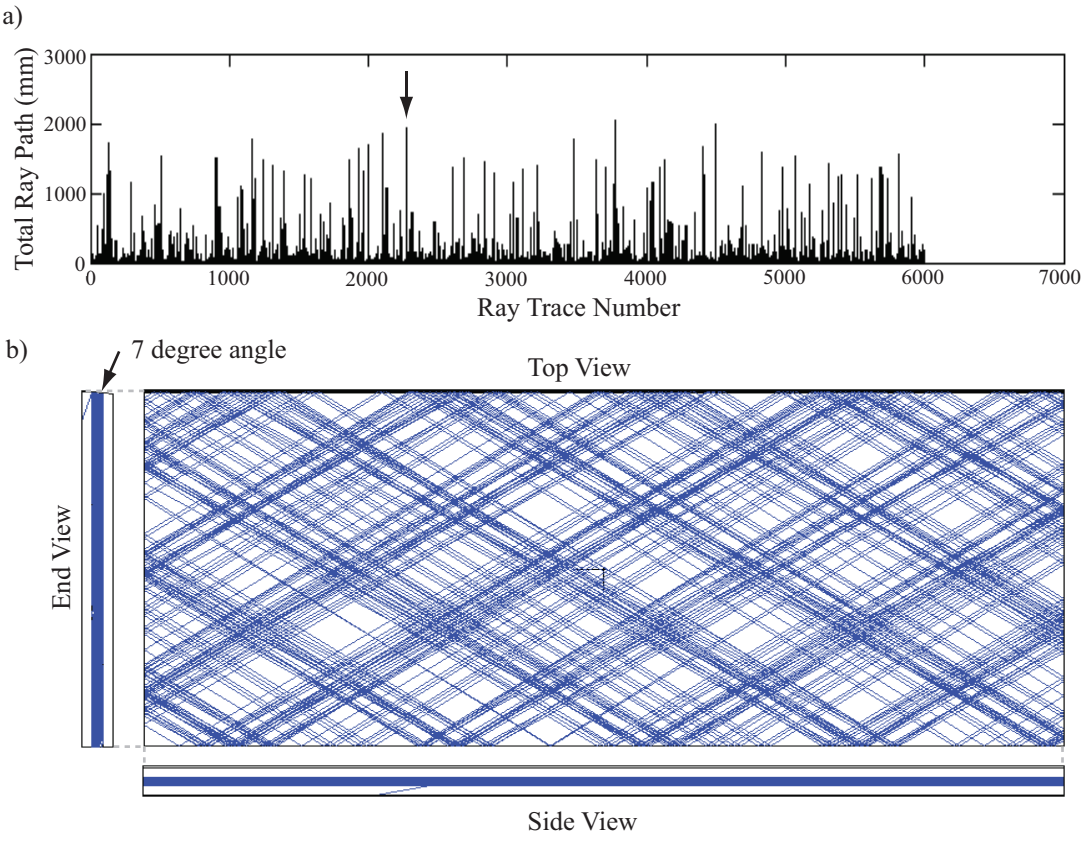

Figure 3.17 – Simulation of trapped rays within the 6 mm wide Yb:YAG planar waveguide with a single edge facet angled at 7°. a) Path length of each ray simulated within the waveguide core. b) Trajectory of single ray denoted with an arrow through the waveguide core.

Initially, we modelled the 6 mm wide waveguide with a single 7° with a sample of 6000 rays. The result of this can be seen in figure 3.17 a), this shows that many rays travel up to 1 m within the waveguide core, some may be even longer but the Zemax

limit of number of surface interactions per ray was reached for some of the longer rays. Each parasitic path length is considerably more than the 26 mm the round trip resonator gain length. Clearly from these results parasitic oscillation severely compete for the gain within the waveguide, causing a significant contribution to the poor laser efficiency. Figure 3.17 b) shows the trajectory of single parasitic ray through the waveguide core region, this shows a periodic pattern which could have a volume grating effect on the resonator mode due to the refractive index variations between the areas with gain and the areas depleted by the parasitic oscillation, further increasing the cavity losses.

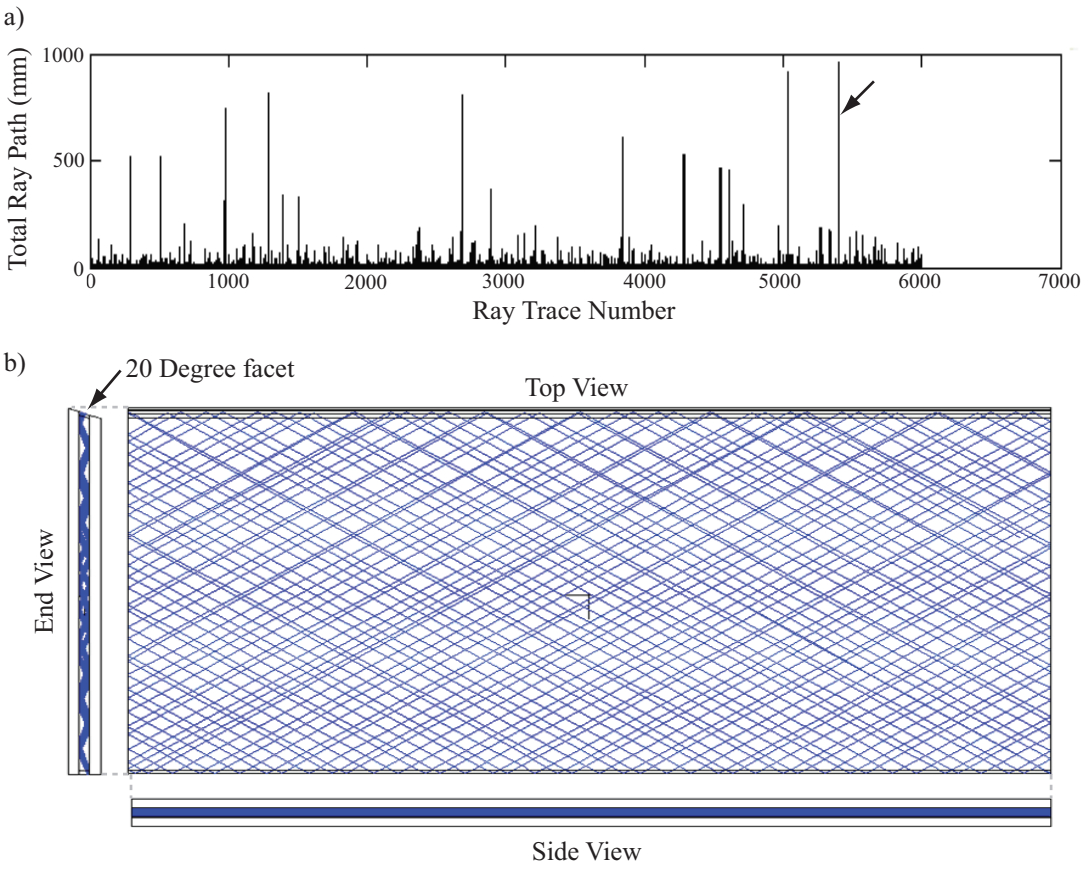

Figure 3.18 – Simulation of trapped rays within the 6 mm wide Yb:YAG planar waveguide with a single edge facet angled at 20°. a) Path length of each ray simulated within the waveguide core. b) Trajectory of single ray denoted with an arrow through the waveguide core.

We then adjusted the side angle of the waveguide progressively up to 20° to determine the degree of trapping with varying side angle. The result of a 20° side facet can be seen in figure 3.18. It can be seen that the degree of trapping is reduced, giving a maximum path length of ∼1m. However, there is still a significant number of rays with long path length. This model showed there was not a single angle at which trapping ceased, just a steady decreases in the average path with increased angle.

As varying the angle of a single facet will not sufficiently suppress the parasitic

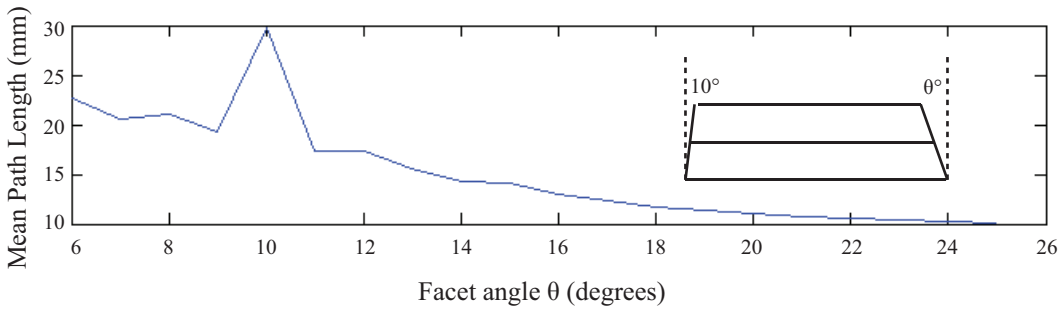

Figure 3.19 – Average ray path length for a 6 mm wide planar waveguide with one facet fixed at an angle of 10° whilst the opposite facet angle is varied, based on tracing 100000 rays.

oscillation, it is possible to vary the angle of both side facets. One facet was given a fixed angle of 10° whilst the opposite facet angled from 0 to 30°. Figure 3.19 demonstrates the effect of both facets angled, there is a clear increase when the facets are symmetric with the average path length dropping to ∼10 mm when the opposite facet is angled at 20°, with this being the maximum angle the waveguide could be adjusted too to still allow pumping into the facet. Each waveguide was then modelled with one facet remaining at 7° with the opposite facet at 20°, the maximum angle possible which can still be side pumped. Figure 3.20 shows a histogram of each ray's path length for both waveguides for 100,000 rays, showing the majority of the trapped rays to have a path length of <10 mm, effectively suppressing the parasitic oscillation within the core. The same modelling was applied to the 12 mm wide planar waveguide, giving very similar results.

This modelling has shown parasitic oscillation can be effectively suppressed by chamfering the edges of the planar waveguide. Other methods which have been utilised include rough grinding of the side facets [28], Sm:YAG claddings and notches cut into the sides of the waveguide. However, none of these methods are suitable for the Yb:YAG planar waveguide discussed here, roughening of the side facets would prevent side pumping, Sm:YAG does not absorb very well at 1030 nm, limiting it to Nd:YAG operation and notches cut into the side facets would affect both the side pumping and the unstable resonator alignment which utilises the full width of the planar waveguide.

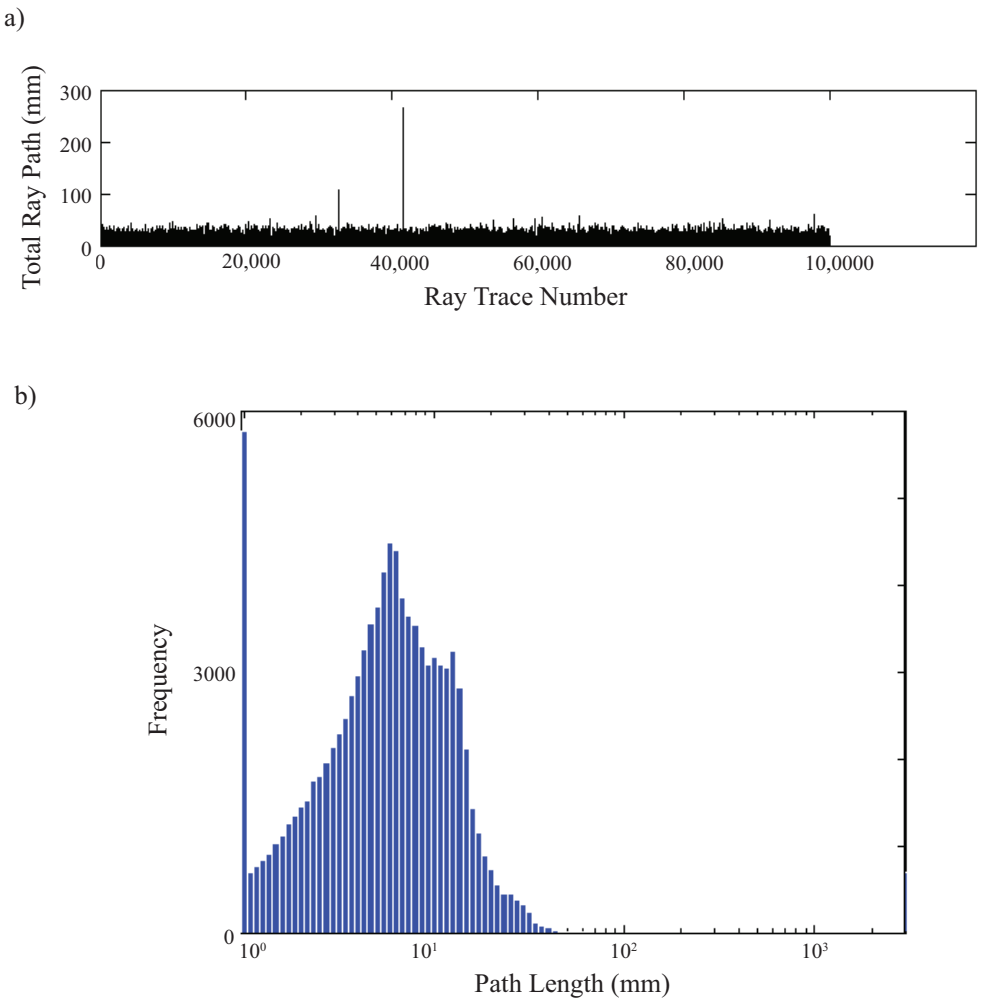

Figure 3.20 – Simulation of the 6 mm wide planar waveguide with one side facet at 7° whilst the opposite facet is angled to 20°. a) Path length of each ray. b) Histogram of ray path length.

3.5 Parasitic Suppressing Waveguides

The results from ray tracing of the Yb:YAG waveguide suggest that re-polishing the flat side facet to a 20° angle would effectively suppress the parasitic oscillation within the waveguide. Both 6 mm and 12 mm wide waveguides were sent to Leysop Ltd. for polishing work, both were polished to a 20° angle with surface finish of $\lambda/10$ and no AR coating applied to the freshly polished surface. The 6mm wide waveguide was built back into the heatsinks with pump unit 1 aligned for single sided pumping. The stable/waveguide resonator introduced in section 3.3.3 was then aligned to give the output curve shown in figure 3.22, giving a slope efficiency of 57% and 80 W output power with no parasitic oscillation detected. This gives a significant improvement over a single 7° edge with almost four times the output power achieved. This shows that considerable loss due to parasitic oscillation is removed from the laser with non-parallel chamfered edge facets.

Unfortunately, shortly after achieving these results one of the end laser facets failed, with the core damaging inwards over approximately one third of the width of the waveguide from a corner which had been damaged slightly from the re polishing process. After the facet was damaged, the laser continued to operate with reduced output power as shown in figure 3.22 and parasitic oscillation again building up with a threshold of 120 W. At low pump density, the damaged waveguide follows the undamaged output power, however, once the absorbed power reaches 120 W, the slope decreases due to the laser trying to operate in the damaged region. This is due to the Yb:YAG transparency threshold, as pump power is increased, gradually, more of the lateral width of the laser reached threshold allowing the laser to operate within this region. Eventually, the pump power is sufficient that the laser attempts to operate in the damaged region, however, due to the damage, only paths which avoid the damaged region can lase, resulting in low efficiency parasitic oscillation again taking place within the core.

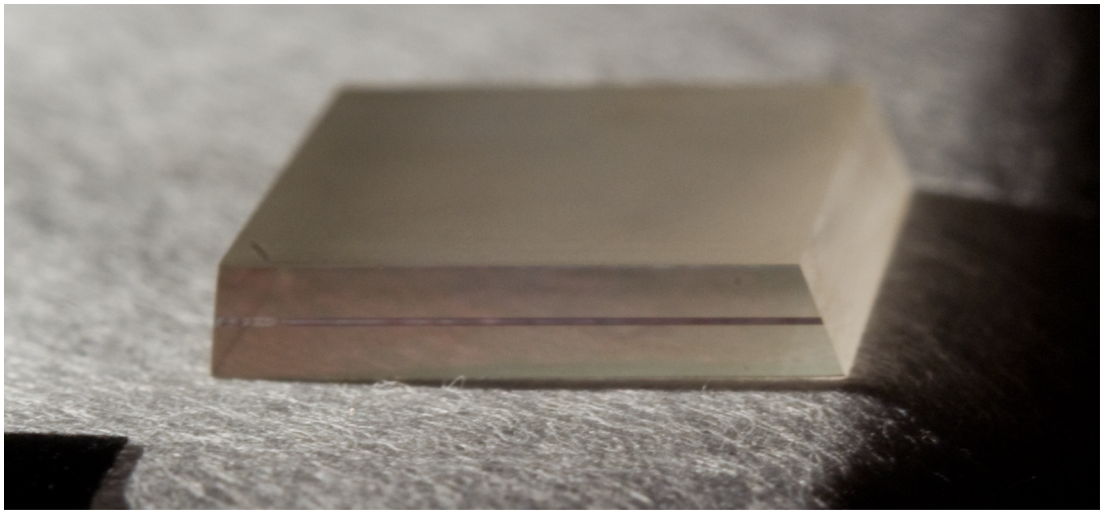

Figure 3.21 – The 12mm wide waveguide after polishing the second side facet to 20°

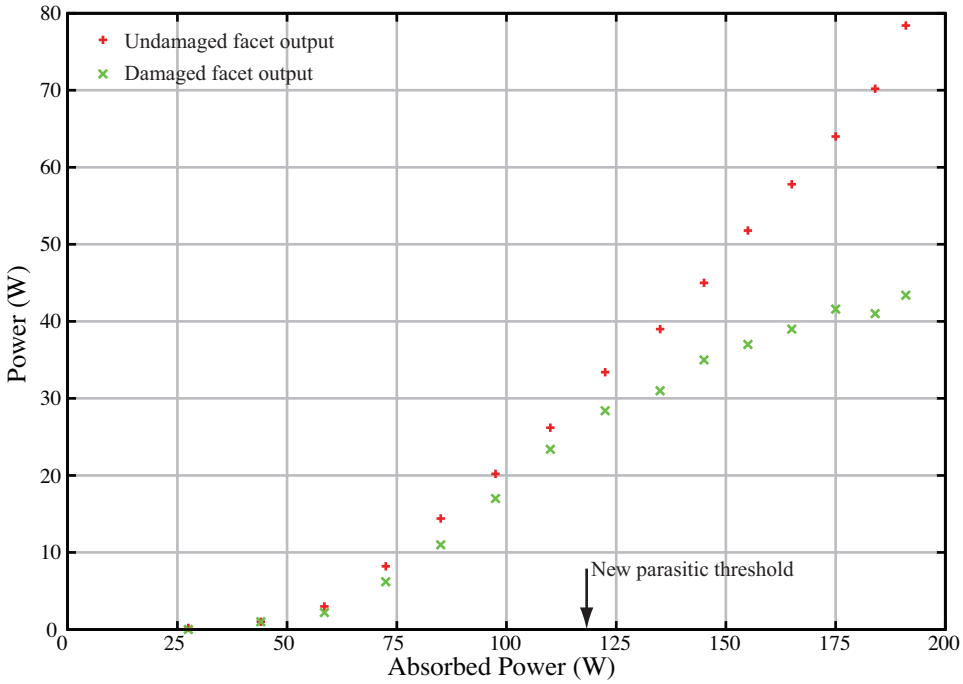

Figure 3.22 – Laser output power from the 6 mm wide planar waveguide, both before and after facet damage occurred.

3.6 Single-Sided Pumping of 12 mm Wide Waveguide

Due to the damage occurring to the 6 mm waveguide, the 12 mm waveguide was utilised. This section discusses operation of the 12 mm wide, width scaled planar waveguide under single-sided pumping conditions.

3.6.1 Hybrid Stable Waveguide Resonator

Pumping of the width scaled waveguide was achieved using the same alignment method as that used in the 6mm wide waveguide. Due to the additional width, 75% of the pump light is absorbed in a single pass at low diode currents, with up to 80% absorption achieved with a pump current of 90 A.

The stable/waveguide resonator was then aligned to the planar waveguide. The power transfer curve for this resonator can be seen in figure 3.23. An output power of 75 W was obtained with a threshold of 75 W absorbed power giving a slope efficiency of only 35%. The low efficiency can be accounted for in the difficulty aligning the waveguide resonator, with a 12 mm wide waveguide the R_z rotation axis of the mirrors is even less tolerant to misalignment than the 6 mm waveguide reported previously. The single sided pumping is also a significant source of loss, due to Beer's law absorption, it takes a significantly higher incident pump intensity to bring the full lateral width of the waveguide above the transparency threshold of Yb:YAG, resulting in large portions of the waveguide absorbing the 1030 nm laser light before

this threshold is achieved. Utilising this resonator, the laser gave a highly multi-mode beam in both the lateral and transverse directions.

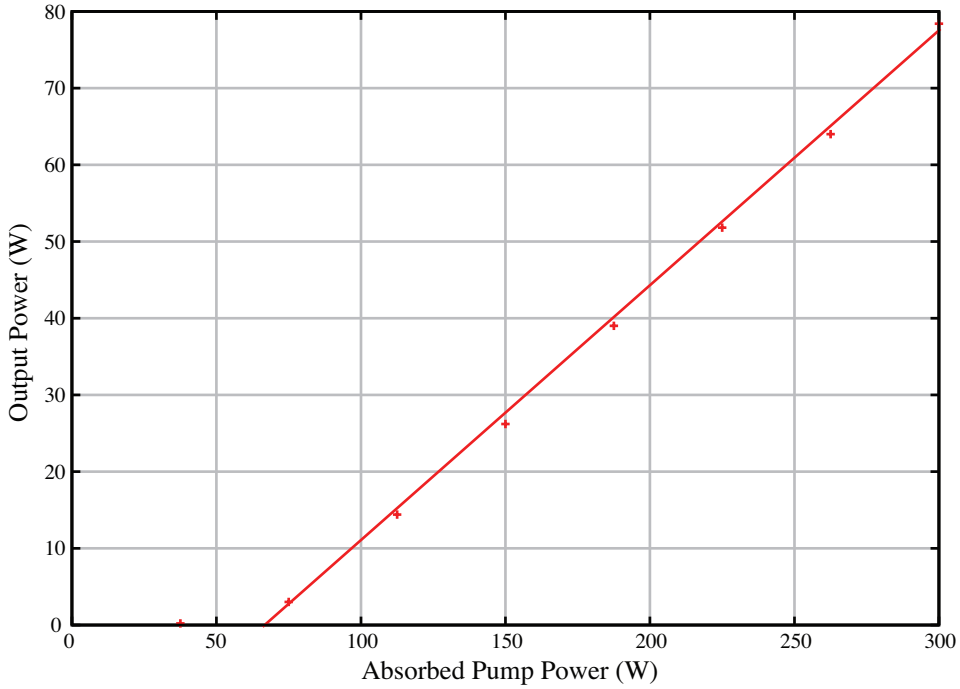

Figure 3.23 – Laser output power from the 12 mm width parasitic suppressed planar waveguide laser utilising the hybrid plane-plane case II resonator.

3.6.2 Lensed Hybrid Unstable Resonator

The lensed unstable resonator was aligned to the re-polished waveguide in an attempt to improve the lateral beam profile of the laser, but maintain the output power obtained from the waveguide/stable resonator with parasitic oscillation suppression. A power transfer curve can be seen in figure 3.24, this shows an output power of 100 W with a slope efficiency of 55%. In the lateral direction the laser had good beam quality, with a collimated divergence suggesting the confocal unstable resonator is operating correctly. In the transverse direction, the beam quality was extremely poor creating highly multi-mode vertical stripe, considerably worse than that seen in the transverse direction utilising the waveguide/stable resonator. The vertical stripe made up of many waveguide modes had a divergence angle (FWHM) of $\sim 45^{\circ}$ this is due to the difficulty in aligning the intra-cavity cylindrical lens causing high-order waveguide modes to be excited.

The laser threshold for this resonator is almost double that of the waveguide/stable resonator due to a combination of the cylindrical lens alignment and the non-uniform pump absorption laterally across the waveguide. A photon generated on axis in the unstable resonator sweeps out the whole width of the waveguide before it exits the resonator through the output coupling mirror edge. At low pump density, the whole

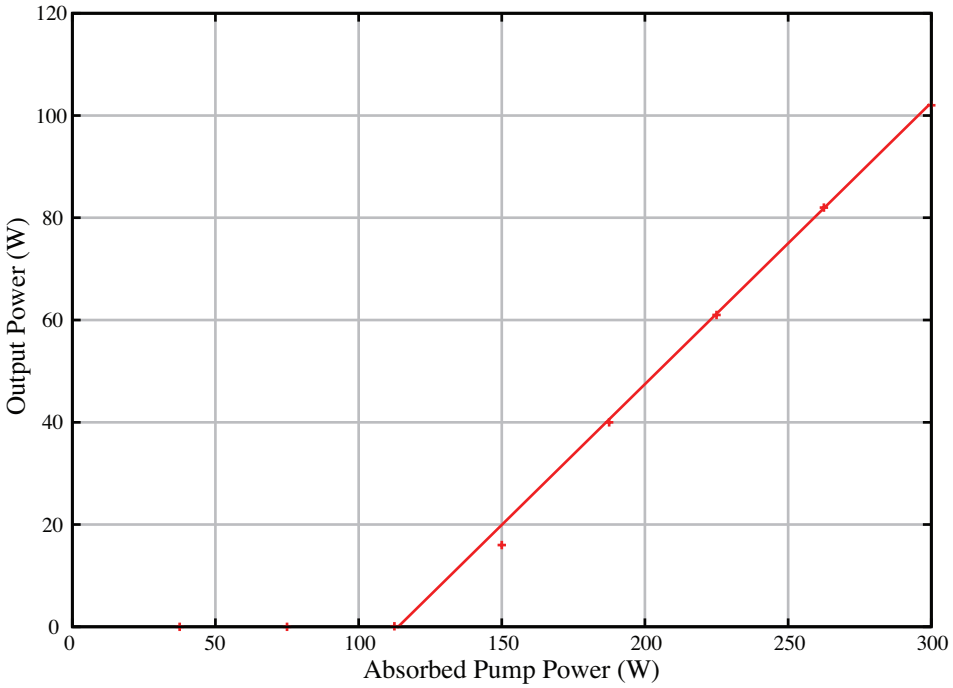

Figure 3.24 – Laser output power from the 12 mm width parasitic suppressed planar waveguide laser utilising the lensed hybrid unstable resonator.

waveguide is not above the transparency threshold of Yb:YAG causing regions of the waveguide to be absorbing, thus increasing the threshold for laser operation. The waveguide/stable resonator is not affected as significantly by this as it operates as a plane-plane cavity with the absorbing region effectively operating as a soft aperture within the laser cavity.

3.7 Conclusions

Within this chapter, novel diode pump units have been utilised to side pump an Yb:YAG, large-core, high-NA planar waveguide. The diode pump unit can provide more than 400 W into each waveguide side facet of dimensions 13 mm x 150 μm, with more than 90% of the pump light coupled into the waveguide core giving a pump absorption in a single-pass of 50% for a 6 mm width and 75-80% for a 12 mm width.

Initial results operating the system with a hybrid-unstable resonator showed poor efficiency due to parasitic oscillation reducing the available gain within the waveguide core. Zemax ray trace modelling showed re-polishing the side facets to 7° and 20° to effectively limit the path length of any trapped rays within the core. Both the 6 mm and 12 mm width planar waveguides were re-polished to these angles, resulting in suppression of parasitic oscillation.

Utilising the hybrid-unstable resonator with the re-polished waveguide resulted in a slope efficiency of 55%, considerably better than without parasitic suppression.

However, the output power was limited by a particularly high incident pump threshold due to the non-uniform pump absorption caused by Beer's law absorption under single-sided pumping. This resulted in area's of the waveguide absorbing the laser radiation at 1030 nm up until significant pump intensity is applied, bringing the full width of the waveguide above the transparency threshold. Additional intra-cavity losses are caused by the difficulty in alignment of cylindrical optics within the resonator.

The following chapter discusses the design of a new heatsink structure, allowing close-coupled resonator optics and eliminating the need for cylindrical optical elements, reducing resonator losses. Additionally, double-sided pumping is introduced to improve the absorption profile through the width of the waveguide to minimise losses due to the Yb:YAG transparency threshold.

Chapter 4

Pump Uniformity and Gain in a Double Side Pumped Yb:YAG Planar Waveguide

4.1 Introduction

Initial results from the Yb:YAG planar waveguide laser shown in chapter 3 show poor efficiency due to a combination of resonator losses and non-uniform pumping. Within this chapter, double-sided pumping is introduced to improve the uniformity of the gain distribution throughout the waveguide, doubling the power available for pumping and improving the pump uniformity. A redesigned waveguide heatsink was developed, allowing resonator mirrors to be placed close to the waveguide facets, reducing resonator losses, leading to highly efficient laser operation which is discussed in chapter 5.

The gain distribution within the waveguide core along with its pump power dependence is measured utilising a diode laser source at 1030 nm. The mechanisms which determine gain in the Yb:YAG planar waveguide are discussed and the effects upon the device under CW operation are investigated. The gain within the device should be maximised and evenly distributed throughout the core region so that the available power, $P_{avail} = g_0 \cdot I_s \cdot V$, is maximised, where g_0 is the small signal gain coefficient, I_s is the saturation intensity and V is the volume.

4.2 Improved Heatsink Design

Chapter 3 showed the current waveguide heatsink design to not be ideal. The overhang created by the excess metal-work prevents any optical surfaces from being placed close to the waveguide facets limiting the possible resonator configurations. Therefore a heatsink with considerably less excess material was designed. Figure 4.1 shows a diagram of the complete heatsink structure.

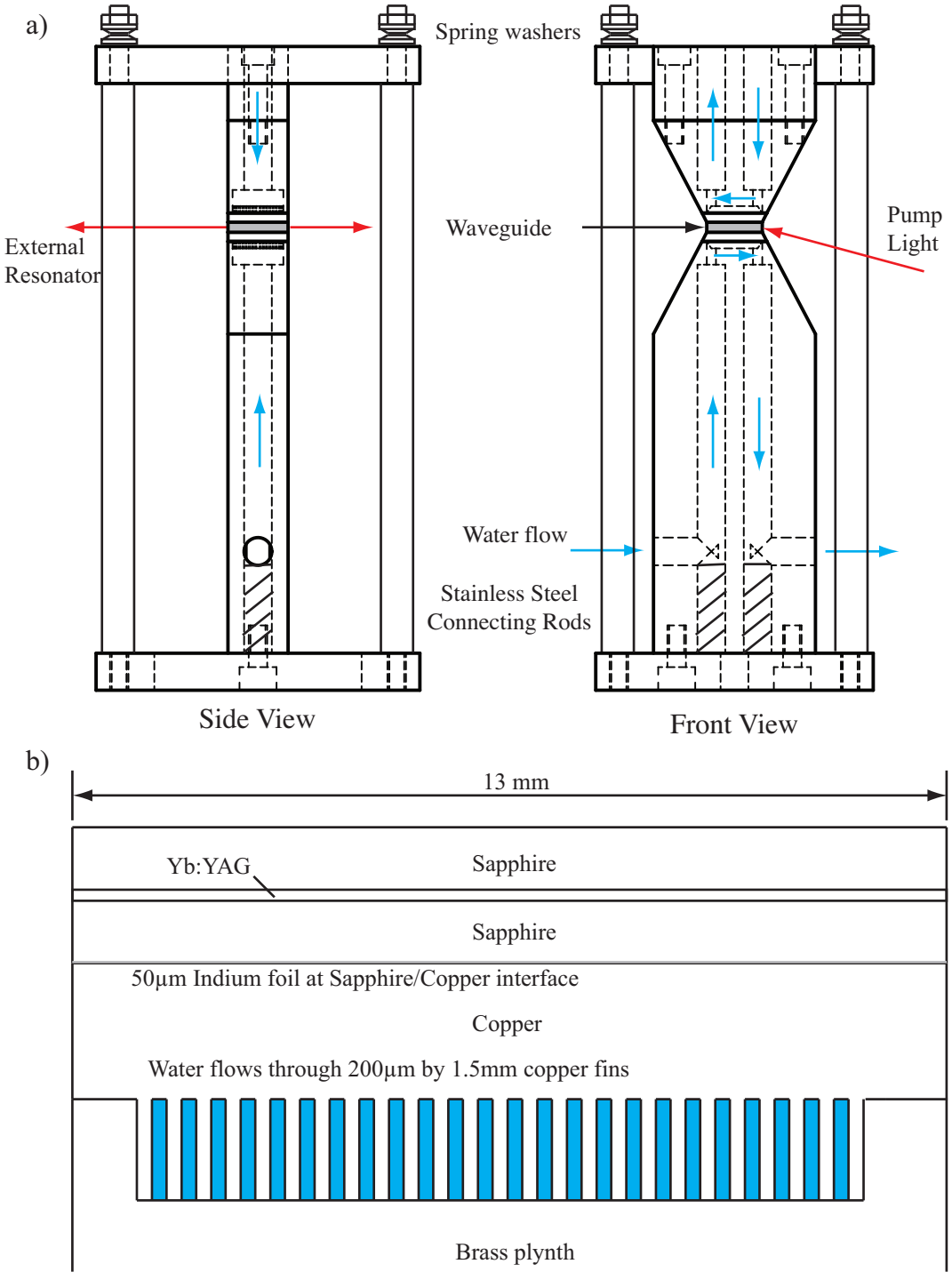

Figure 4.1 – a) Structure of the complete heatsink structure. b) Detail of the heatsink - waveguide interface, 50 μm thick indium foil aids in thermal transfer. The copper top cap with fins is soldered into place on the brass plinth.

The new heatsinks were designed to be flush with the laser facets of the planar waveguide, allowing optics to be placed near the waveguide facets. This limits the size of the metalwork available to 13 mm in the longitudinal direction. The original heatsinks also caused issues with the pump unit angle. If the pump angle is too steep, it is impossible to bring the diode emission into focus on the side facets due to the gold side reflectors of the pump unit colliding with the heatsinks. Due to this constraint, a tapered design was chosen to allow for maximum width at the base of the heatsink giving sufficient space for water cooling connectors whilst minimising the width near the waveguide, preventing collision with the pump units.

Micro-channel copper coolers were utilised for the new heatsinks, similar to those used in the previous design, giving improved cooling with less area of heatsink. The copper micro-channels were created using a diamond saw, giving 200 μm wide fins, the top cap of each heatsink was then soldered into place. Each copper surface in contact with the waveguide was lapped giving a very smooth parallel surface for contact with the waveguide. 50 μm thick indium foil was used at the interface between the copper heatsink surface and the sapphire of the planar waveguide to improve thermal conductivity. The heatsink structure comprises of identical top and bottom parts, with the bottom mounted to a plinth with water flowing through it. The top heatsink is held in place through 4 threaded stainless steel rods combined with a pair of spring washers and a nut, allowing the top heatsink to self-align to the waveguide and press the indium foil with a force of 340 N, sufficient for the indium foil to flow. Due to the reduced length of the heatsink, the water flow was changed from longitudinal to lateral flow with the top heatsink having opposite lateral flow to the bottom heatsink. Thus minimising any thermal gradients which may form within the waveguide due to non-uniform cooling.

Thermal analysis of the heatsink structure using Flex-PDE finite element analysis software was carried out to determine the temperature rise in the waveguide core and if any hot spots occur under intense pumping. Hot spots were expected as the new heatsink design does not have copper micro-channels extending to cover the full area of the waveguide due to the reduced longitudinal length. To model the heatsink, a Gaussian heat source emitting 150 W was inserted into the waveguide core. Figure 4.2 b) shows a vector diagram of the heat transfer through the structure, whilst figure 4.2 a) shows a contour plot of the temperature rise within the structure. These figures show a uniform heat flow away from the waveguide structure, creating no hotspots in the Yb:YAG core and a maximum temperature rise of 50°C to 70°C from room temperature. However, the quantum defect causing direct heat generation within the Yb:YAG is only $\sim$11% of the $\sim$1 kW of pump light under double-sided pumping, slightly less than the 150 W used in the model. A higher value was chosen to compensate for the possibility of impurity quenching occurring within the core,

which is discussed in detail in section 4.4.3.

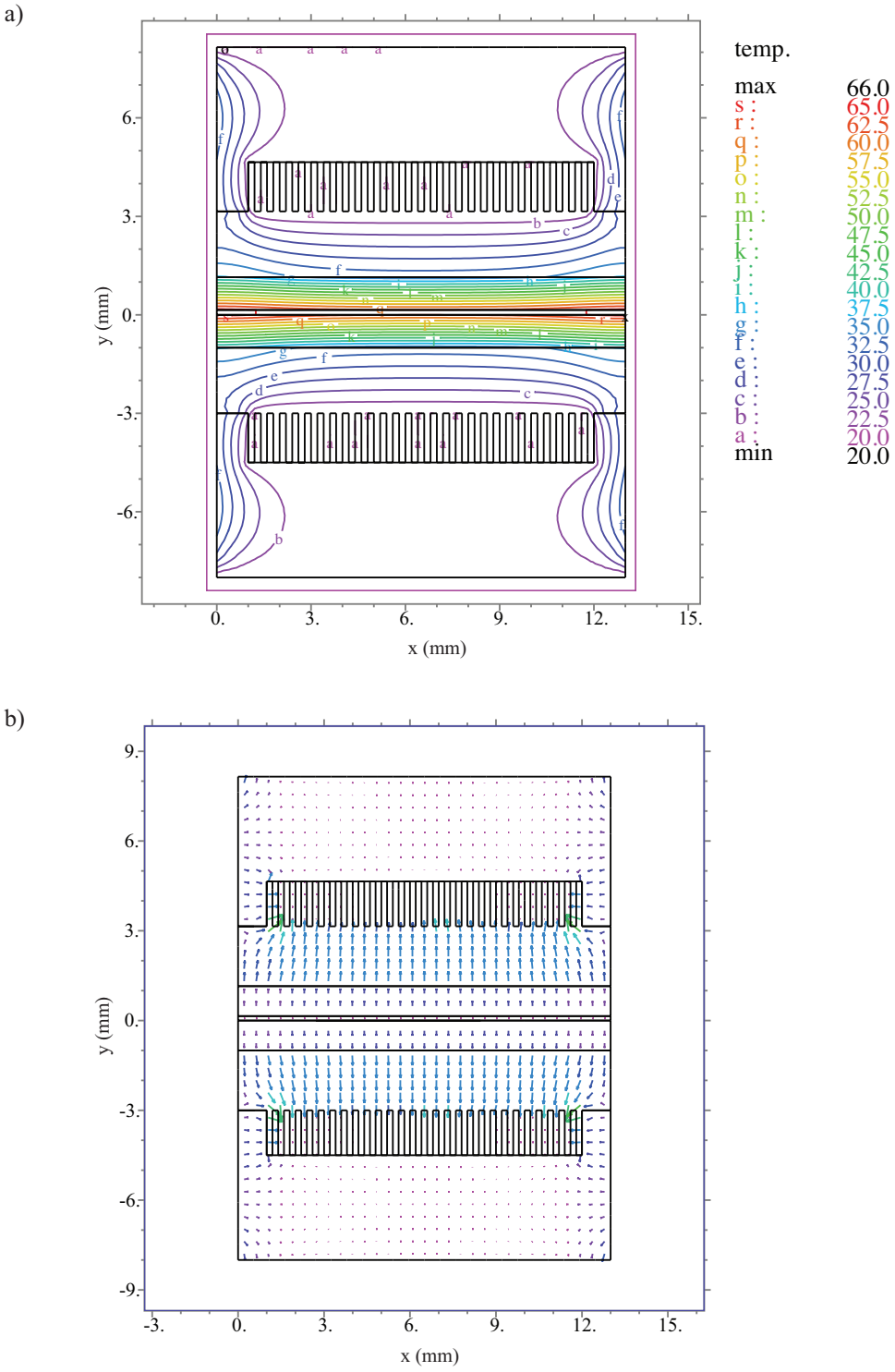

Figure 4.2 – Thermal modelling of the heatsink structure. a) Shows a contour plot of the steady state temperature through the waveguide and heatsink structure with a 150 W heat source within the waveguide core. b) Shows a vector plot of the heat flow leaving the waveguide core and entering the water flowing through the micro-channels which are held at 20°C by the constant coolant flow.

4.3 Double-Sided Pumping

This section details improvements to the pump uniformity in the lateral direction within the waveguide. As shown in the previous chapter, the laser has a particularly high threshold, due to a combination of resonator losses and lack of pump uniformity. Due to the 3-level nature of Yb:YAG the transparency pump intensity must be reached so the gain medium is no longer absorbing at the laser wavelength. By improving the lateral pump uniformity, this absorbing region can be reduced, also creating a uniform gain profile through the lateral width of the waveguide. This section discusses the pump alignment and absorption properties of a double-edge-pumped Yb:YAG planar waveguide.

4.3.1 Second Pump Unit Alignment

The second of the two pump units described in the previous chapter is used as a pump source for the 20° edge facet. The second pump unit is aligned parallel to the optical table in the vertical plane, preventing the transmitted light through the waveguide from entering the opposite pump unit's diode facets and vice versa. This angle was chosen through trial and error, leaving the original pump unit at the required angle and varying the angle of the second unit until light no longer struck the opposite diode facets. The re-polished edge angle at 20° is no longer AR coated, the reflection from this facet for the TM polarisation of the laser diode as a function of angle can be seen in figure 4.3. This figure was produced using the Fresnel reflection equations given by Hecht [73]. This shows a reflection of 7% for an incident pumping angle of 20°, which can be as much as 35 W reflected back from the facet requiring a beam dump to catch this stray radiation. A photograph of the both pump units aligned to the planar waveguide housed in its new heatsink can be seen in figure 4.4.

The second pump unit alignment was optimised using a fluorescence imaging technique. This is due to it not being possible to monitor the waveguide pump absorption using a power meter as before, therefore a technique to monitor the fluorescence emission and hence the diode alignment was developed. This technique utilised a CCD camera imaging the waveguide end facet as shown in figure 4.5, with a 1030 nm bandpass filter (10 nm FWHM) and variable ND filters attached to the imaging lens.

The image from the camera was observed using Spiricon beam profiling software with a software aperture created around the waveguide region. The intensity within this region is then monitored as the diode stack angle and position is varied with a maximum intensity corresponding to maximum diode absorption. Spiricon data shows each pump unit causes approximately the same intensity of fluorescence at 1030 nm

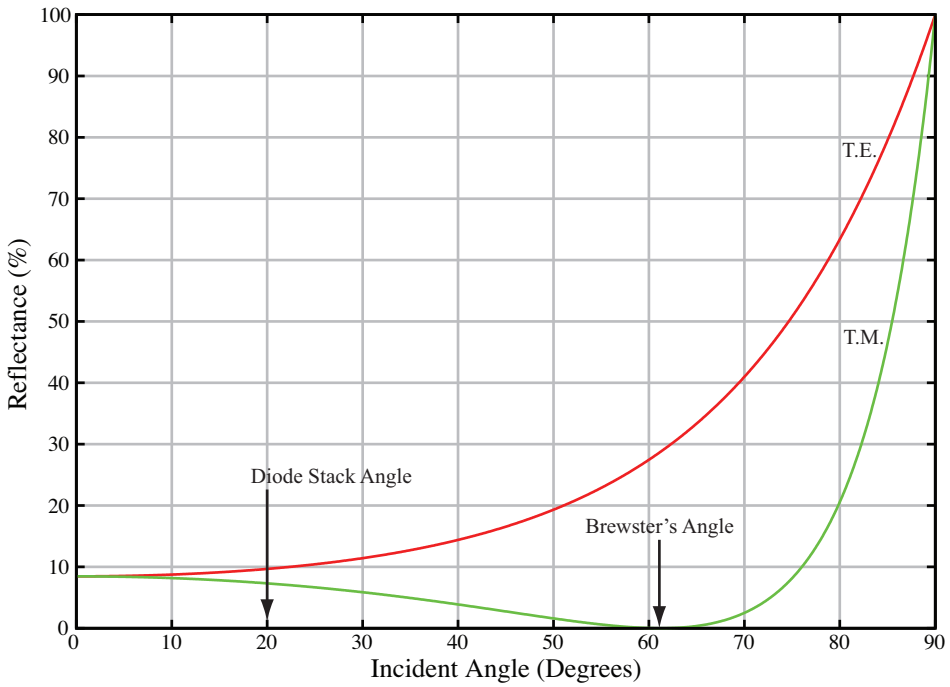

Figure 4.3 – Percentage reflection of diode pump light from non-AR coated waveguide facet for both T.E. and T.M. polarisation. The diode stacks used to pump the Yb:YAG waveguide are polarised in the T.M. direction.

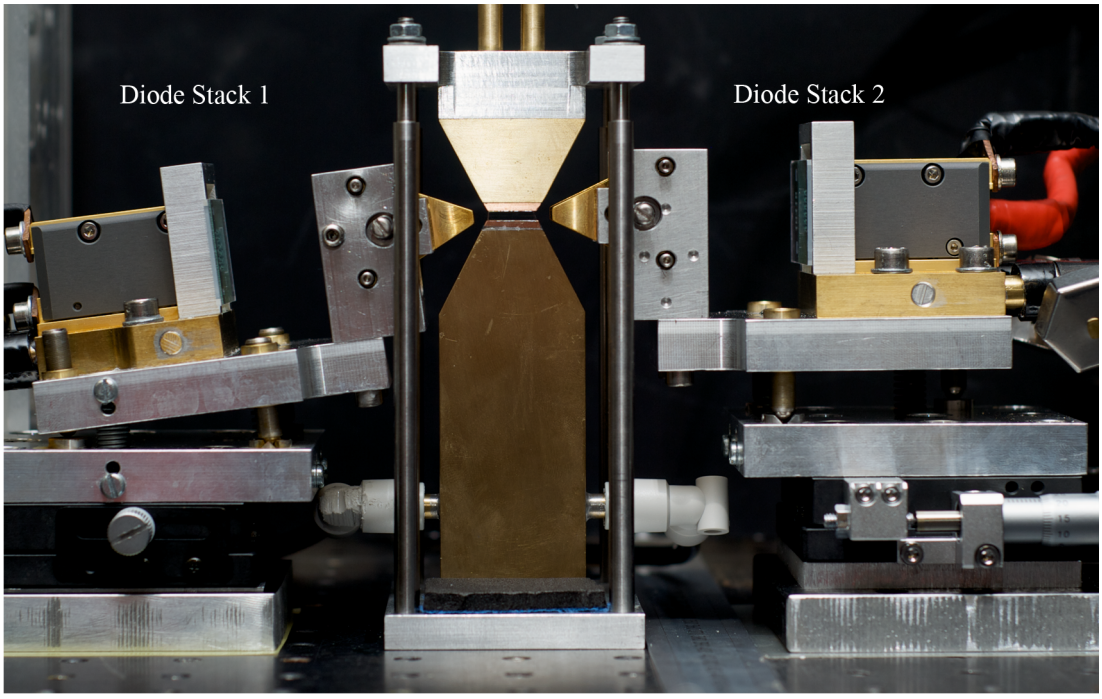

Figure 4.4 – Double-sided pumping of the Yb:YAG planar waveguide housed in improved heatsinks.

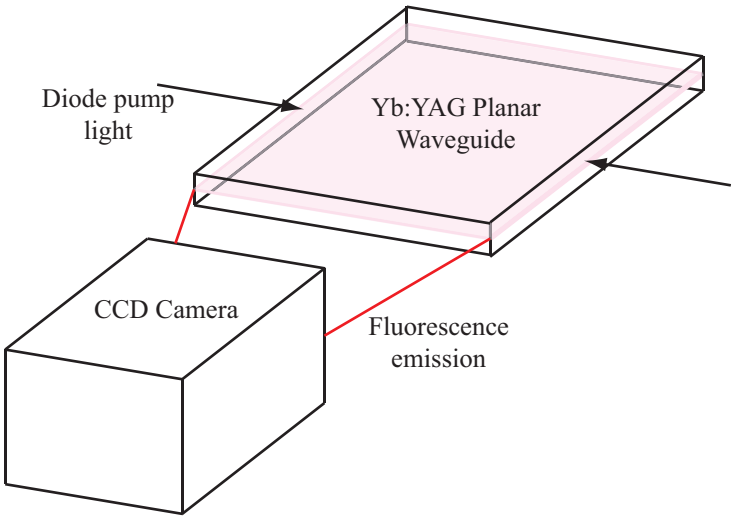

Figure 4.5 – Fluorescence imaging of the waveguide facet for diode alignment using a CCD camera.

when they are operated at the same pump current.

4.3.2 Absorption Profile

The measured fluorescence across the waveguide facet using the imaging technique described above gives an approximation to the pump absorption profile within the waveguide core. An error in the profile is introduced by the use of a standard 35 mm camera lens due to perspective. This perspective shift causes the peak at either side of the waveguide to be artificially high as the camera is effectively looking at the entire side facet rather than just the profile in the plane of the laser end facet. This technique could be improved through the use of a telecentric imaging lens. Figure 4.6 shows the lateral fluorescence profile through the waveguide core, giving an approximation of the absorption profile for both single-sided pumping with each diode stack and double-sided pumping. The experiment was then repeated by imaging the waveguide side facets to show the longitudinal absorption profile which can be seen in figure 4.7. This shows a flattened Gaussian-like absorption profile throughout the length of the planar waveguide.

As the power in the transmitted, non-absorbed light under double sided pumping can not be measured under double-sided pumping conditions, the amount of pump absorption is unknown. Ignoring any possible pump saturation effects under intense double sided pumping, the pump absorption is taken to be 75%, the same as measured for low-intensity single-sided pumping. At high pump intensity, the onset of pump saturation will prevent the absorption from increasing to 80% due to diode wavelength tuning as it did for single-sided pumping, therefore, it is assumed that the pump absorption remains at 75%.

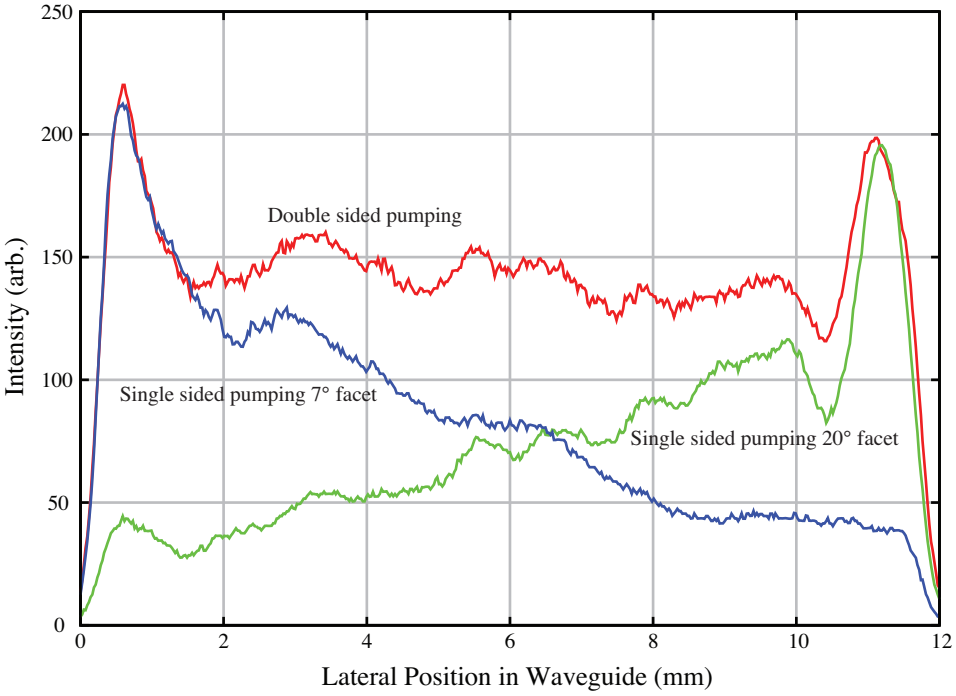

Figure 4.6 – Fluorescence profile at 1030 nm in the lateral direction with single sided pumping into the 7° facet, 20° facet and double sided pumping with the diode stacks operating with a 90 A pump current, resulting in 400 W incident for single sided pumping and 800 W for double-sided pumping.

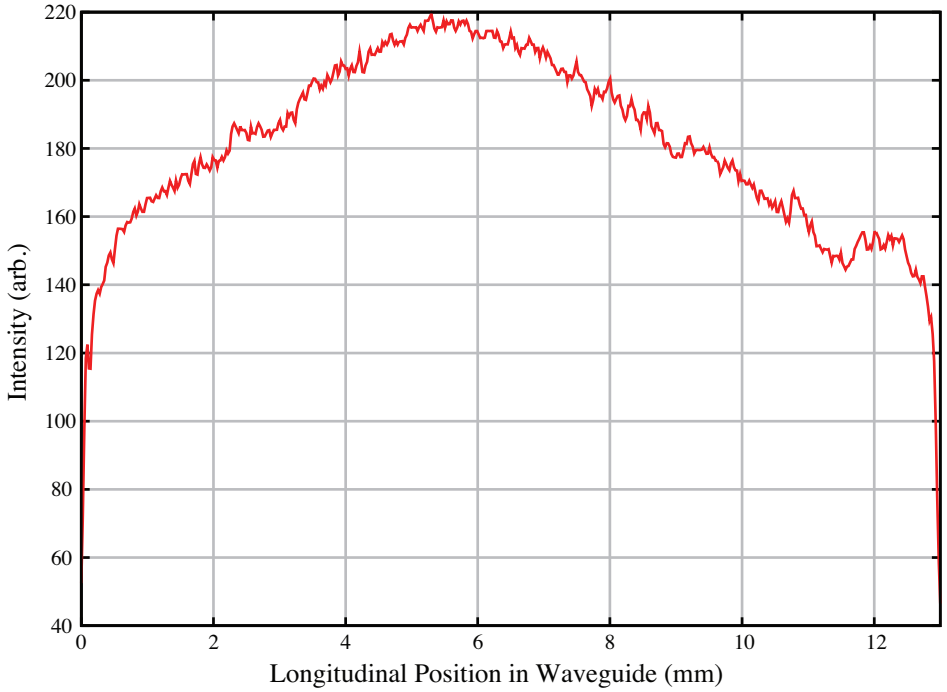

Figure 4.7 – Fluorescence profile at 1030 nm in the longitudinal direction through the waveguide measured at the 7° side facet with diode stack 1 operating with 90A diode current.

4.4 Issues Affecting Gain in Yb:YAG Planar Waveguide Lasers

The issues affecting gain in the Yb:YAG planar waveguide laser are discussed in this section. There are four processes which can negatively affect the gain available within the laser, these are due to 1) pump saturation, 2) heat generation, 3) parasitic oscillation clamping the gain and 4) emission at wavelengths other than the desired laser wavelength. Parasitic oscillation has already been discussed and suppressed in chapter 3. Heat generation through the quantum defect and emission in the green due to two-ion co-operative luminescence are discussed.

4.4.1 Pump Saturation

Due to terminal level thermal population in the quasi 3-level Yb:YAG laser system, it is only possible to excite a certain maximum fraction of Yb^{3+} active ions into the upper level and only extract a certain maximum fraction of this excited fraction. These fractions have been calculated by Krupke *et al.* [41, 74]. and are shown in figure 4.8. The saturation intensity required to extract the maximum excited fraction is given by equation 4.1 and is calculated to be $I_{p,sat}$ =28 kWcm^{-2} [41].

$$I_{p,sat} = \frac{hc}{\lambda_p \sigma_p \tau} \tag{4.1}$$

Where λ_p is the pump wavelength, σ_p is the pump transition cross section and τ is the upper laser manifold lifetime.

To determine experimentally whether pump saturation is occurring, the power in the IR fluorescence was measured with varying pump diode current. If the fluorescence power flattens with increased pump power this suggests pump saturation is occurring. An $f = 25.4$ mm lens was placed 25.4 mm from a waveguide laser facet, this allowed all the fluorescence emitted from one laser facet to be coupled onto a power meter. A baffle was placed around the lens to prevent any stray pump light or heat from giving a false reading on the thermal power meter. A RG850 filter was then placed immediately after the lens limiting the power meter to measuring only the IR. The experimental configuration can be seen in figure 4.9.

The fluorescence output power for both single and double sided pumping can be seen in figure 4.10. This shows a flattening of the output power curve when double sided pumping is used, it does not completely flatten suggesting that the waveguide is only approaching saturation and not completely in the saturation regime. It could also imply ASE is occurring. With high gain, a single photon emitted at one side of the waveguide can be amplified before it reaches the other side of the

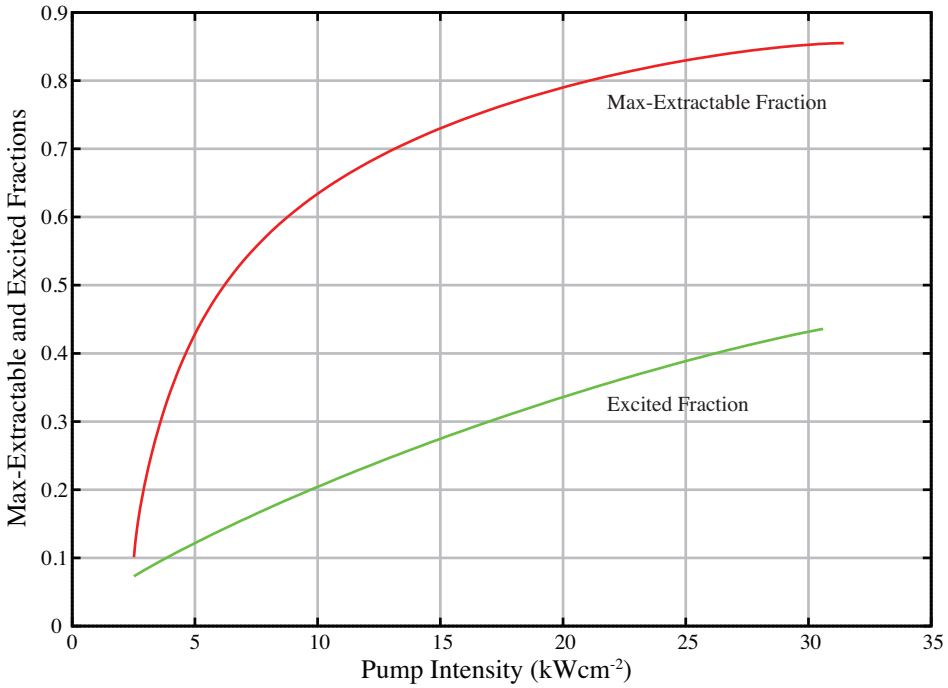

Figure 4.8 – Figure and caption extracted adapted from reference [41]. Maximum extractable fraction and excited fraction of manifold populations in Yb:YAG as a function of pump intensity for 941 nm pump transition.

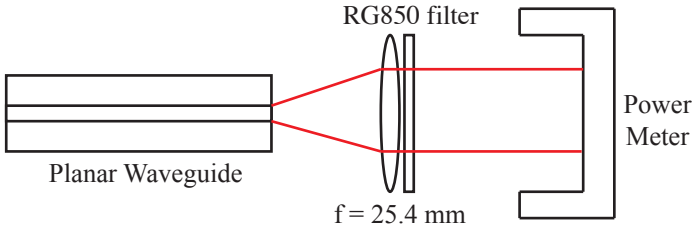

Figure 4.9 – Experimental configuration to measure the fluorescence power from one laser facet.

waveguide, extracting population from the upper state and depleting the population inversion causing a reduction in gain. This would appear as an increase in fluorescence power output from the waveguide after saturation has occurred, similar to that caused by parasitic oscillation. However, the reduction is considerably less than parasitic oscillation due to the shorter path length involved in ASE compared to parasitic paths.

This experiment was then repeated using an Ocean Optics HR4000 spectrometer and monitoring the intensity of three peaks in the fluorescence with increasing pump current. This allowed monitoring of multiple wavelengths to determine if wavelengths, which are amplified considerably less than the 1030 nm peak exhibit the same constant increase in fluorescence output as observed above. The three peaks monitored were the 970 nm zero phonon emission; the 1030 nm peak emission; and the 1050 nm emission. The stimulated emission cross-section for 970 nm and 1050 nm are both

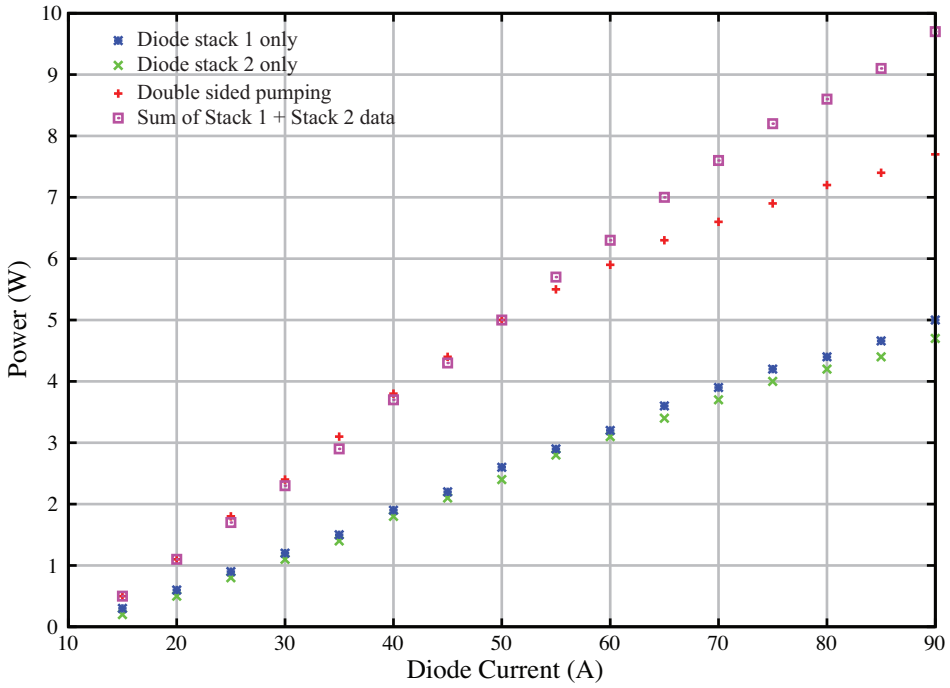

Figure 4.10 – Fluorescence power at wavelengths >850 nm for increasing diode pump current. Single sided pumping shows a linear response, whereas double sided pumping shows the onset of pump saturation at a pump current >60 A.

considerably less than the cross-section at 1030 nm. The data from the spectrometer was then normalised with all three peaks plotted on a semi-log graph shown in figure 4.11. This data shows the same change in curve as seen in the power measurements in figure 4.9 for the 1030 nm peak. The 970 nm and 1050 nm emissions do however flatten completely. This suggests that the steady increase in intensity of the 1030 nm emission after the change in slope at >60 A due to pump saturation is caused by ASE, as 1030 nm is amplified significantly more than the other wavelengths due to the greater emission cross-section occurring at this wavelength. A normalised plot of the complete emission spectra from the waveguide for various pump current can be seen in figure 4.12. This shows a narrowing of the 1030 nm peak with increased pumping suggesting the onset of ASE.

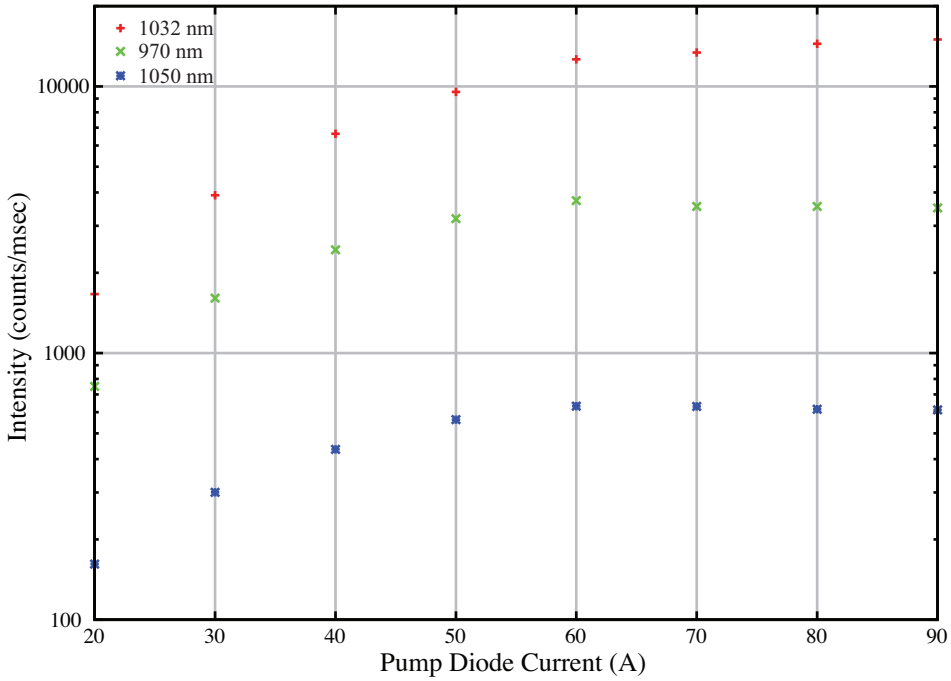

Figure 4.11 – Intensity of various wavelengths of fluorescence with varying diode current. Above a diode current of 60 A (both stacks operated with matched current) the emission intensity flattens due to the onset of pump saturation.

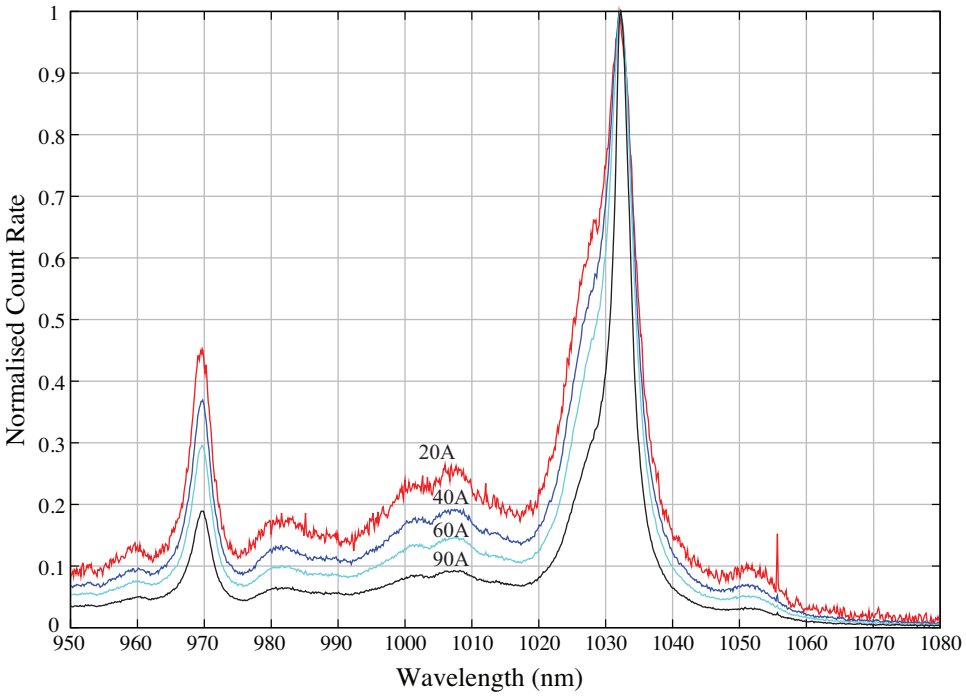

Figure 4.12 – Fluorescence emission spectra for Yb:YAG planar waveguide with varying diode pump current. 90 A represents both diode stacks operating with a 90 A pump current, resulting in 800 W at 940 nm incident on the waveguide side facets.

4.4.2 Heat Generation in Yb:YAG

The major contribution to heat generation in Yb:YAG is due to the quantum defect. Figure 4.13 shows the three-level Yb:YAG laser system with pump absorption from the ground state, $^2F_{7/2}$ (0 cm^{-1}), to the upper pump absorption level, $^2F_{5/2}$ (10624 cm^{-1}) for diode pumping at 941 nm [75]. Stimulated emission occurs between the $^2F_{5/2}$ (10327 cm^{-1}) upper level and $^2F_{7/2}$ (612 cm^{-1}) lower level giving emission at 1030 nm. The extra energy in the system between the upper pump level and the upper stimulated emission level is released in the form of phonons, causing heating of the laser crystal. The quantum defect is defined by the difference between the emitted and pump photon energies with a fractional value of 0.11, considerably less than that of Nd:YAG at 0.24 [76].

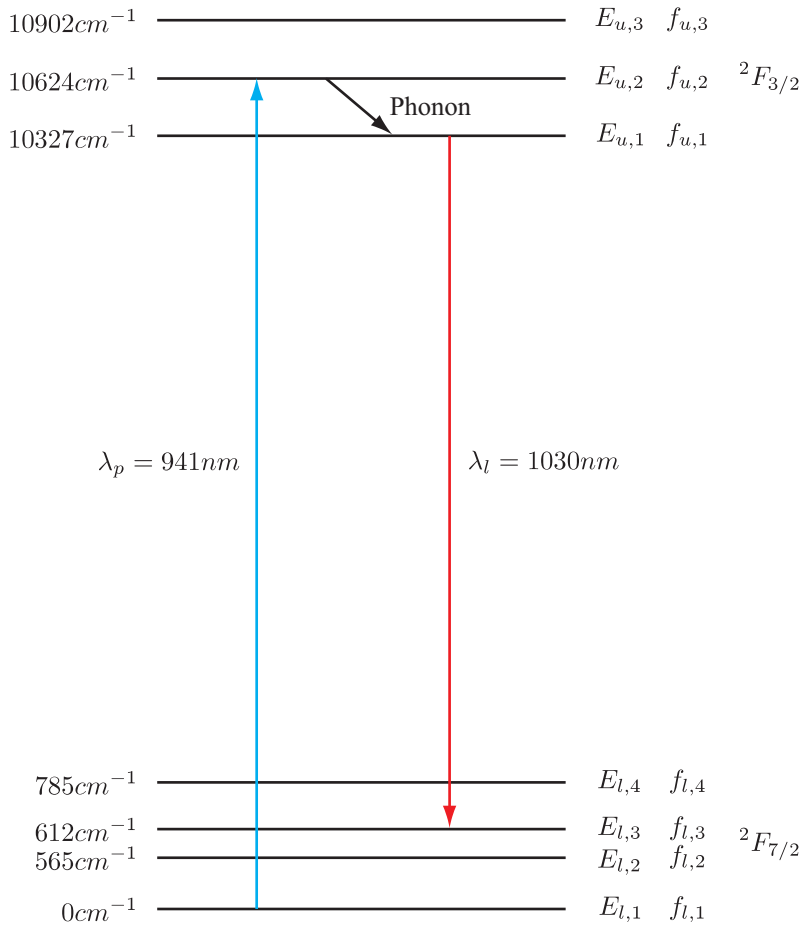

Figure 4.13 – Energy level diagram of the 3-level Yb:YAG laser system.

The quantum defect in Yb:YAG may be reduced by pumping the zero-phonon absorption at 970 nm, which has similar absorption cross section to the 941 nm absorption. The absorption peak at 970 nm has a much smaller spectral bandwidth than the absorption peak centred at 941 nm which is considerably more difficult to pump, requiring the need for a wavelength-locked diode laser source. Hence, only pumping at 941 nm will be discussed.

Cross relaxation is a common source of waste heat in Nd:YAG with crystals doped higher than 1 at. % , due to energy transferring between active ions in the lattice and quenching to a lower energy level and then relaxing to ground through phonon emission. At first sight, it does not appear that quenching can occur in Yb:YAG crystals due to the lack of intermediate energy levels. However, defects due to impurities can cause a quenching effect, as discussed in the following section.

4.4.3 Quenching

Under intense pumping, the Yb:YAG planar waveguide is seen to glow a very intense blue-green colour, suggesting an up-conversion process is taking place within the crystal causing a reduction in gain and hence laser efficiency. This section characterises this green emission and suggests possible explanations for its presence.

An Ocean Optics USB2000 spectrometer was used to obtain a visible emission spectrum from the waveguide. To do this, the fibre coupled spectrometer was positioned to couple light from the centre of one laser facet with a BG38 filter and hot mirror placed between the waveguide and the fibre, preventing any 940 nm pump leakage which can cause the spectrometer to saturate. The emission spectra was then measured with double-sided pumping at a range of pump current. Figure 4.14 shows the visible emission spectrum with a diode pump current of 90 A. This shows a broad peak centred around 510 nm with a strong peak in this feature at 500 nm and another strong feature at 514 nm. Another, weaker peak can be seen at 485 nm with a second weak peak seen as a shoulder on the broad curve at 525 nm. The spectrometer data for each pump current was normalised, showing the shape of the green emission does not change with increasing pump, unlike the IR emission shown in figure 4.12. The intensity of the 500 nm and 514 nm peaks has been plotted against diode pump current in figure 4.15. This shows the green emission also saturates with a pump current above 60 A and tracks the IR emission, suggesting that green ASE is generated after pump saturation.

Emission in the green has been observed previously from Yb:YAG lasers, and is usually attributed to impurities within the crystal structure [77]. Due to the long upper state lifetime in Yb:YAG, energy migration from one Yb^{3+} to another is very common which can lead to energy being transferred to another impurity ion within the crystal lattice. Impurities in Yb:YAG, typically come from the Yb oxide used in the growing of the crystal structure with impurities being from the Lanthanide series, commonly the Ho^{3+}, Er^{3+}, Tm^{3+} and Pr^{3+} ions. Due to this energy migration process, use of Yb^{3+} is very common in making Yb:Ho:YAG and Yb:Er:YAG co-doped upconversion lasers. The Yb^{3+} ion is used as a sensitiser for the Er^{3+} and Ho^{3+} ions due to the difficulty in pumping to the level required to obtain direct green emission.

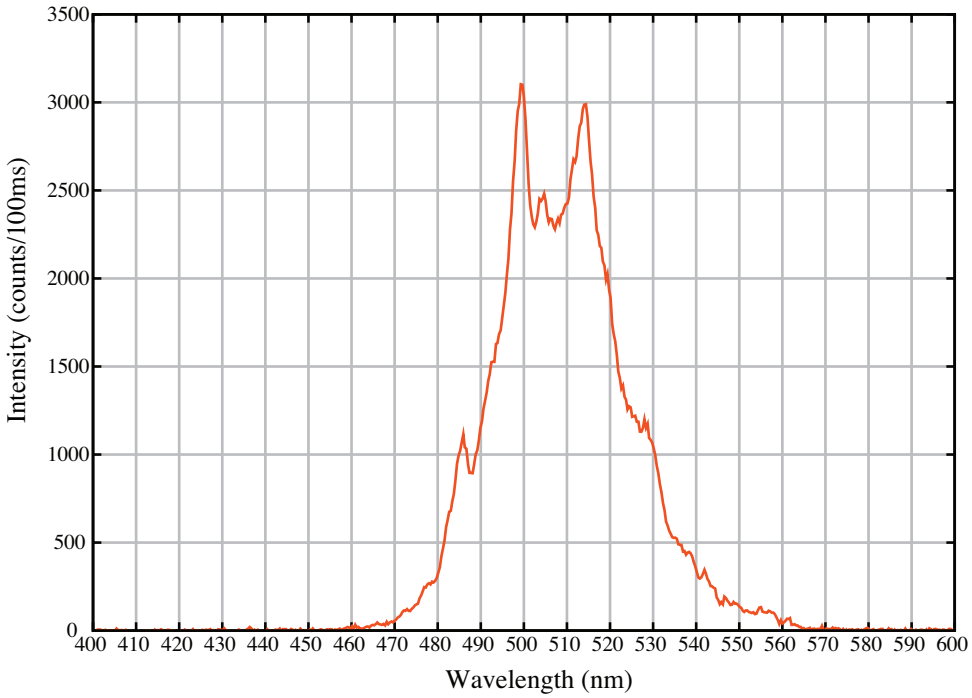

Figure 4.14 – Fluorescence emission spectra of the Yb:YAG crystal taken with an incident pump power of 800W.

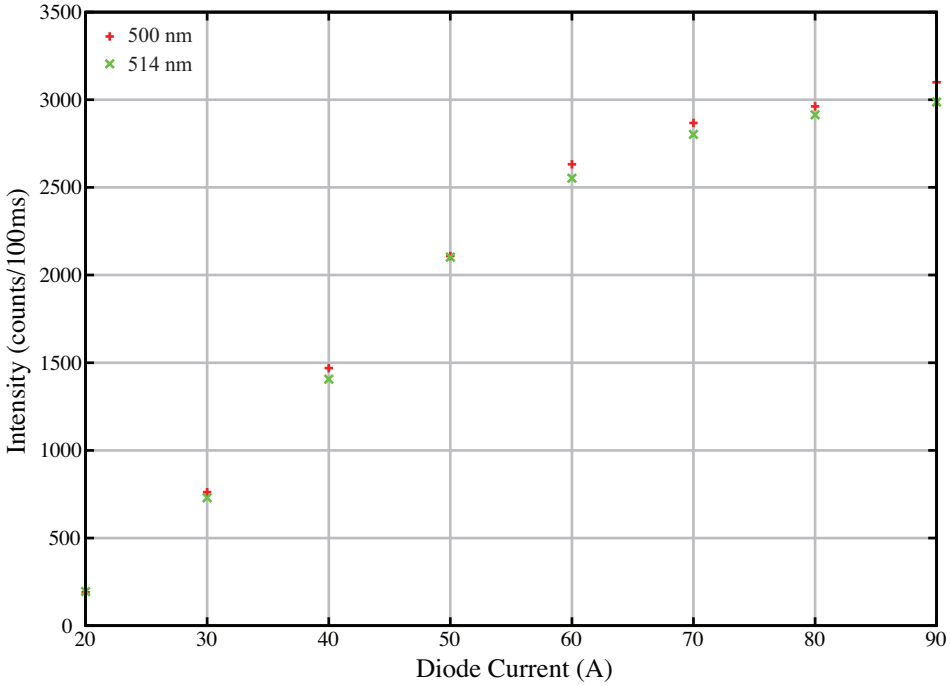

Figure 4.15 – Green fluorescence emission as a function of diode pump current.

The Yb^{3+} is pumped directly at 940 nm, energy from the upper state of the Yb^{3+} is then transferred to an intermediate state in the Ho^{3+} or Er^{3+}. This intermediate state is then excited by another pump photon to a higher level, resulting in laser emission at 525 nm [78] and 540 nm [79] for Yb:Ho:YAG and 545 nm in Yb:Er:YAG crystals [77]. This process is known as stepwise upconversion. Figure 4.16 shows a simplified energy level diagram of this process for Yb:Ho:YAG. The energy transfer process between the upper state of Yb^{3+} and other Lanthanide ions is an extremely efficient process, typically having an efficiency of >90%. This process can also occur with Tm^{3+} and Pr^{3+} impurities, with both of these ions causing emission at 490 nm [75].

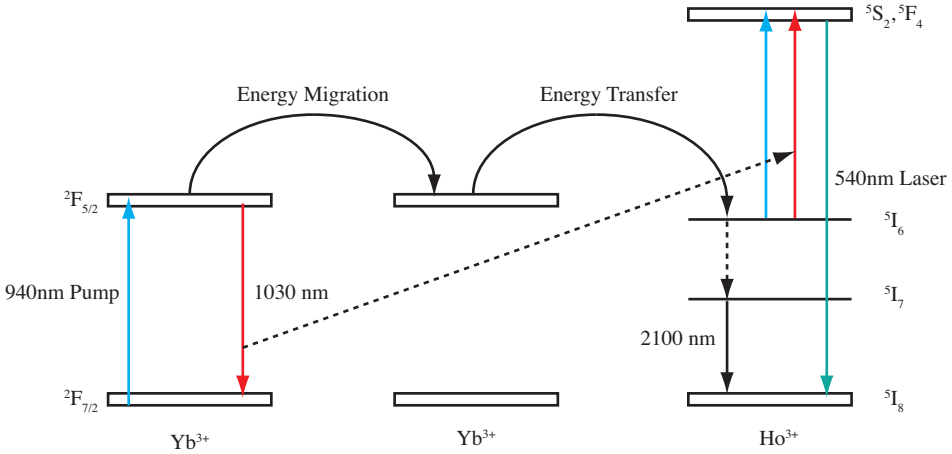

Figure 4.16 – Stepwise upconversion process in Yb:Ho:YAG.

The emission observed from the Yb:YAG planar waveguide laser does not match any of the common impurities in Yb doped materials. The small feature at 485 nm at the side of the main emission can be attributed to Tm^{3+} or Pr^{3+}, whilst the shoulder at 525 nm can be attributed to Er^{3+}. Emission at 500 to 515 nm has been observed previously in other Yb-doped materials such as $YbPO_4$ [80] and $Ca_{1-x}Yb_xF_{2+x}$ crystals [81]. Emission at this wavelength in these crystals has been attributed to cooperative luminescence. Cooperative luminescence occurs when two ions close to each other operate together, creating a virtual upper-state at twice the wavenumber of the usual $^2F_{5/2}$ upper level in Yb. This virtual upper-state then emits light with a wavelength ranging from approximately 500 nm to 514 nm. Figure 4.17 shows a simplified energy level diagram demonstrating the cooperative luminescence process. Cooperative luminescence in Yb:YAG has been observed before by Malinowski *et al.* [82]. They showed cooperative emission from 15%at. doped Yb:YAG in planar waveguide form at 488 to 520 nm, but only at 488 nm from the same crystal in bulk form. Xu *et al.* [83] also show cooperative luminescence in bulk Yb:YAG crystals, however, they only observe luminescence at 488 nm and have determined the optimum concentration for strong Yb-ion pair effects to be 15%at. doped Yb:YAG. At higher doping concen-

trations Yb^{3+} energy migration quenches the cooperative luminescence process. The lifetime of the green transition is also less than the IR emission [80]. This is due to the process using two excited ions, resulting in a reduced upper-state lifetime of the cooperative luminesence process of $\tau_{pair} = \frac{1}{2}\tau$ as shown in figure 4.17.

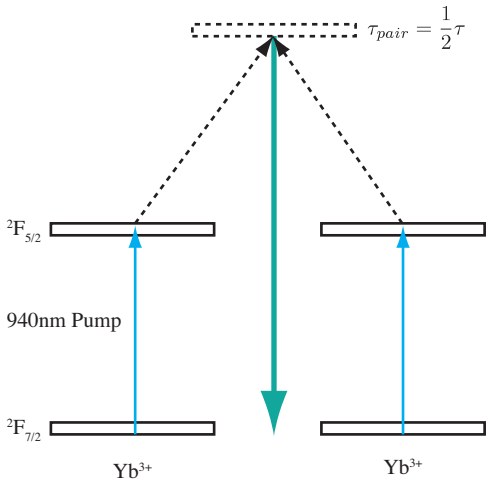

Figure 4.17 – Cooperative luminescence process in an Yb^{3+}-Yb^{3+} pair.

To determine the power emitted in the form of cooperative luminescence, the experiment detailed in figure 4.10 was repeated. The IR filter was replaced with a BG38 filter and a hot mirror so only visible light was able to fall on the power meter. Figure 4.18 shows the power emitted in the visible plotted against diode pump current with double-sided pumping. This shows at maximum diode current, 650 mW of visible fluorescence is emitted from a single laser facet, making up approximately 8% of the total fluorescence collected with no filters. To fully understand cooperative luminescence's affect on gain at 1030 nm, the lifetime of the cooperative luminescence needs to be measured and applied to a full rate equation analysis. However, due to the complexity of the experiment required to measure fluorescence lifetimes and the lack of data on cooperative luminescence in 2%at. doped Yb:YAG crystals, this analysis has not been done.

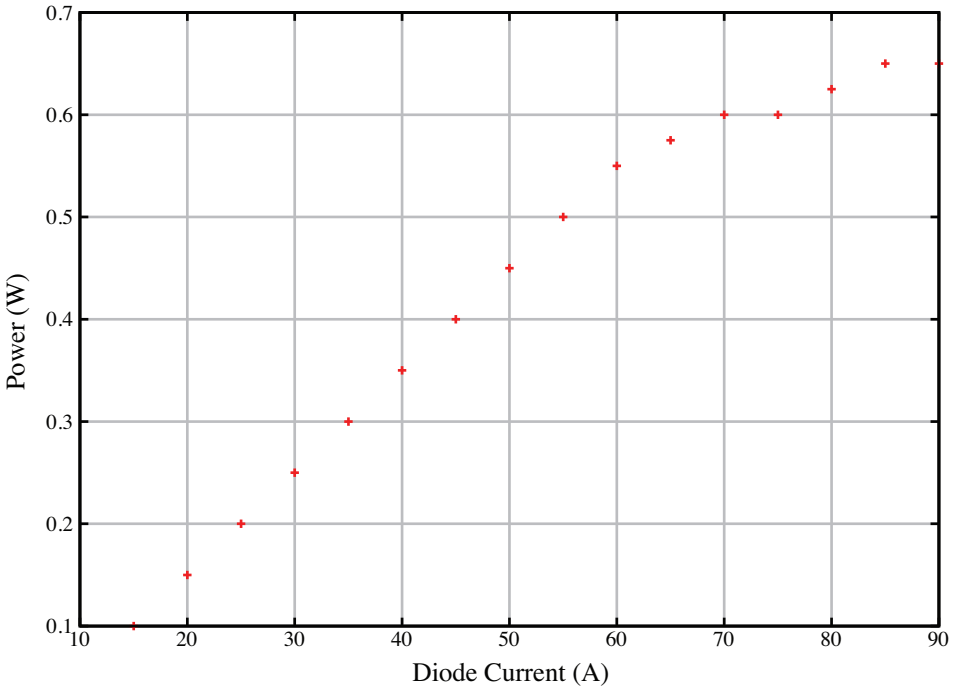

Figure 4.18 – Visible Fluorescence power output from a single waveguide facet.

4.5 Measurement of Gain in the Yb:YAG Planar Waveguide

Within this section, the theoretical gain within the 2%at. doped Yb:YAG waveguide is calculated with varying pump intensity. The gain within the waveguide is then directly measured using a single mode diode laser operating at 1030 nm. The theoretical gain is then compared with the measured gain.

4.5.1 Calculation of small signal gain coefficient

To determine the theoretical gain within the Yb:YAG planar waveguide laser, equation 4.2 must be used which is adapted to give a value for gain, g_0, with varying fraction of total active ion population in the upper state, x [50].

$$g_0(x) = N_0[(\sigma_e \cdot x) - \sigma_a(1-x)] \tag{4.2}$$

Where $N_0 = 2.7 \times 10^{20}$ cm^3 is the dopant density of active ions within the Yb:YAG waveguide. σ_e is the stimulated emission cross section at the laser wavelength and σ_a is the absorption cross section at the laser wavelength, with both values taken from Krupke [41] at 300 K, where both are effective cross sections made up from a combination of different absorption and emission lines overlapping. The data for the absorption cross section spectrum is reliable, however, the emission cross section can have an error up to 20% due to it being very difficult to measure and calculate

using the Fuchtbauer-Ladenberg method. The values for the two cross-sections are $\sigma_{SE} = 1.7 \times 10^{-20}$ cm^2 and $\sigma_a = 0.1 \times 10^{-20}$ cm^2.

Figure 4.19 shows a plot of fraction of total active-ion population in the upper-state versus gain. This shows a gain of 2 cm^{-1} when 45% of the total population is excited, this is the point at which the maximum 85% of the excited population produced can be extracted as shown in figure 4.8 [74].

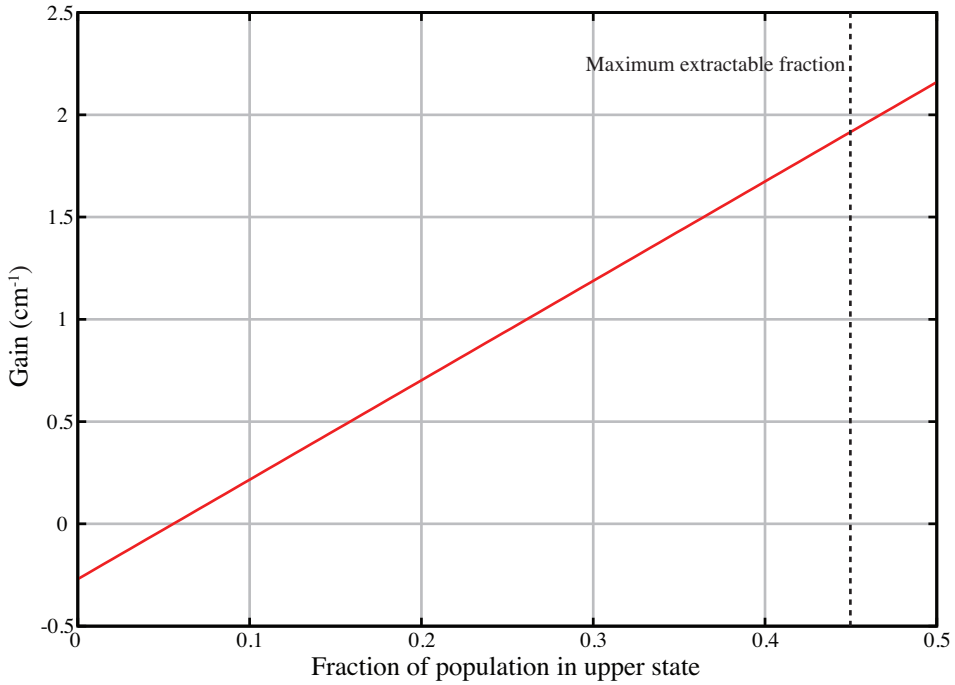

Figure 4.19 – Gain as a function of excited fraction of total active ion population. The maximum extractable fraction of excited ions is achieved when 45% of the total ion population is excited.

4.5.2 Measurement of Small Signal Gain Coefficient

This section describes the technique used to measure the gain present within the Yb:YAG planar waveguide when excited through double-edge pumping. The experimental value is then compared with the theoretical result obtained in the previous section.

A 15 mW, 1030 nm single mode fibre-coupled diode laser is used as a probe beam to measure the gain within the planar waveguide. The emission from the laser was coupled into the Ocean Optics HR4000 spectrometer and the temperature of diode casing was modulated using a thermo-electric cooler until the emission from the diode matched the peak in the fluorescence signal from the Yb:YAG planar waveguide laser under intense pumping as shown in figure 4.20.

To couple the output from the fibre coupled diode into the planar waveguide, a

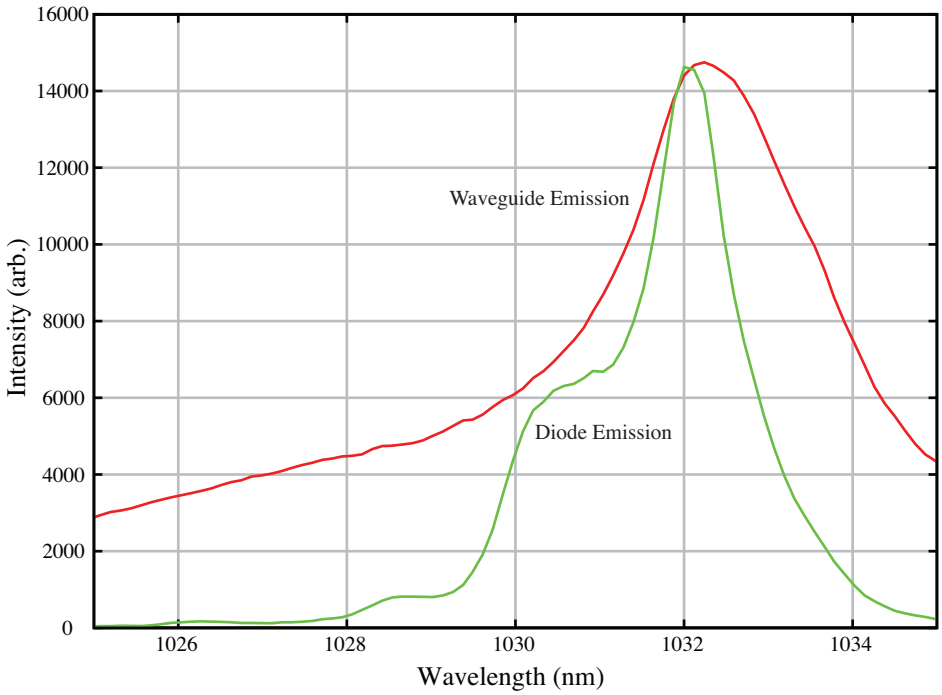

Figure 4.20 – Emission from the 1030 nm diode laser with the fluorescence emission spectrum of the Yb:YAG planar waveguide laser overlaid.

collimating lens was attached to the output end of the fibre pigtail and a 300 mm focal length lens was used to couple the diode light into the waveguide core. A power meter was placed at the opposite side of the waveguide to monitor the transmitted diode light, a slit was also placed after the waveguide for the diode light to propagate through, limiting the level of waveguide fluorescence reaching the power meter and contaminating the measurement. The transmitted diode light was then measured with both pump diode stacks operated from 10 A (below diode threshold) through to 90 A. The experiment was then repeated with the 1030 nm diode laser blocked off to get a background fluorescence reading on the power meter so the data could be compensated. Measurements were then taken in 0.5 mm steps across the full width of the waveguide. The experimental configuration can be seen in figure 4.21. Siegman [31] shows that the small signal gain, g_0, may be calculated from the measured data using equation 4.3.

$$g_0 = \frac{1}{l_{wg}} \ln\left(\frac{P_{out}}{P_{in}}\right) \tag{4.3}$$

The results of the gain measurement experiment can be seen in figures 4.22 and 4.23. Figure 4.22 a), b) and c) show the gain obtained within the Yb:YAG planar waveguide for a) 0.5 mm from the 7° edge, b) the centre of the waveguide and c) 0.5 mm from the 20° edge, all plotted against varying pump diode current. This shows that the gain flattens off at $\sim$1 cm^{-1} due to the onset of pump saturation with double-sided pumping across the whole waveguide. At each edge, saturation also occurs

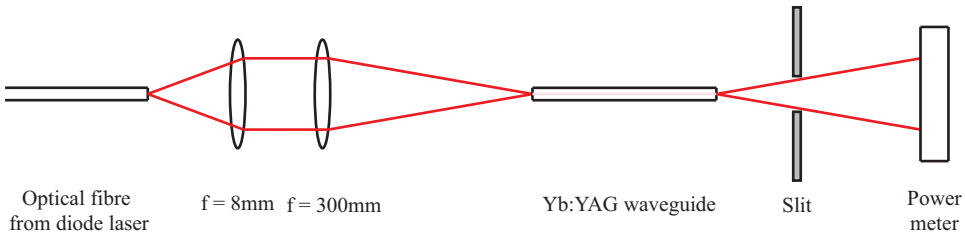

Figure 4.21 – Experimental configuration to measure the gain within the Yb:YAG planar waveguide laser. A fibre-coupled diode laser emitting at 1030 nm is mode matched into the Yb:YAG planar waveguide with the power at the output after the waveguide measured for various waveguide pump intensities.

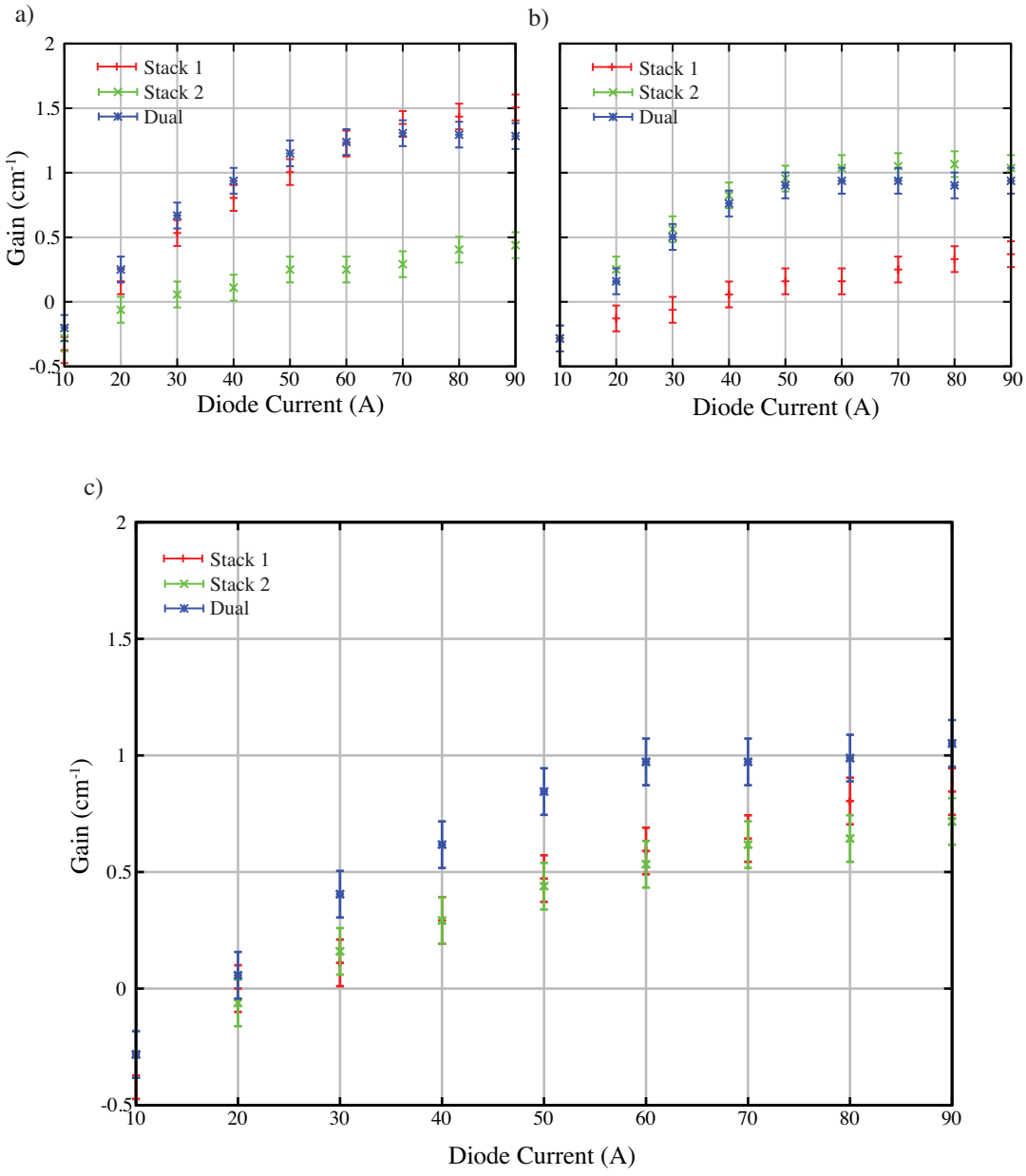

Figure 4.22 – Plots of gain against diode pump current for each diode stack individually and double sided pumping with a) 0.5 mm from the 7° facet, b) the centre and c) 0.5 mm from the 20° facet of the Yb:YAG planar waveguide.

with single-sided pumping when pumped only at the respective edge, this shows the incident intensity from each stack individually is sufficient to induce localised pump saturation. At the centre of the waveguide, each stack produces approximately the same gain when pumped from a single edge and does not cause saturation. Saturation only occurs at the centre of the waveguide under double-sided pumping conditions. Measurements near the 7° edge show a higher gain of 1.5 cm^{-1} compared to 1 cm^{-1} achieved near the 20° edge. This can be attributed to a number of factors, it is possible that a doping gradient is present within the crystal, the heatsinks could not be uniformly cooling the waveguide and most significantly, the angle the diode pump light is launched causes a variation in overlap of the diode laser mode with the pump mode within the core.

Figure 4.23 a), b) and c) show the gain for various pump currents plotted against the width of the waveguide (0 mm is the 7° edge) for a) only stack 1 (pumping 7° facet only), b) only stack 2 (pumping 20° facet only), and c) both diode stacks on. This data shows the gain profile through the waveguide utilising various pumping methods. Single-sided pumping of the 7° facet results in an exponential-like decay in the gain with distance from the pump source, whilst single-sided pumping of the 20° facet has an initial increase after ∼1.5 mm into the waveguide and then follows a near linear decay. This decay is expected to take the shape of Beer's law due to the lateral pump absorption profile rather than the linear profile measured. This difference is due to the non-uniform pump profile in the transverse direction not having perfect overlap with the gain probe beam causing variations in overlap across the lateral width of the waveguide causing the 'ripples' seen in the lateral gain profile. This effect is caused by the angle the pump diodes are set at, the 7° edge is pumped so the diode light propagates near parallel through the waveguide, whereas the 20° facet is pumped at an angle to avoid light falling on the opposite stack, this results in the top and bottom of the waveguide being pumped initially rather than the centre where the gaussian gain probe beam was at its most intense. We modelled the pumping of the planar waveguide by coupling 6 gaussian beams into each facet at the angle set experimentally and observed the pump intensity variation through the guide, including absorption effects [84]. The results of this can be seen in figure 4.24, this shows the 7° edge to have a peak intensity in the centre of the guide, whereas the 20° edge initially has greater intensity at the edges resulting in less overlap with the gain probe beam, confirming the reason for greater gain being measured at the 7° edge than the 20° edge. Under double-sided pumping conditions, the gain profile is reasonably uniform throughout the width of the waveguide with a nominal small signal gain of 1 cm^{-1}.

The measured gain near saturation is less than the calculated gain shown in figure 4.19 at room temperature. However, thermal models of the heatsinks show the waveguide core to increase in temperature near saturation causing the gain at higher

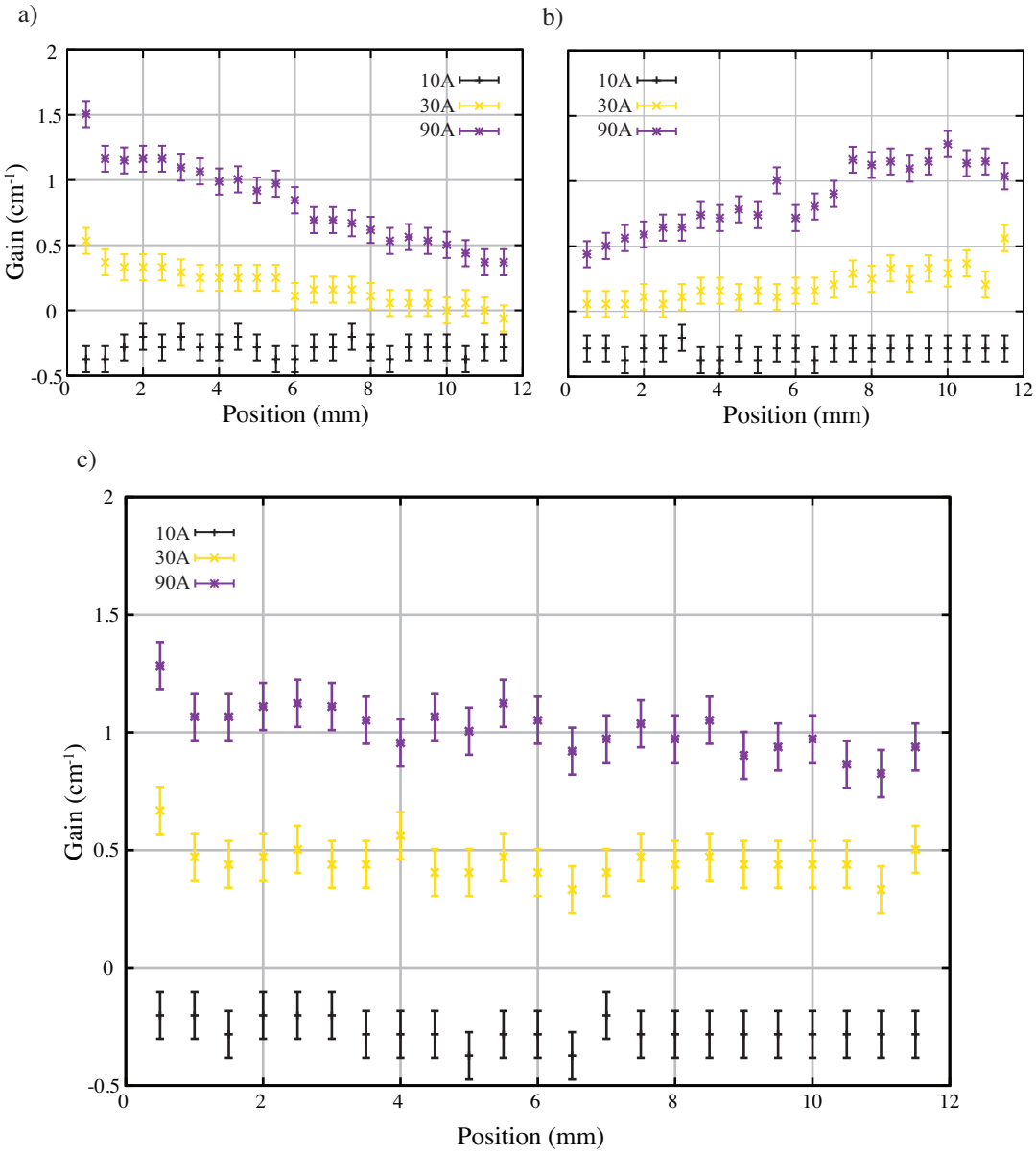

Figure 4.23 – Gain profiles laterally through the Yb:YAG planar waveguide for a) single-sided pumping of the 7° edge, b) single-sided pumping of the 20° edge and c) double-sided pumping. The profile is plotted for various pump diode currents with 10A being below the pump diode threshold.

temperature to be reduced slightly from the value at room temperature due to reduced emission and absorption cross-sections. The variation of gain across the lateral width of the waveguide suggests that pump overlap with the propagating mode is a significant factor, with the greatest gain being in regions where there is the strongest overlap. The most significant contributing factor to the available gain is the onset of pump saturation, effectively limiting the gain to 1 cm^{-1} across the full width of the waveguide. However, even with these limitations, the measured uniform gain of $\sim$1 cm^{-1} is a factor of ten higher than that previously measured in a Nd:YAG planar waveguide laser [28]. Combined with the improved pump uniformity and redesigned heatsinks, operation as a high efficiency, high output power laser is possible.

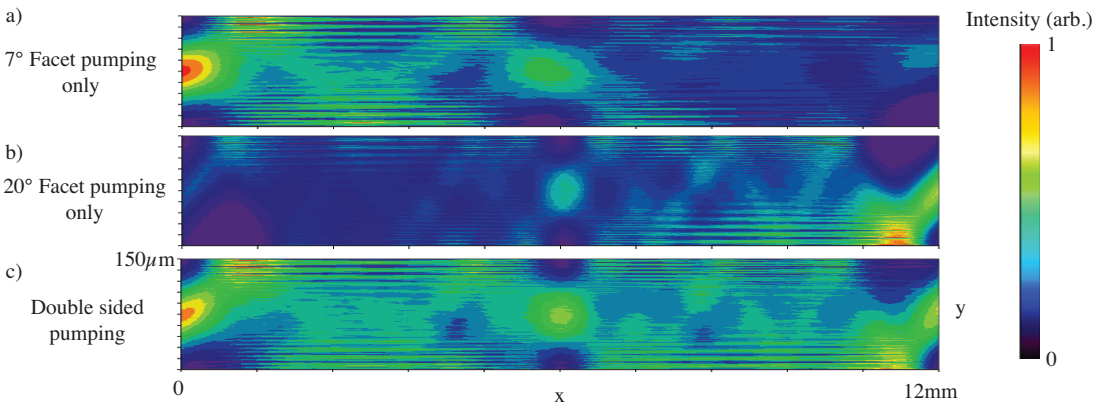

Figure 4.24 – Colour profile representing the relative pump intensity through the Yb:YAG planar waveguide core under various pumping conditions. The x-direction represents the lateral profile through the core, whilst the y-direction represents the transverse profile. The banding is due to the model being the combination of 6 coherent gaussian beams resulting in interference fringes which would not be present in the actual device.

4.6 Conclusions

Within this chapter, designs of new heatsinks were presented for the Yb:YAG planar waveguide. These heatsinks are more compact than the previous design, allowing for mirrors to be placed close to the waveguide facets. The next chapter discusses high-power operation with close-coupled resonator mirrors.

A fluorescence imaging technique has been developed, which enables the pump alignment and uniformity to be monitored remotely. Utilising this technique allowed a second diode stack to be aligned to the planar waveguide giving a maximum of 800 W incident pump power. Monitoring the fluorescence under intense double-sided pumping showed a very uniform lateral pump profile. The output power of the fluorescence also suggests the presence of ASE within the waveguide core, which may limit the total output power available from the laser. The fluorescence imaging also suggests evidence of pump saturation occurring under double-sided pumping due to the high-incident pump intensity. Reaching pump saturation is very useful in amplifier applications as it maximises the energy storage within the waveguide.

Gain measurements were also performed using a 1030 nm 15 mW diode laser. These measurements determined the lateral gain profile, which proved to be uniform under double-sided pumping conditions. The gain measurements also confirmed the effects of pump saturation. Uniform small signal gain of 1 cm^{-1} represents an amplification factor of three to four times per pass. High gain allows for the high-power laser operation, which is discussed in the next chapter. The high amplification factor shown means amplification factors of 1000-fold amplification after six passes of a

signal through the waveguide core. The high-gain and amplification is promising for operation of the device as a compact amplifier for single spatial mode pulsed laser systems.

Chapter 5

Efficient Operation of High-Power Yb:YAG Solid-State Planar Waveguide Lasers

5.1 Introduction

This chapter discusses efficient laser operation of the Yb:YAG planar waveguide laser. Improvements made in chapter 4 to the heatsinks allow resonator optics to be placed close to the waveguide facets, minimising intra-cavity losses. Double sided pumping has shown that a uniform pump and gain distribution giving an amplification of 3-4 times per pass has been achieved in the Yb:YAG planar waveguide. This leads the way to efficient laser operation, uniform pumping removes any absorbing regions laterally through the waveguide, reducing the intra-cavity loss and high-gain under intense pumping enables high laser power output.

Initially, close coupled plano-concave resonators are tested giving excellent results with highly efficient operation. The laser output is highly multimode in the lateral direction whilst maintaining near single mode operation in the transverse direction. The results from these resonators represent a significant increase over the previous power output record from a diode pumped solid-state planar waveguide laser achieved by Xiao *et al.* [14]. Trials with a hybrid unstable resonator are also performed, resulting in lower power but significantly improved lateral beam profile. Initial trials of custom laser machined toroidal resonator mirrors are then performed.

5.2 Modelling Laser Performance with Variable Output Coupling and Losses

This section models the laser performance of the Yb:YAG planar waveguide under double-sided pumping conditions. The model utilised within this section is a slightly modified approach to that presented by MacKenzie *et al.* [29] which itself is a modified version of the model applied by Beach *et al.* [85]. This model was originally developed

Parameter	Symbol	Value
Pump delivery Efficiency	η_{del}	0.99
Pump 940 nm photon energy	$h\nu_p$	$2.1 * 10^{-19}$ J
Laser 1030 nm photon energy	$h\nu_l$	$1.9 * 10^{-19}$ J
Output coupler reflectivity	R	0.8
Pump absorption cross-section	σ_a	$0.1 * 10^{-20}$cm^2
Pump overlap with doped core	η_{po}	0.75
Laser emission cross-section	σ_e	$1.7 * 10^{-20}$ cm^2
Laser overlap with doped region	η_{lo}	1
One-way waveguide transmission	T	Variable
Excited state energy storage lifetime	τ	951 μs
Waveguide length	L_{wg}	13 mm
Waveguide width	W_{wg}	12 mm
Core height	$2a$	150 μm
Yb dopant density	N_0	$2.1*10^{20}$ cm^{-3}
Terminal laser $^2F_{7/2}$ Boltzmann occupation factor	$f_{l,3}$	0.046
Initial laser $^2F_{5/2}$ Boltzmann occupation factor	$f_{u,1}$	0.70
Initial pump $^2F_{7/2}$ Boltzmann occupation factor	$f_{l,1}$	0.88
Terminal pump $^2F_{5/2}$ Boltzmann occupation factor	$f_{u,2}$	0.17

Table 5.1 – Yb:YAG laser parameters used for modelling

to study the performance of an end-pumped Yb:YAG rod laser. Table 5.1 lists the parameters used within the model, with the majority of the constants taken from [41, 85] with Yb:YAG operating at 300 K. The fractional populations $f_{l,1}$, $f_{l,3}$, $f_{u,1}$ and $f_{u,3}$ were calculated previously in chapter 4, section 4.5.

Equation 5.1 gives the output power of the laser as a function of the slope efficiency η_{slope}, the incident pump power P_p and the laser threshold power P_{th}.

$$P_{out} = \eta_{slope} \left(P_p - P_{th} \right) \tag{5.1}$$

The highly multi-mode laser oscillation in the lateral and transverse directions gives relatively uniform gain saturation and can be approximated using a plane-wave. The lateral pump profile under double-sided pumping is approximated to be uniform across the waveguide width. This approximation is slightly incorrect, as the lateral pump profile was shown in the previous chapter to be an approximately the sum of two exponentials, each propagating in opposite directions. Approximating this with a uniform profile will have the effect of a slightly increased laser threshold.

To obtain laser threshold, the populations in the upper and lower laser levels must

be equalised, meaning a minimum inversion fraction of $\frac{f_{l,3}}{f_{l,3}+f_{u,1}}$ must be obtained. This means that for transparency, $f_{u,1}n_2 = f_{l,3}n_1$, where the total dopant density, $N_0 = n_1 + n_2$. However, this assumes that the upper-state population, n_2 is not increased by losses due to output coupler reflectivity, R, and waveguide propagation and coupling losses, T. MacKenzie *et al.* [29] have shown for a double-sided pumped planar waveguide, that the upper state population at threshold incorporating output coupling, resonator and waveguide transmission losses can be expressed using equation 5.2.

$$n_2 = \frac{1}{f_{l,3} + f_{u,1}} \left(\frac{1}{2\eta_{lo}\sigma_e L_{wg}} \ln \left[\frac{1}{T^2 R} \right] - f_{l,3} N_0 \right) \tag{5.2}$$

The incident pump power required for laser oscillation can be expressed using equation 5.3.

$$P_{th} = \frac{h\nu_p}{\eta_{del}\tau} \left(\frac{n_2 2 L_{wg} W_{wg} a}{1 - \exp[\sigma_a N_{2p} \eta_{po}]} \right) \tag{5.3}$$

The exponential function in equation 5.3 compensates for the rate at which pump photons are absorbed out of the pump laser across the width of the laser, where N_{2p} is the integrated upper state inversion density in the pump direction given by equation 5.4.

$$N_{2p} = f_{l,1}(n_2 - N_0) W_{wg} \tag{5.4}$$

Similarly, the slope efficiency, η_{slope}, can be determined using equation 5.5 [29]. Where N_{2l}, the integrated inversion density in the laser direction is expressed using equation 5.6. The $\frac{1-R}{R}$ term represents the power returned to the laser cavity from the output coupler, whilst the exponential terms represent the non-uniform excitation of laser photons within the waveguide.

$$\eta_{slope} = \eta_{del} \frac{\nu_l}{\nu_p} \left(\frac{1-R}{R} \right) \cdot \left(\frac{1 - \exp[\sigma_a N_{2p} \eta_{po}]}{(\exp[\sigma_e N_{2l} \eta_{lo}] - 1)(1 + T^2 \exp[\sigma_l N_{2l} \eta_{lo}])} \right) \tag{5.5}$$

$$N_{2l} = (f_{l,3} + f_{u,1}) n_2 L - f_{l,3} L_{wg} N_0 \tag{5.6}$$

Three efficiencies are also included within these equations, the pump delivery, pump overlap and the laser overlap efficiency, η_{del}, η_{po} and η_{lo} respectively. The delivery efficiency is taken to be 0.99, representing the majority of the pump light coupling into the waveguide. The pump overlap efficiency is 0.75, representing the 75% pump

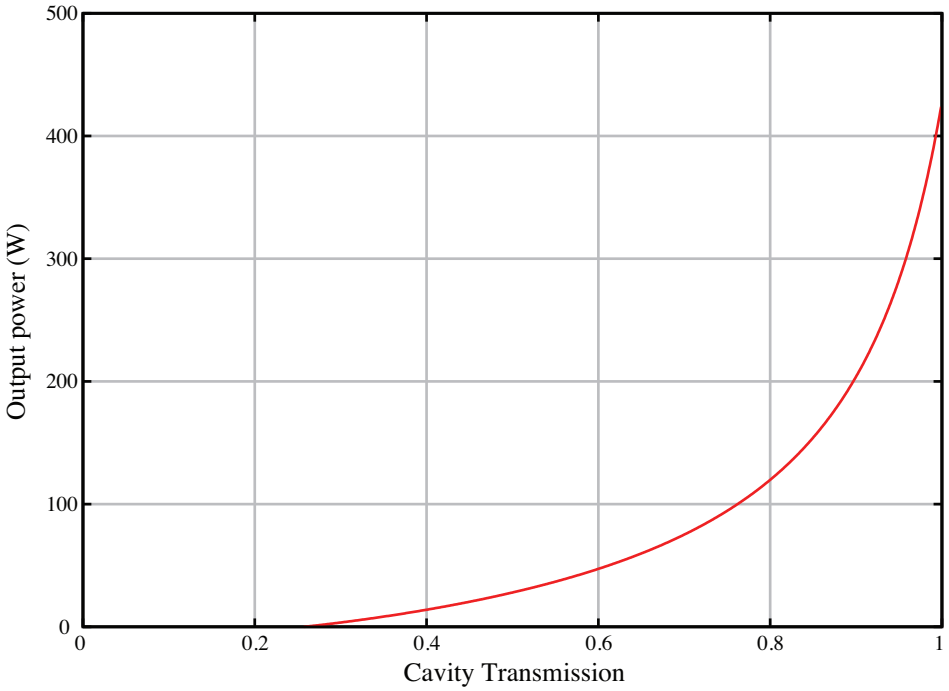

Figure 5.1 – Output power variation with waveguide transmission, T. When $T = 1$, there are no waveguide propagation and coupling losses, as T decreases, introducing loss to the laser resonator, the output power rapidly decreases.

absorption with the laser overlap efficiency being 1, representing the multi-mode laser output extracting all of the available gain.

Figure 5.1 shows how the output laser power depends on waveguide propagation and coupling losses under 800 W of incident pump power, where $T = 1$ represents no losses whilst assuming $R = 0.8$. This shows an extremely rapid decline in output power with increasing loss, showing the importance of a low-loss resonator with excellent waveguide coupling. Figure 5.2 shows a typical Rigrod type curve, allowing the optimal output coupling to be determined with low losses ($T = 0.99$) under 800 W of pumping, showing the optimal output coupling to occur with an output coupler reflectivity of 80%.

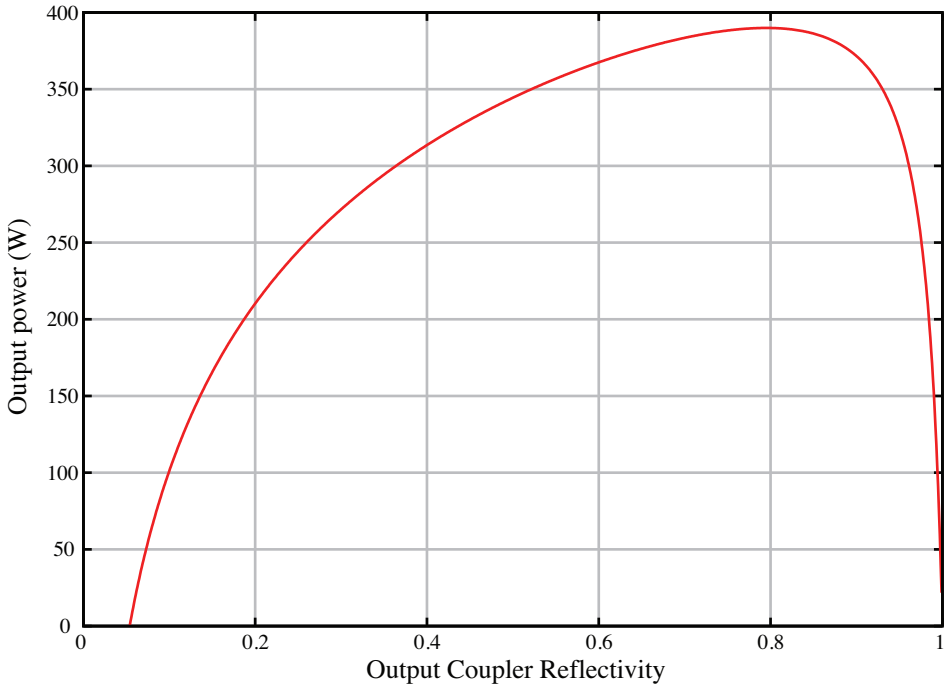

Figure 5.2 – Optimal output coupler reflectivity with low loss and 800 W of incident pump power.

5.3 Plano-Concave Waveguide Resonators

Previous results from this laser, shown in chapter 3, have had low efficiency and high threshold, due to a combination of non-uniform pumping and resonator losses. Non-uniform pumping has been solved by utilising the double sided pumping method described in chapter 4, whilst resonator design has been significantly simplified through the use of smaller heatsinks. Within this section, a resonator utilising closely coupled standard spherical resonator mirrors has been developed to minimise resonator losses.

5.3.1 Resonator Configuration

A simple plano-concave resonator has been developed to combine a weakly confined stable resonator in the lateral direction and a dual case I waveguide resonator in the transverse direction. The resonator consists of a plane output coupler placed 0.5 mm from the front waveguide facet, creating case I waveguide coupling. The rear mirror consists of a 1 m curvature concave mirror, HR coated at 1030 nm placed 0.5 mm from the rear waveguide facet. This creates a dual case I waveguide resonator in the transverse direction and a free-space stable resonator in the lateral direction. A diagram of this resonator can be seen in figure 5.3.

To determine if a stable free-space laser mode can exist within the waveguide in the transverse direction, competing with any waveguide mode, equations 5.7 and 5.8

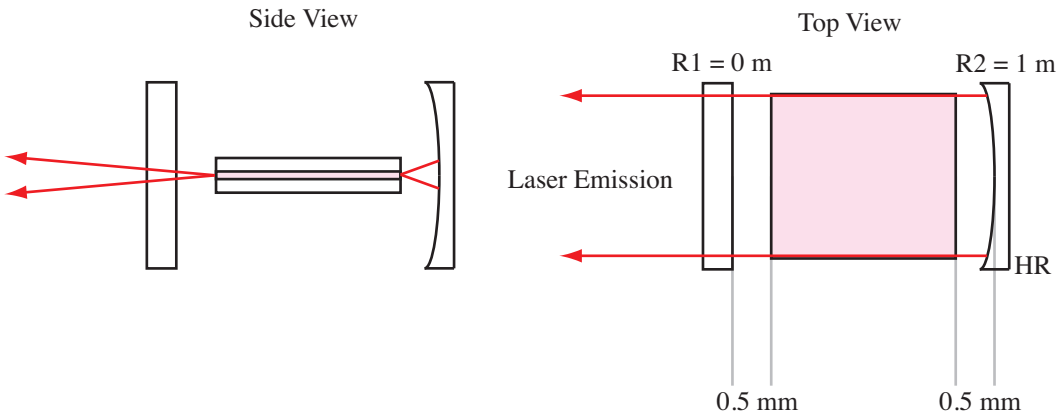

Figure 5.3 – Plano-concave resonator utilising spherical optics creating a hybrid waveguide-stable configuration.

[2] can be use to calculate the size of the free-space mode as a function of position within the cavity.

$$w_0^2 = \left(\frac{\lambda}{\pi} \cdot [L_{wg} \cdot (R_2 - L_{wg})]^{\frac{1}{2}} \right) \tag{5.7}$$

$$w(z) = w_0 \left[1 + \left(\frac{\lambda z}{\pi w_0^2} \right) \right]^{\frac{1}{2}} \tag{5.8}$$

Where w_0 is the beam waist, L is the air equivalent cavity length defined within chapter 2 and R_2 is the curvature of the rear mirror, where $R_2 = 1$ m. This shows the fundamental stable resonator mode does not drop below 170 μm in width and therefore cannot propagate through the waveguide without interaction with the sapphire claddings. Therefore, in the transverse direction, the resonator will operate in the lowest loss configuration of a dual case I waveguide resonator and will have a highly multi-mode beam in the lateral direction, with the number of modes oscillating only limited by the width of the gain region.

5.3.2 High-Efficiency Laser Operation

The resonator described in section 5.3.1 was aligned with a 40% reflectivity output coupler. The waveguide heatsinks were then cooled with water at 20°C. The diode stacks operated with de-ionised water at 27°C. The diode current was then increased, giving the power transfer curve shown in figure 5.4. The experiment was then repeated using 60% and 80% output couplers to allow analysis of cavity losses to be carried out. The laser was only operated to an incident diode power of 400 W for the 40% and 60% output couplers due to the unknown damage threshold of the optical coatings. If the coatings were to burn out, they would likely smoke the waveguide facet, risking serious damage to the device. The 80% reflectivity output coupler does not have this issue

and 385 W was achieved with an incident power of 800 W, representing a 48% optical to optical efficiency. Slope efficiency is difficult to determine as the transmitted, non-absorbed pump light has not been determined. Using the measured single sided pump absorption of 75%, an approximate slope efficiency in terms of absorbed pump power can be calculated. An absorption of 75% yields a slope efficiency of $\sim$ 75%. To the authors knowledge, this represents the highest output power and efficiency achieved to date from a diode-pumped solid-state planar waveguide laser with the slope efficiency comparable to current thin disc laser designs.

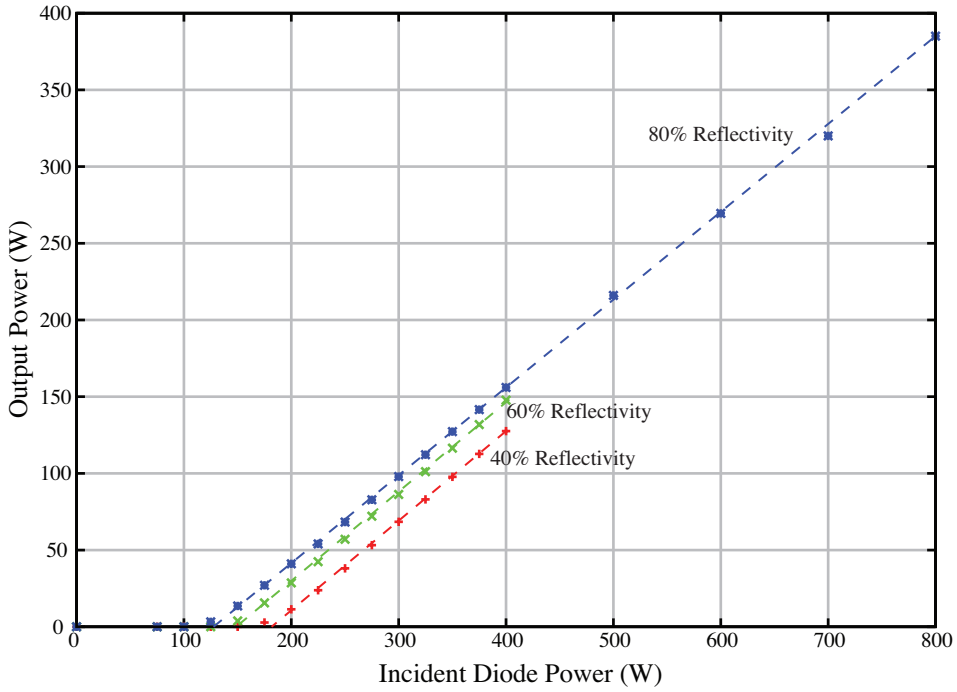

Figure 5.4 – Output power for 3 different output coupling mirrors, with an 80% reflectivity mirror, 385W output is achieved giving a slope efficiency of 75%. The dotted lines represent a fit to the experimental data using the method described in section 5.2.

Figure 5.4 also includes modelled laser output power using the method described in section 5.2. Waveguide transmission and coupling losses, T, were varied along with the upper state lifetime, τ, to achieve a fit to the experimental data. This showed losses due to waveguide propagation and coupling of $\sim$1% and a reduction in the upper state lifetime from 950 μs down to $\sim$900 μs. This reduction can be attributed to the effects of cooperative luminescence and amplified spontaneous emission, with these values remaining relatively constant for varying output coupler reflectivity.

5.3.3 Transverse Mode Selection

The plano-concave resonator in this configuration has good beam quality in the transverse direction, with highly multi-mode operation laterally. Figure 5.5 shows a sample beam profile using the 80% reflectivity output coupler. Low order mode operation in the transverse direction is unusual as the plano-concave resonator creates a dual case I waveguide resonator with no mode control. Using the Huygens kernel arbitrary wave propagation method given by Siegman [31] and described in section 1.4 chapter 1, various order waveguide modes were propagated from the waveguide facet out to the plane at which the beam profile was measured. This was compared with the average transverse mode profile measured using Spiricon as shown in figure 5.6. This shows the output beam to be a combination of modes TE_1 and TE_3 with the average intensity of the TE_3 mode being 20% of the TE_1 mode.

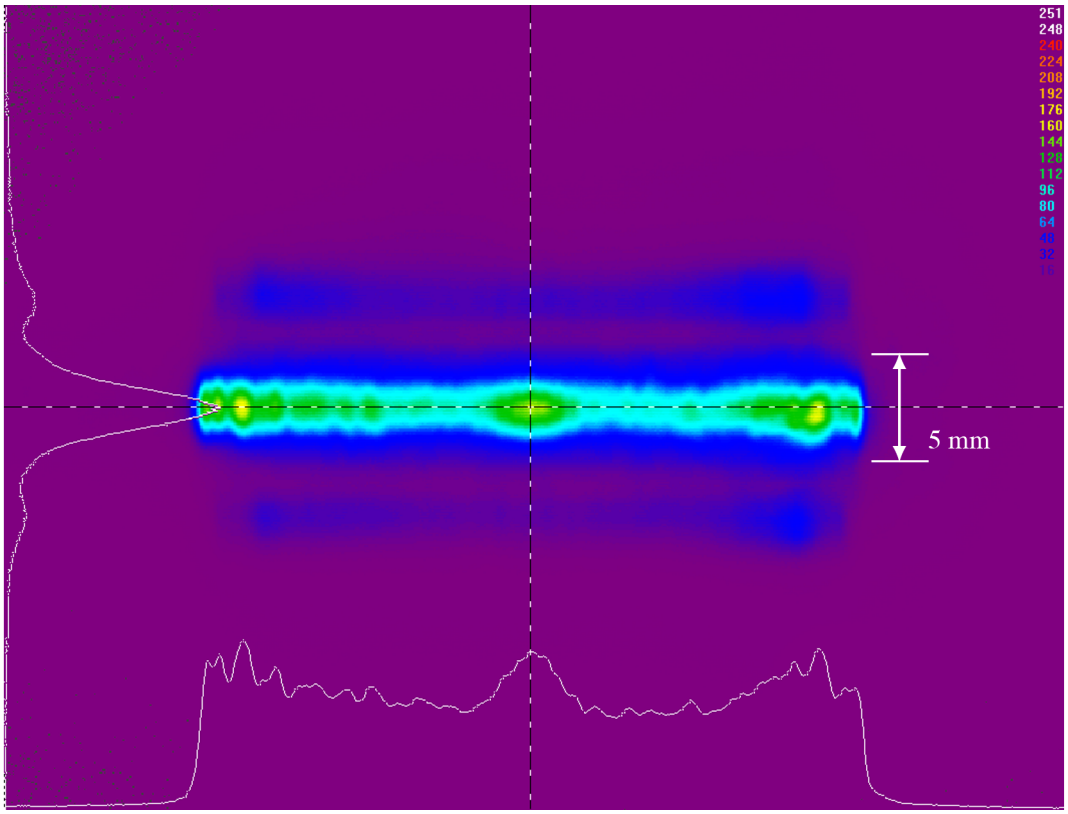

Figure 5.5 – Sample beam profile from the plano-concave resonator with 80% reflectivity output coupler. Measured on a diffusive screen 250 mm from the waveguide facet.

The natural low order mode selection is due to the pump uniformity. The laser prefers low order modes due to the pump being at its most intense in the centre of the waveguide. The effect of pump uniformity can be seen in the strength of modes TE_1 and TE_3 across the width of the waveguide. At the lateral centre, where the sapphire interfaces of the waveguide are pumped the least due to homogenisation of the pump light, as shown in figure 4.24, mode TE_3 has very little power. Near the

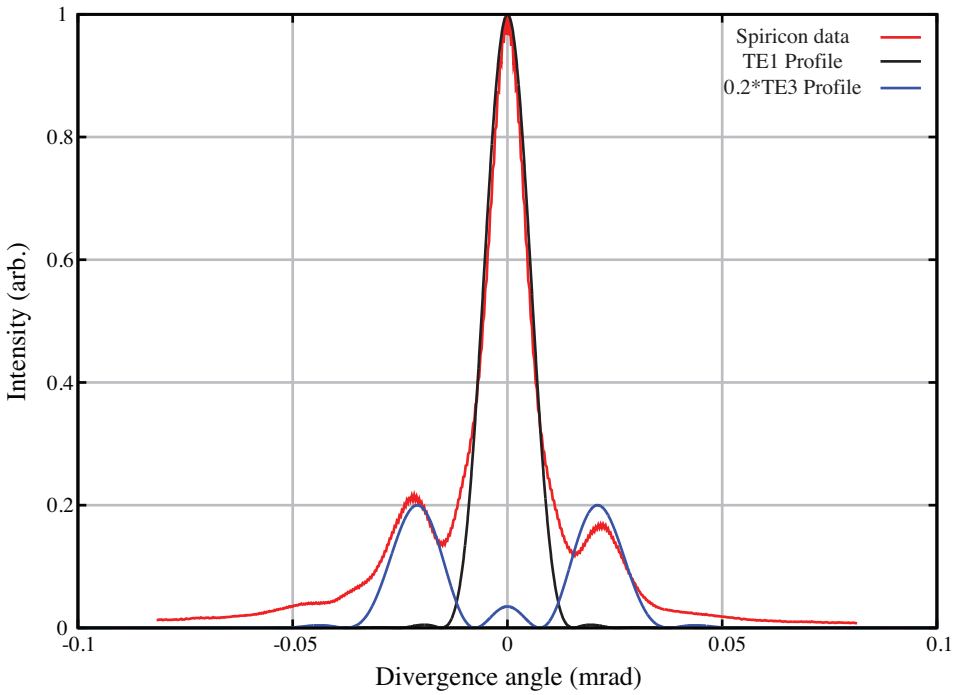

Figure 5.6 – Transverse profile of the output from the plano-concave resonator with plot of the normalised TE_1 and TE_3 modes overlaid.

7° and 20° facet where the pump profile is not homogenised, mode TE_3 has more power although still not as much as the central TE_1 mode. TM modes, $TM_{2,4,6...}$, are suppressed due to symmetry. The lack of a central lobe causes a mismatch between the pump profile which is most intense in the centre of the waveguide corresponding to the pump modelling shown in the previous chapter.

A strategy to improve the transverse beam profile is to translate the HR rear mirror away from the laser facet. Doing this will increase the waveguide coupling loss of higher order modes due to them coupling into the sapphire cladding regions. Higher order modes have a higher divergence than low order modes, hence as the mirror is translated more loss is introduced to the TE_3 mode than the TE_1 mode allowing near single mode operation. Figure 5.7 shows the power output from the laser as the rear mirror is translated away from the waveguide facet, showing a near linear decrease in output power with distance. Figure 5.8 shows the beam profile in the transverse direction with increasing mirror-end facet separation, with near single mode operation achieved at a separation of 1 mm. The profile with a separation of 1 mm still has a small wings at the sides of the main lobe. These can be attributed to weak cladding modes propagating through the waveguide which are excited by the lossy TE_3 mode coupling into the claddings.

Two processes are responsible for the reduction in power with increased separation. Diffractive coupling losses are the first process, this arises from the higher order modes diverging sufficiently to no longer couple efficiently into the waveguide core. The

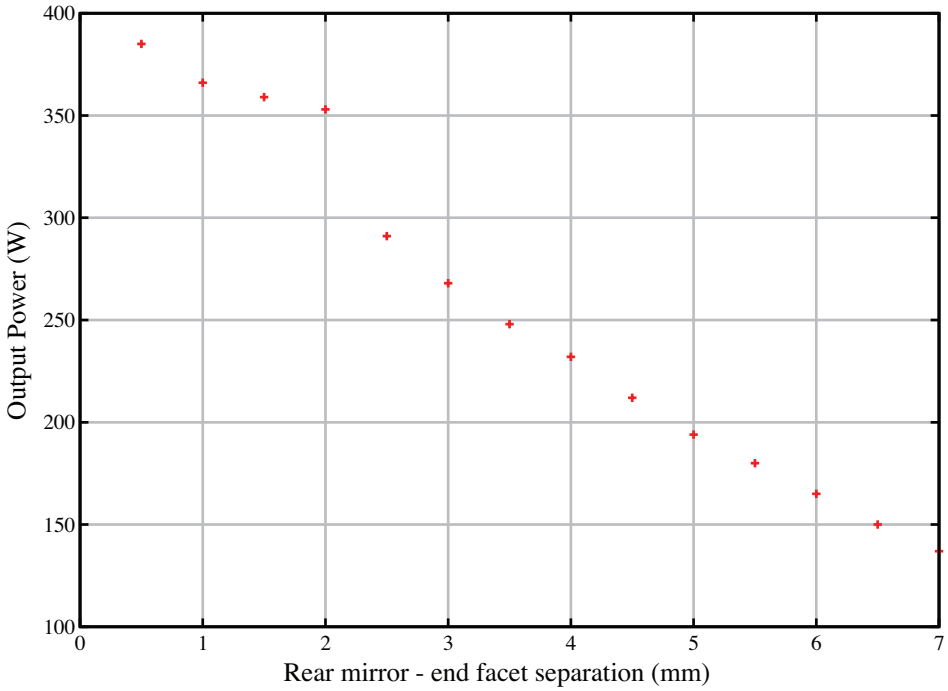

Figure 5.7 – Reduction in output power as the rear mirror to end facet separation is increased.

second process is due to mode mixing where the overlap of the power returned in different waveguide modes interferes. For example, the TE_3 mode can supplement the fundamental mode if the central TE_3 lobe is in phase and overlaps with the TE_1 lobe whilst the two outer TE_3 lobes couple into the sapphire claddings.

An approximation for the diffractive coupling losses can be made theoretically by propagating the different waveguide modes out from the laser facet to the rear mirror, then propagated back into the laser facet. The overlap of the returned mode with the size of the waveguide core region can then be calculated giving an approximation of the diffractive loss for each waveguide mode. Figure 5.9 shows the calculated return profile for modes TE_1 and TE_3 with varying mirror separation with the waveguide core superimposed. The overlap of these profiles with the waveguide core can be seen in figure 5.10, showing losses for the fundamental mode, TE_1 dropping slowly with separation, whereas the TE_3 mode drops rapidly with separation as the side lobes begin to couple into the claddings. By calculating these profiles, an overlap integral can be performed on the fundamental waveguide mode and the returned mode, giving the coupling loss including phase information. Any light coupling through the cladding regions is removed from the calculations by only performing the overlap integral over the waveguide core region. Figure 5.11 shows the results of these calculations for the TE_3 mode propagated out to and returned from the rear resonator mirror and the subsequent coupling efficiency into the TE_1, TE_3 and TE_5 waveguide modes. This shows a significant drop in the coupling efficiency of the TE_3 mode back into a TE_3

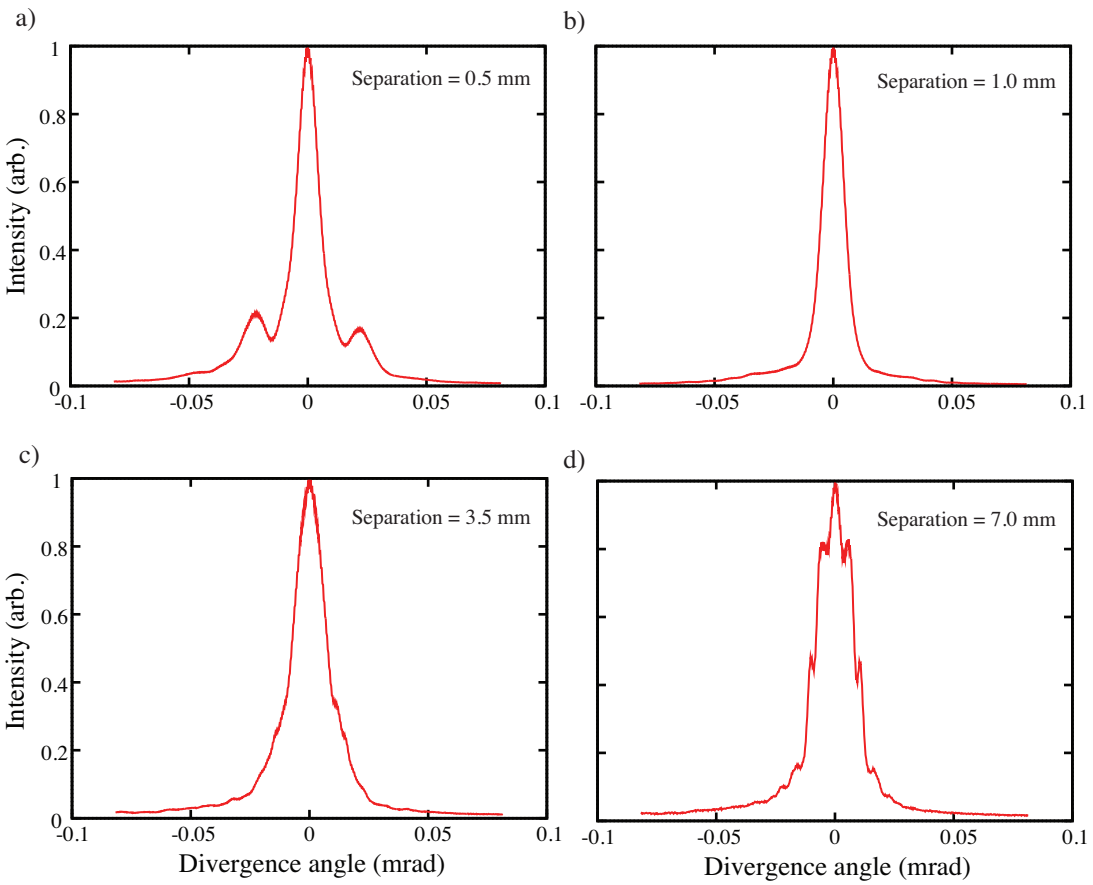

Figure 5.8 – Average transverse mode profile for various mirror-end facet separations. Maximum output power occurs when the separation is minimised (a), Single mode operation occurs at 1 mm (b), as the separation is increased gradually the fundamental mode is diffracted causing broadening (c) and eventually clear diffraction fringes are observed (d).

mode with increasing mirror-facet separation but an increase in efficiency for a TE_3 mode back into a TE_1 mode. The coupling efficiency of the TE_1 mode has also been performed, this shows a gradual decrease in efficiency down to 75% with a separation of 7 mm.

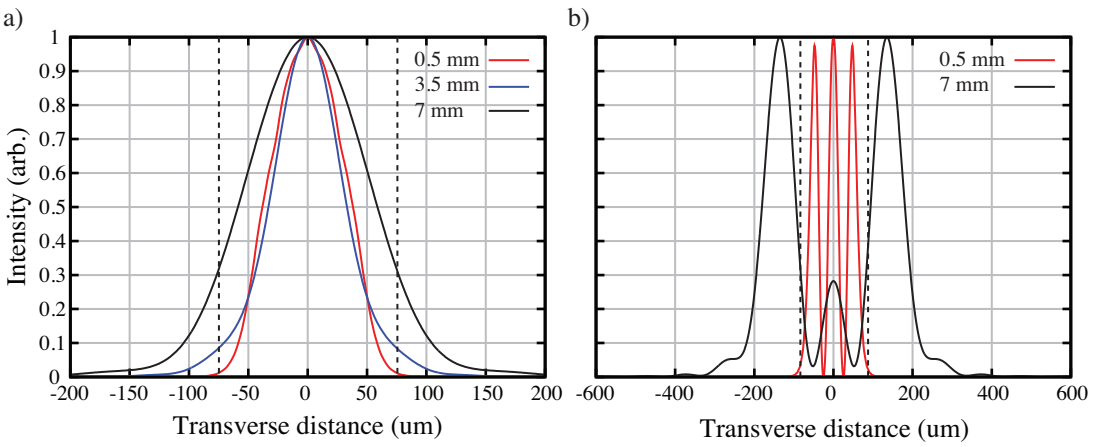

Figure 5.9 – Normalised intensity profiles of the return mode to the laser facet with various mirror-facet separations for a) TE_1 and b) TE_3. The dashed lines represent the waveguide core thickness.

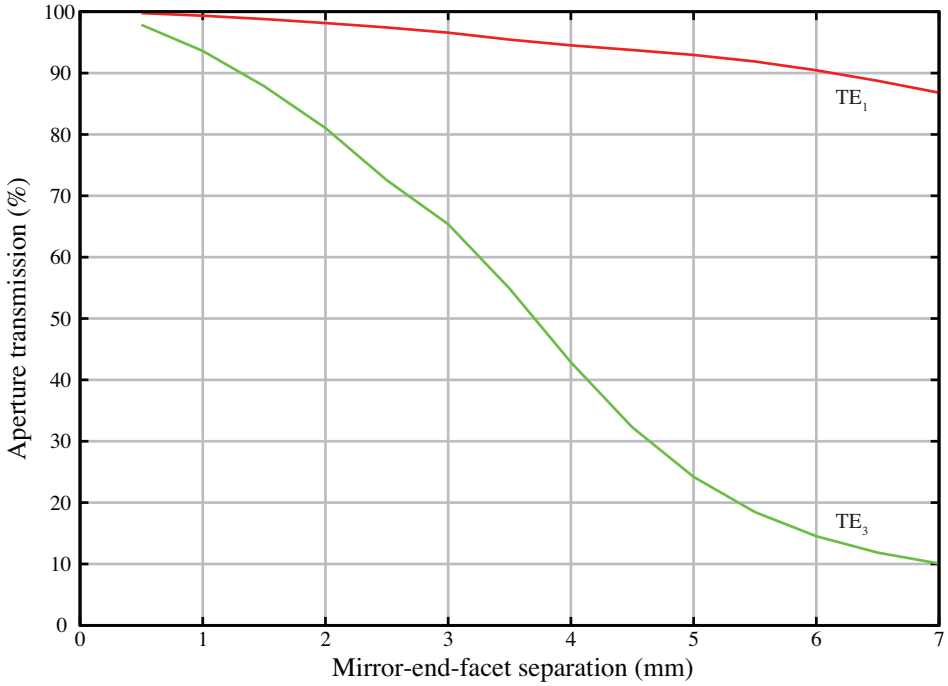

Figure 5.10 – Fraction of the TE_1 and TE_3 mode transmitted back into the core of the waveguide with various rear mirror to waveguide facet separations

Assuming uniform gain throughout the height of the waveguide core, the fundamental waveguide mode sweeps out 75% of the gain available, with a coupling efficiency of 75% back into the core after a mirror 7 mm from the facet, giving ∼55% of the available gain extracted as useful output power. This is a reasonable approximation to the experimental value in which 150 W of the maximum 385 W is extracted with a separation of 7 mm giving a ∼ 40% efficiency. The reduced efficiency experimentally is due to the pump light not being uniformly distributed in the transverse direction.

Using a plano-concave resonator, high power and efficient operation has been

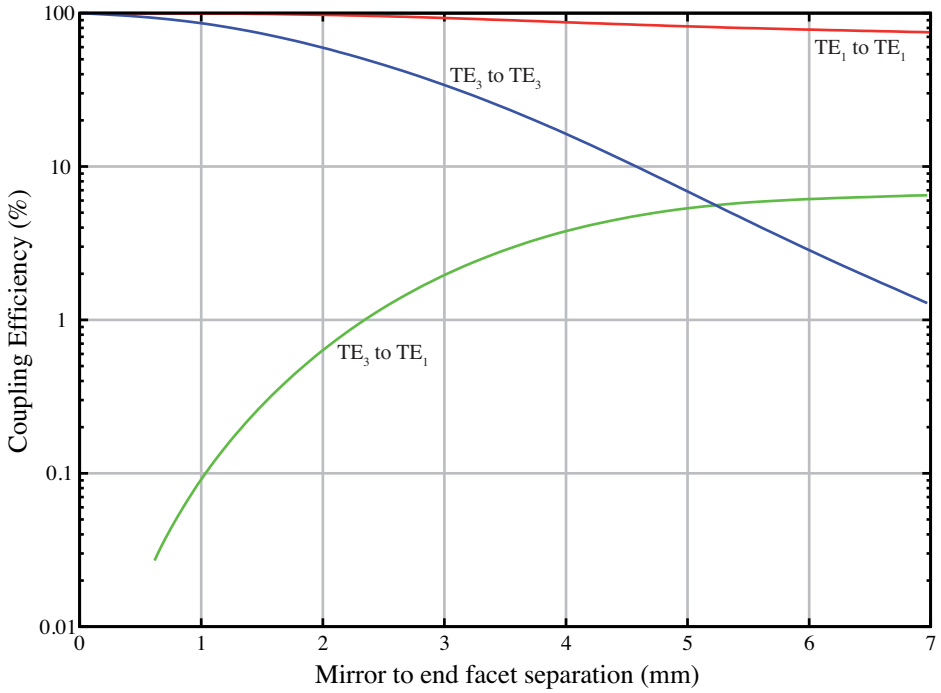

Figure 5.11 – Coupling efficiency of the TE_1 and TE_3 modes back into other modes after propagation from the laser facet, through free-space to the rear mirror then back into the laser facet.

achieved with good beam quality in the transverse direction, however, very poor beam quality is observed in the lateral direction. To improve the lateral beam quality, the next section discusses operation of the laser using a negative-branch hybrid unstable resonator.

5.4 Hybrid Negative Branch Unstable Resonator

Utilising close-coupled spherical resonator optics and double sided pumping, the intra-cavity losses have been reduced sufficiently to allow high power operation. To improve the lateral beam profile, the hybrid unstable resonator previously used in chapter 2 for Nd:YAG planar waveguides has been adapted for use with the shorter Yb:YAG waveguide, without the need for the intra-cavity lens which was used in chapter 3. Figure 5.12 shows a diagram of the resonator used. The resonator formed in the transverse gives case I waveguide coupling from the rear mirror, and concentric, case II waveguide coupling from the output coupler. In the lateral direction, a negative-branch unstable resonator is formed with a magnification of 1.1, giving an effective output coupling of 10%. This creates an under-coupled resonator, due to the optimum output coupling being shown to be ∼20%. The reason for using an under-coupled resonator is due to mirror availability. The mirrors used here were the only mirrors available with a coating which can handle high incident power.

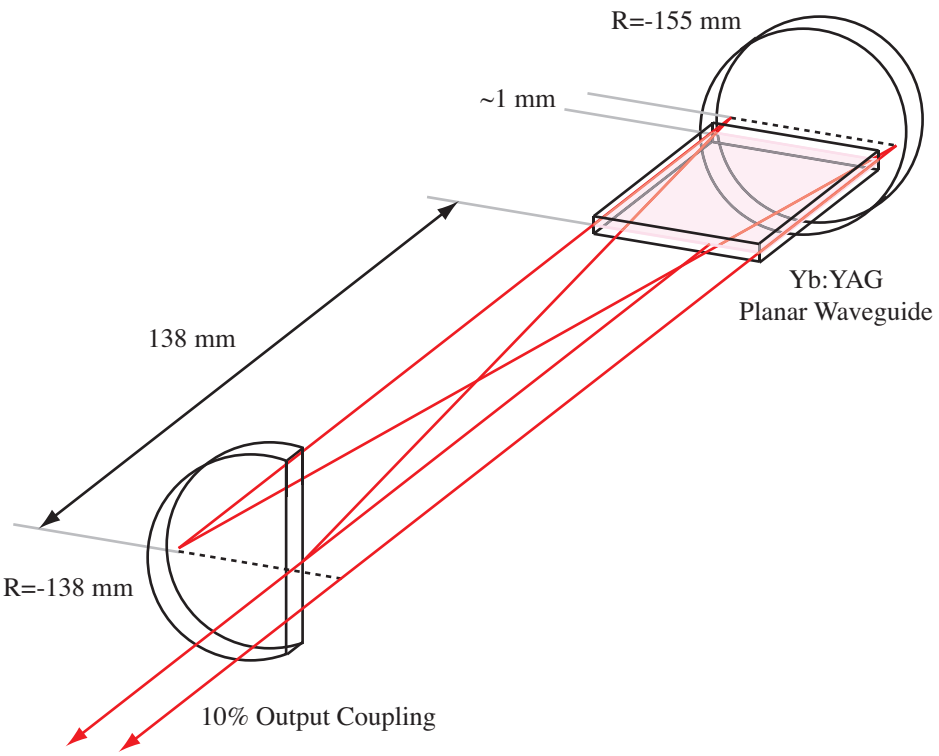

Figure 5.12 – Hybrid negative-branch unstable resonator using spherical mirrors. Case II waveguide coupling is achieved with the output coupler with case I coupling at the rear mirror.

Aligning the resonator to the Yb:YAG planar waveguide gave the power transfer curve shown in figure 5.13. 300 W output was achieved with 800 W incident diode power representing a 37.5% optical to optical efficiency, a laser threshold of 100 W with ∼75% pump absorption gives a slope efficiency of 60%. The beam quality in the lateral direction is much improved as shown in figure 5.14, however, in the transverse direction, the beam quality has deteriorated from that seen in the plano-concave resonator. Fitting the fundamental mode to the beam profile shows the output beam to be an envelope of fringes close to the divergence of the fundamental mode as shown in figure 5.14. The output coupling mirror was translated along the z-axis in an attempt to increase the power output and reduce the transverse coupling problem, the results of this can be seen in figure 5.14. As the output coupler is translated away from the nominal case II distance of 138 mm, the power drops a to half its peak value with a mirror translation of ±3 mm and the fringe envelope does not change significantly until a translation of more than ±2 mm. This shows the fringe envelope is not due to a mirror spacing issue. The fringe separation implies interference from coherent sources with a separation of 250 μm, suggesting that the interference is coming from the sapphire cladding layers. A possible explanation for this is the gradual coupling of radiation into the sapphire claddings during the unstable resonator beam 'walk out', creating coherent interference between the core and cladding modes. This effect has not been seen in the previous work performed on Nd:YAG planar waveguides, due to

the Nd:YAG waveguides being almost six times the length of the Yb:YAG waveguide. Any cladding modes in the longer waveguide will have diverged more and scattered into the 'dirty' YAG-water interfaces, meaning their effect on the waveguide mode is significantly less. This effect could be prevented by the use of an intra-cavity slit, carefully aligned to prevent and light being coupled into the sapphire claddings at each laser facet. An alternative to the slit is the use of case III waveguide coupling at one of the mirrors, its natural mode selectivity will suppress higher order modes, limiting the amount of intra-cavity light coupled into the claddings.

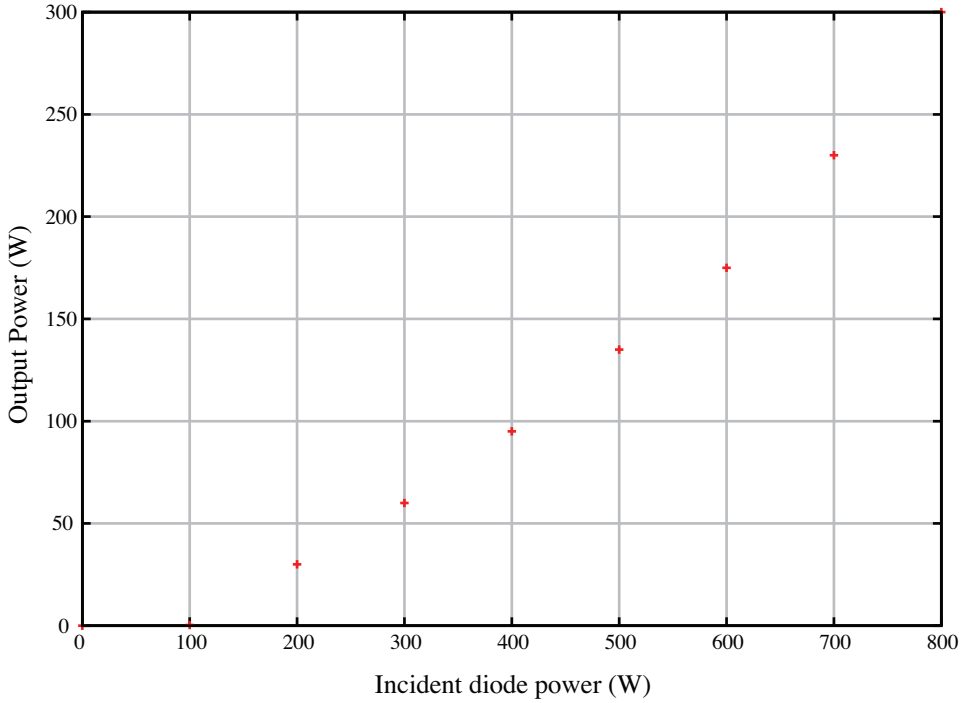

Figure 5.13 – Power transfer curve from the Yb:YAG planar waveguide laser using a spherical mirror hybrid unstable resonator.

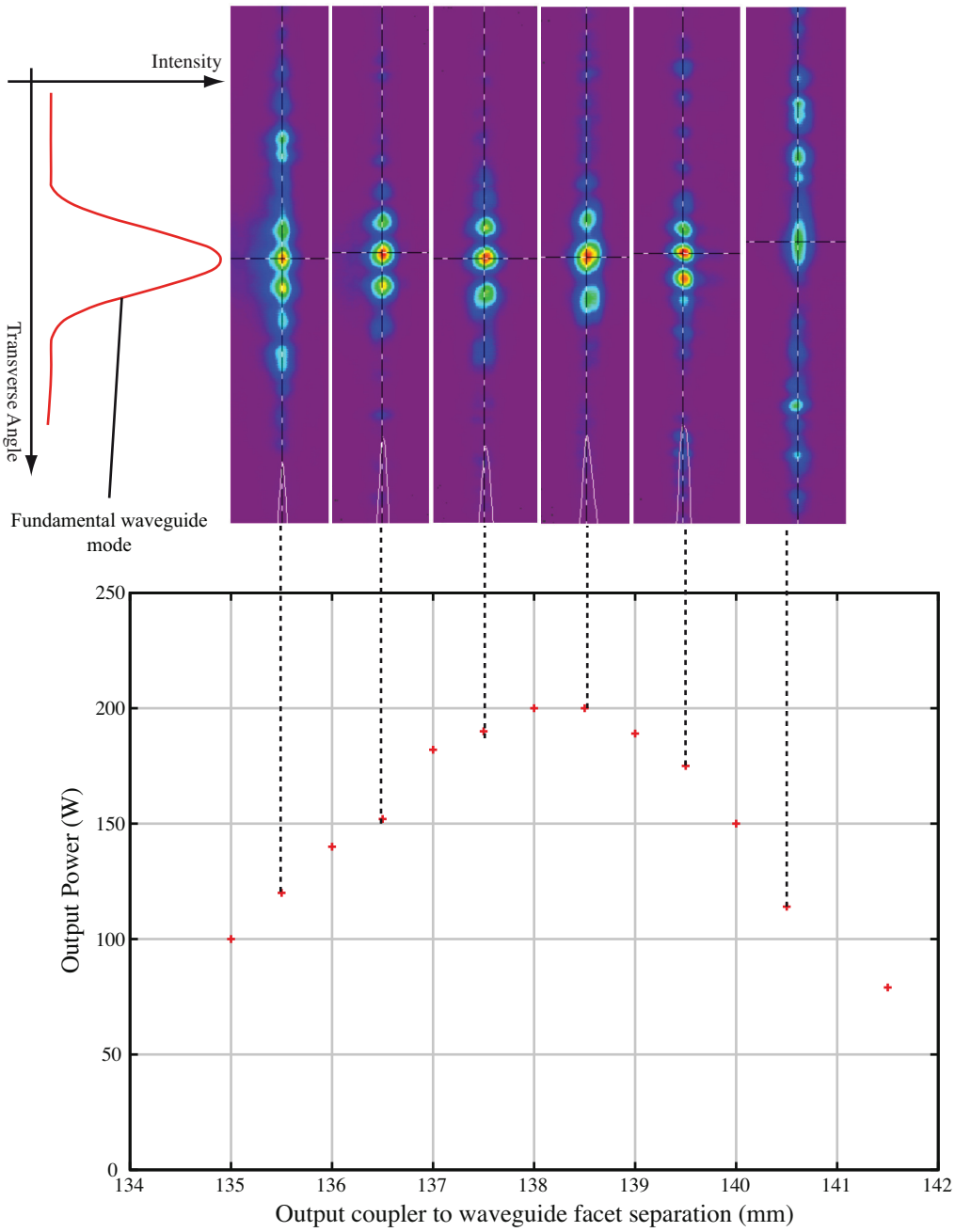

Figure 5.14 – Change in output power and beam profile with varying output coupler to waveguide facet separation. The near-Gaussian profile represents the size a fundamental waveguide mode would be after propagation through free-space to the plane at which the beam profiles where taken.

5.5 Case III Waveguide Resonators

This section investigates the case III waveguide coupling condition utilising a hybrid stable waveguide resonator. The case III condition efficiently couples only the fundamental waveguide mode back into the waveguide facet, suppressing higher order modes and improving the output beam quality in the transverse direction. A highly curved cylindrical mirror is used in place of the spherical rear mirror used for the plano-concave resonator discussed in section 5.3 to assess the coupling losses and beam quality associated with the case III condition.

5.5.1 Case III Condition

The case III condition is discussed in detail in chapter 1. The mirror placement and curvature is defined by equations 5.9 and 5.10 respectively.

$$Z_0 = Z_r \tag{5.9}$$

$$R = 2Z_r \tag{5.10}$$

$$Z_r = \frac{\pi a^2}{2\lambda} \tag{5.11}$$

Where Z_0 is the distance the mirror needs to be placed from the laser facet, Z_r is the Rayleigh range, defined by equation 5.11, R is the mirror curvature, a is the half-height of the waveguide and λ is the laser wavelength. For a 150 μm Yb:YAG planar waveguide, this results in a Rayleigh range of 8.6 mm, meaning the optimum case III mirror must have curvature 17.2 mm and a mirror-facet separation of 8.6 mm.

Due to the short length of the planar waveguide and short curvature of the case III condition, it is possible for a stable free-space resonator mode to exist in the transverse direction. Equations 5.7 and 5.8 allow the range of mirror curvature which form a stable resonator to be calculated. The calculations are performed on a plano-concave cavity with the front mirror placed 0.5 mm from the waveguide facet for maximum output power and the rear mirror placed 8.6 mm from the rear waveguide facet. Figure 5.15 shows the beam size at each waveguide facet for varying rear mirror curvature. This shows a minimum curvature of 15.7 mm is required to form a stable, free-space cavity with a stable mode capable of fitting within the waveguide up to a curvature of 16.5 mm.

5.5.2 Cylindrical Mirror

To test the case III waveguide condition, a cylindrical mirror with a concave curvature of 15.5 mm was combined with a plane, 80% reflectivity output coupler to form a stable

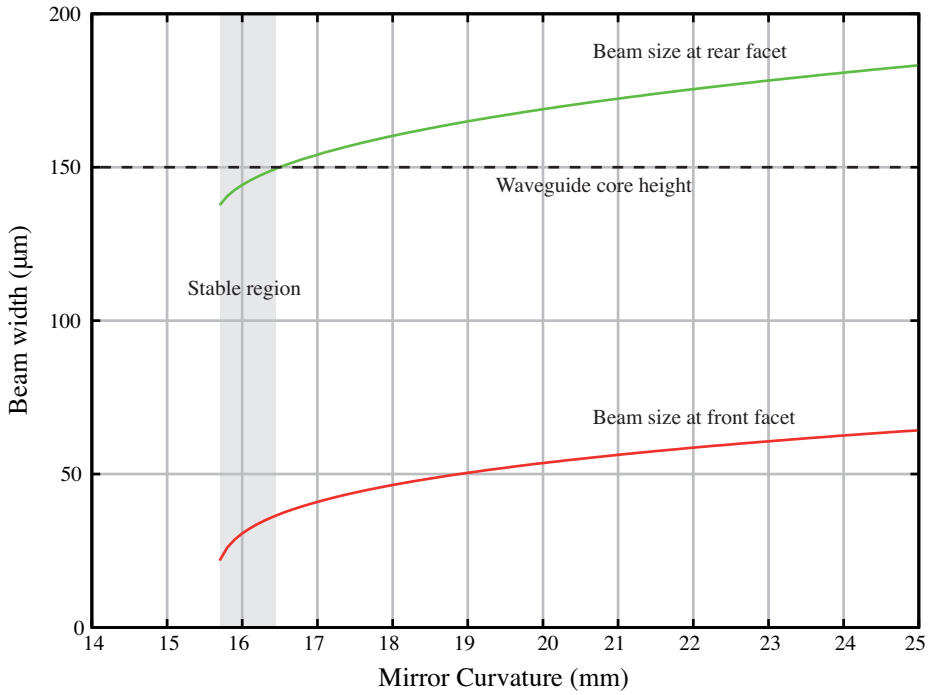

Figure 5.15 – Free-space resonator beam size at each waveguide facet with varying mirror curvature. The shaded region represents the region which a stable free-space mode can fit within the core of the waveguide.

plane-plane resonator in the lateral direction and case I - case III waveguide coupling in the transverse direction as shown in figure 5.16. The plane output coupler was positioned for maximum power output at a distance of 0.5 mm from the waveguide facet with the rear cylindrical mirror placed 8.5 ±0.1 mm from the rear waveguide facet. Figure 5.17 shows stable free-space resonator beam size calculations for a 15.5 mm curvature mirror with varying mirror to end-facet separation. A mirror to end-facet separation of less than 7.85 mm allows a stable free-space resonator to form within the waveguide, which could affect the results obtained within this section.

Due to the low damage threshold of the HR coating on the cylindrical lens, the laser was only operated with an incident diode power of 250 W, varying the mirror to waveguide facet separation gave the output power as shown in figure 5.18. The transverse beam profile with varying mirror-facet separation can be seen in figure 5.19 giving single mode operation and allowing a reasonably large error in mirror-facet separation for single mode operation without introducing significant loss of ±2 mm. The beam profile remains constant with mirror-facet separation varying, showing the output beam is a TE_1 waveguide mode, and not a stable free-space resonator mode. This is due to the waveguide mode being larger than the free-space mode, thus utilising more gain causing it to suppress free-space laser operation.

A maximum power of 68 W was achieved with a mirror-facet separation of 7.5 mm, representing a 3% drop in power from the plano-concave resonator demonstrated in

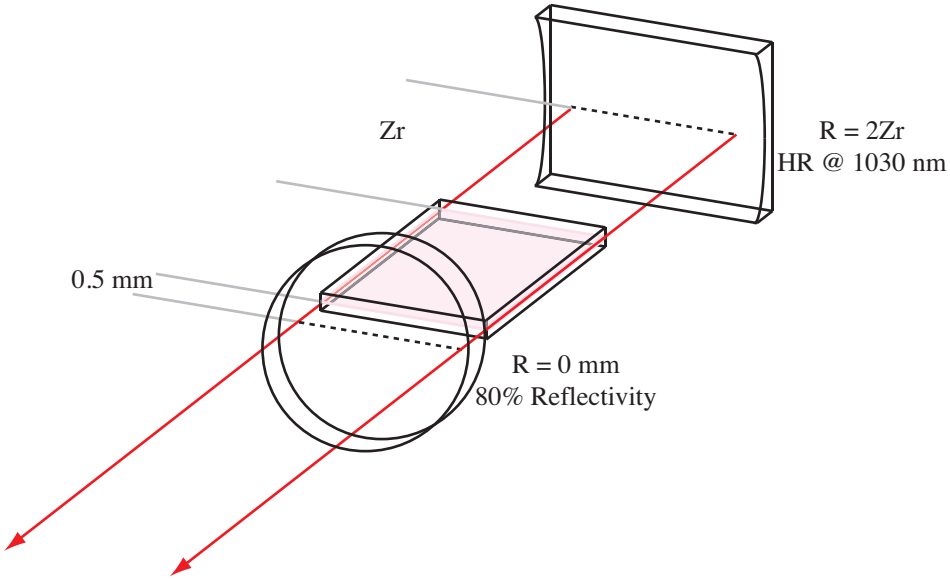

Figure 5.16 – Resonator giving case III waveguide coupling at the rear mirror, case I coupling at the output coupler and forming a plane-plane resonator in the lateral direction.

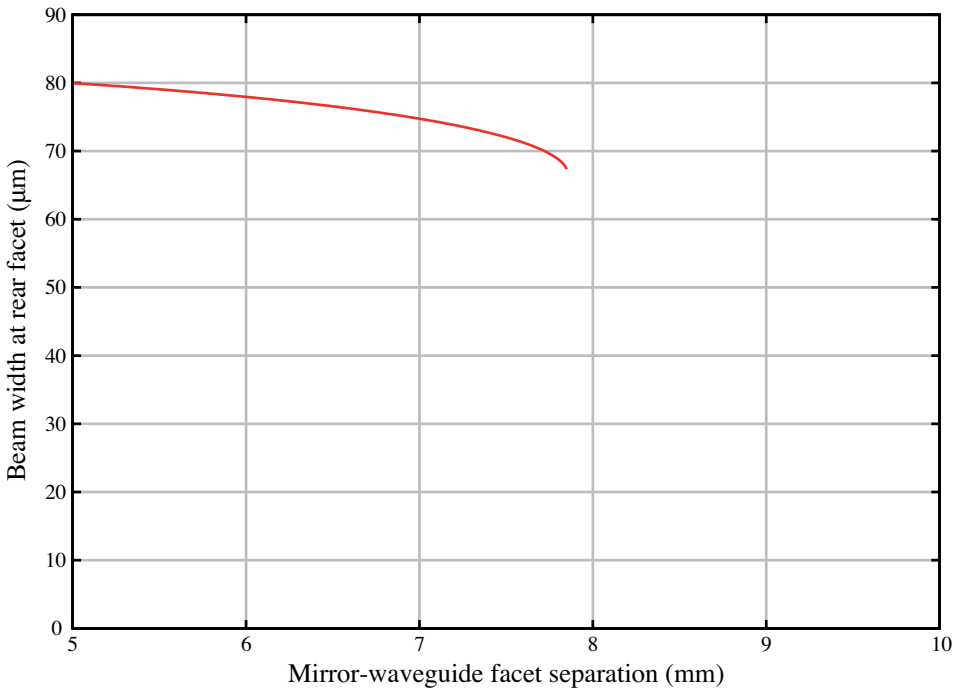

Figure 5.17 – Free-space resonator beam size at the rear waveguide facet. The stable mode can fit within the waveguide when the mirror to facet separation is less than 7.85mm.

section 5.3. The drop in power is due to a number of processes. The lateral direction no longer has any confinement causing any emission not propagating parallel to the optical axis capable of walking out of the resonator laterally introducing loss. The rotation of the cylindrical mirror about the optical axis can cause some alignment loss, however, this was considerably easier to align than the previously shown case II cylindrical resonator mirrors. The losses could be reduced by improving the lateral confinement through the use of a toroidal mirror.

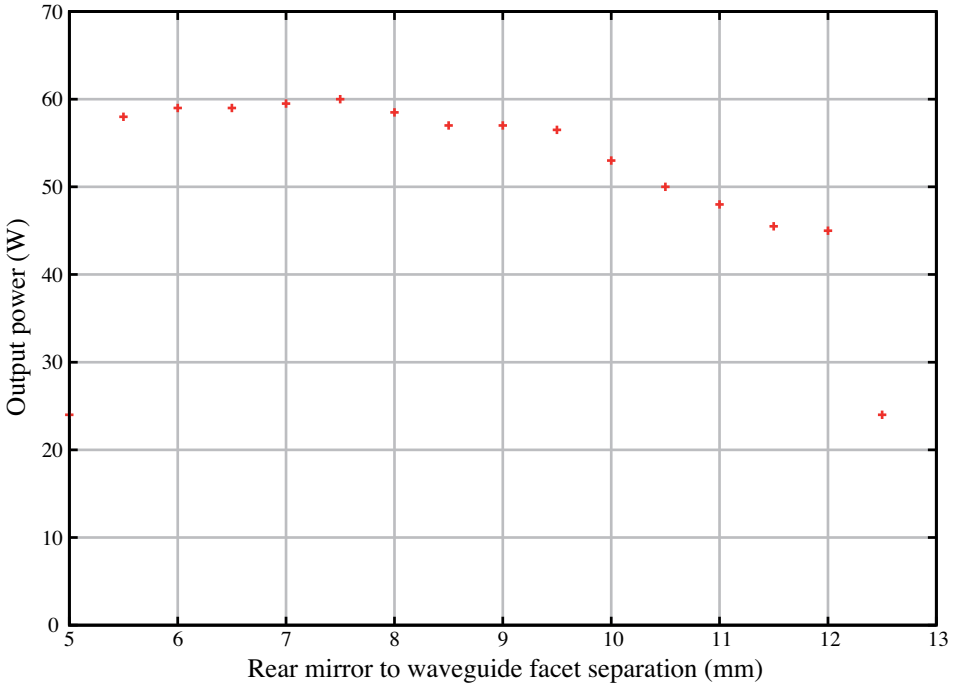

Figure 5.18 – Laser output power with varying rear mirror to waveguide facet separation.

The results in this section show that the case III position provides excellent transverse mode selectivity and nearly matches the output power achieved with a multimode, dual case I cavity. The case III mirror position has also been shown to be tolerant to errors in mirror curvature and placement. The mirror utilised in this section has a curvature 2 mm smaller than the optimal calculated curvature and provided a near constant output power and beam profile over 4 mm of longitudinal mirror translation.

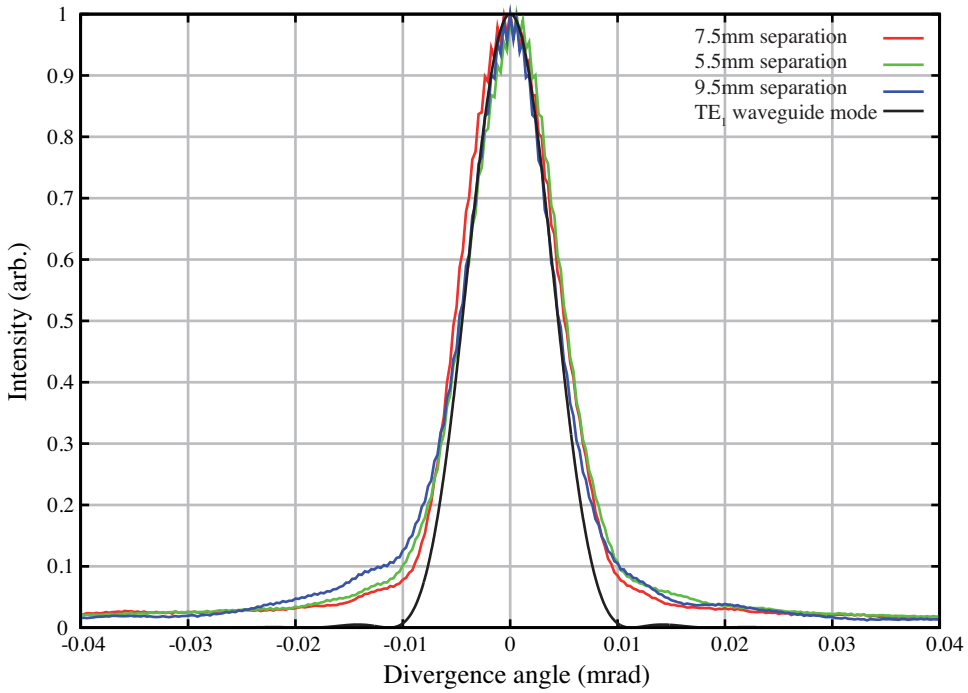

Figure 5.19 – Normalised transverse beam profiles for the case iii cylindrical resonator with varying mirror to end facet separation with the TE_1 waveguide mode plotted for comparison.

5.6 Custom Laser Cut Mirrors

This section discusses the fabrication of toroidal resonator mirrors to improve the lateral confinement, whilst maintaining case III waveguide coupling in the transverse direction. The large transverse-lateral aspect ratio of the planar waveguide creates the need for a resonator mirror that can be highly curved in the transverse direction for efficient case III waveguide coupling, but has a curvature ~10 times less in the lateral direction to form an unstable resonator, sweeping out most of the gain whilst maintaining good beam quality.

Traditional polishing methods can be used to create custom toroidal mirrors, however, the process takes a lot of time and is very costly. This section discusses the use of custom shaped CO_2 laser cut micro-optics as resonator mirrors, created by a laser ablation and laser polishing technique developed within the LPA group. The mirrors fabricated using laser ablation within this section were made by PowerPhotonic Ltd [86] with localised polishing by Krystian Wlodarczyk, whilst the mirrors made using the laser polishing technique with slightly higher than normal incident laser power were made entirely by Krystian Wlodarczyk, a fellow PhD student within the LPA group.

5.6.1 Fabrication Techniques, Mirror Design and Characterisation

The LPA group previously developed a technique to create custom optical surfaces in fused silica utilising CO_2 laser machining [87]. This technique has been employed by PowerPhotonic Ltd. to create custom aberration correcting phase plates for diode laser bars and stacks and is the technique used to create the phase plates mounted on the diode stacks for pumping the Yb:YAG planar waveguide laser. The CO_2 laser is used with a pulsed raster scanning technique to ablate the fused silica substrate into the required shape, leaving a rough surface. After the general shape of the required micro-optic is created, the CO_2 laser is then operated with long pulses and power just below the ablation threshold of the fused silica, this causes the surface of the silica to melt, thus polishing the surface giving extremely low local surface roughness [88]. The finished optic is then sent for HR coating.

A second method of producing mirrors with the CO_2 laser has also been developed within this section by Krystian Wlodarczyk, this method is an extension of the laser polishing procedure and is still under development. A flat fused silica sample is put through the laser polishing procedure but with higher than usual power, this vaporises material from the surface creating a smooth cylindrical trench in the fused silica. Varying the power in the polishing beam and using a raster scanning technique allows for the creation of trenches with variable width and radius of curvature.

Two substrates with 5 stripe mirrors on each have been manufactured using laser cutting and polishing techniques. The first, utilising the laser machining technique was made by PowerPhotonic Ltd. with localised polishing and characterisation by Krystian Wlodarczyk. This mirror was machined into a cylindrical fused silica substrate with curvature of 230 mm, creating a toroidal surface. The shape of the mirror can be seen in figure 5.21, with 5 stripes created with varying central active area curvature, photographs and surface profiles of the stripe mirrors can be seen in figure 5.20a). The active area is made so that its width closely matches the fundamental waveguide mode at the required distance with deep unpolished trenches either side designed to scatter high order modes, effectively creating a mode selective slit within the mirror structure itself. Initially, this mirror was designed for use with the Nd:YAG planar waveguide laser, with the 230 mm cylindrical substrate curvature designed to match a 138 mm output coupler to create a case III unstable resonator, however, the fifth stripe mirror has curvature of 20 mm enabling it to be used as a case III Yb:YAG resonator mirror coupled with the 80% plane output coupler used for other resonators within this chapter. In the transverse, highly curved direction, the surface roughness achieved with this technique is very smooth, measured as $\sim$40 nm peak-to-peak using

an optical surface profiler, whereas in the lateral direction, the surface roughness is slightly worse at ∼100 nm peak to peak. The difference in smoothness is due to errors in the lateral curvature of the substrate, through the use of higher-quality cylindrical substrates the surface roughness will greatly improve.

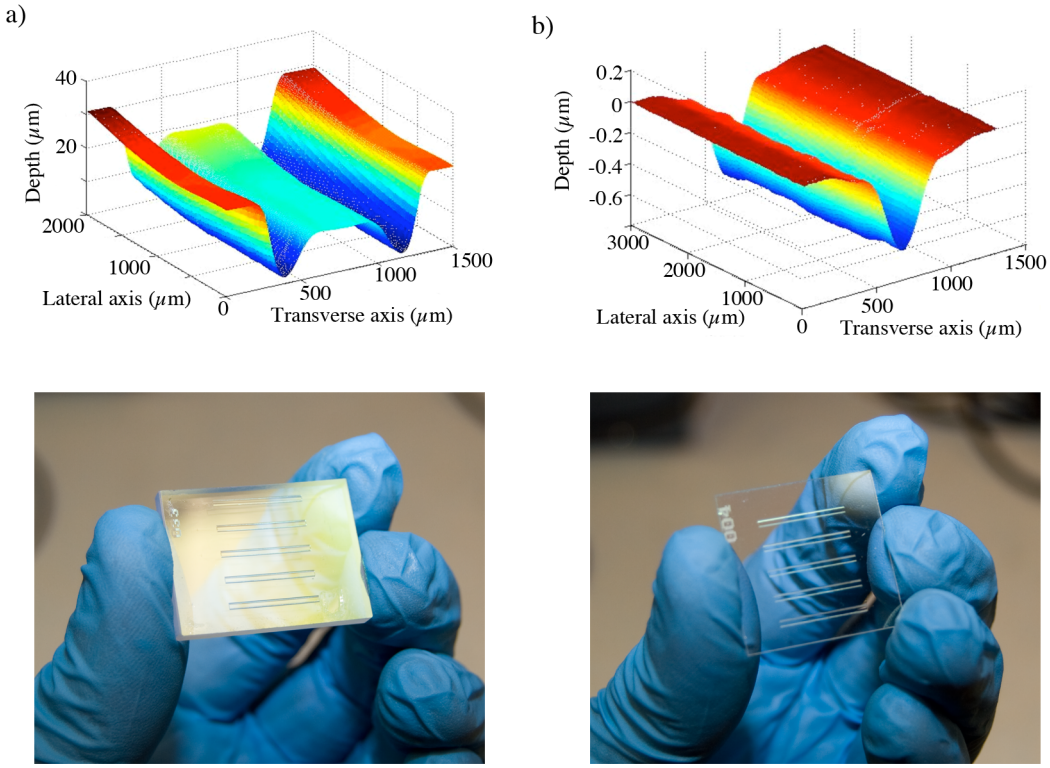

Figure 5.20 – a) surface profile of mirror created using laser cutting of a cylindrical fused silica substrate. b) Surface profile of mirror created using laser ablation technique. Photographs of the various curvature stripe mirrors cut into the silica substrates are shown below the surface profile respectively.

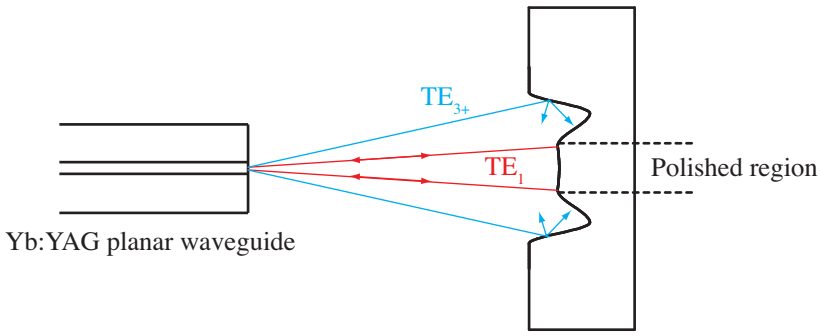

Figure 5.21 – Shape of laser cut resonator mirror, only the central curved region is polished with curvature matching the case III waveguide condition. High order modes are scattered from the unpolished surfaces, enhancing mode selectivity.

The second mirror was manufactured and characterised by Krystian Wlodarczyk using the laser vaporisation technique. Five stripe mirrors were created on a flat fused silica substrate, for each stripe, the laser parameters were varied resulting in three

stripes which could be tested as case III mirrors. The stripe mirrors width closely matches the size of the fundamental waveguide mode, enhancing mode selectivity. The three case III stripe mirrors have curvatures 14.1 mm, 17.7 mm and 19.1 mm, allowing a range of radii to be tested around the required case III radius of curvature. A photograph and surface profile of these stripe mirrors can be seen in figure 5.20b). The surface roughness of these mirrors is ∼60 nm peak-to-peak in the transverse direction. Laterally, the roughness is good locally at only ∼20 nm peak-to-peak, however, over a 20 mm length the low frequency surface roughness is as bad as 500 nm peak-to-peak. The large low frequency peak-to-peak roughness is due to surface of the blank sample being warped from the time of manufacture and is consistent with many different samples from the same batch.

5.6.2 Laser Trials

To test these mirrors, both were aligned individually to the Yb:YAG planar waveguide as the rear resonator mirror in the case III position with the plane, 80% reflectivity output coupler placed 0.5 mm from the opposite facet. Again, due to the unknown damage threshold of the HR coatings, the laser was only operated with an incident diode power of 250 W, limiting the risk of a mirror getting damaged and in turn, damaging the planar waveguide facets. Each mirror was mounted in turn on a 6-axis translation stage, allowing precise alignment to be performed for each stripe mirror, optimising the beam quality and output power. Each stripe mirror was also translated longitudinally, varying the mirror to end-facet separation allowing the optimal position to be determined for each mirror. Figure 5.22 shows the output power for each mirror with varying mirror separation, a maximum power of 56 W was obtained from the 17.7 mm curvature mirror produced using the laser polishing technique. This output nearly matched that obtained from a standard cylindrical lens with the majority of losses, again being attributed to leakage through the optical coatings. The laser cut mirror with mode selective structure worked reasonably well, despite the ∼ 100nm low-frequency surface roughness in the lateral direction. Using this mirror, 40 W of output power was obtained, the loss in output power is due to diffractive losses from the rough lateral surface and the loss of lateral fill factor due to the 230 mm lateral curvature. As the mirror to facet separation is reduced, all mirrors show a rapid decrease in output power, with separation increasing, the drop in power is considerably slower. These output power characteristics are expected due to the case III coupling losses discussed in detail in chapter 1.

The beam profile from all of the mirrors in the transverse direction was excellent when operated in a position that gave maximum output power. The beam profiles for each mirror and comparison with the theoretical TE_1 waveguide mode can be seen in

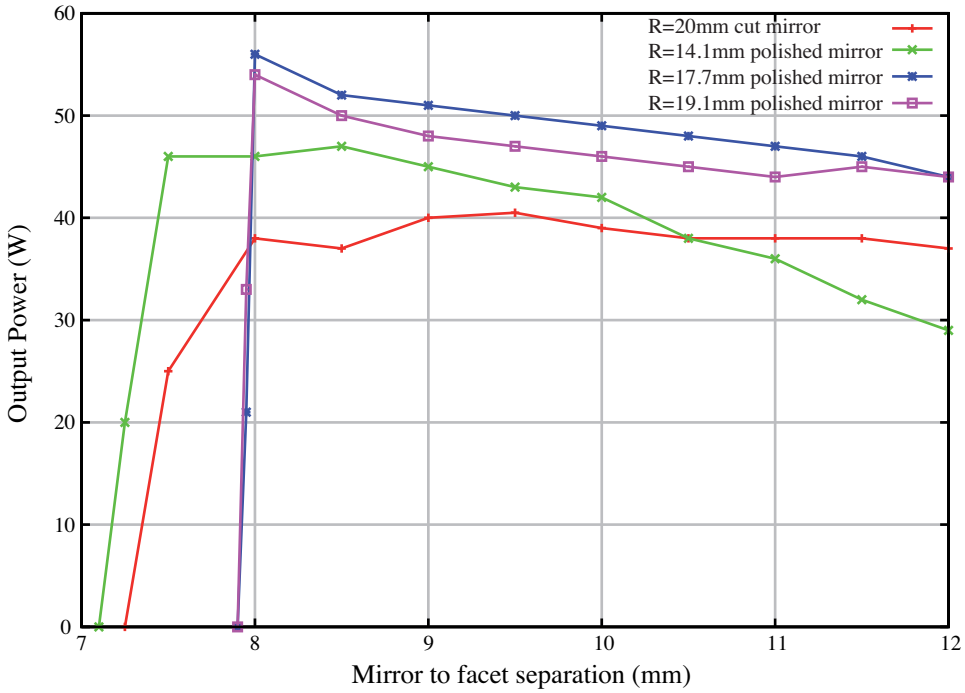

Figure 5.22 – Output power obtained from each laser cut mirror. The 20mm laser cut mirror is on a 230mm curvature cylindrical substrate and was created using laser cutting and polishing whilst the other three mirrors were created on a flat substrate using the enhanced laser polishing technique.

figure 5.23. This shows a good match between the theoretical and experimental beam profiles for all mirrors, showing successful case III operation. However, each profile contains some extra power in the wings, due to either weak higher order modes or through diffraction from the edges of the mirror structure. The beam profiles have very similar properties to those from a standard commercial cylindrical mirror operating in the case III condition.

To the authors knowledge, these results represent the first use of a CO_2 laser machined mirror as a laser resonator mirror. The results obtained from the laser smoothed mirrors are good, nearly matching a commercial cylindrical lens. However, further work is required to reduce the surface roughness. Future work on improving the surface roughness, better optical coatings and resonator design using toroidal optics shows promise for the creation of a case III hybrid unstable resonator with excellent beam quality in the transverse direction whilst the unstable resonator gives excellent beam quality in the lateral direction. The laser cut mirrors also show promise in the creation of custom shaped mirrors for intra-cavity beam shaping such as mode selective and super-gaussian resonators.

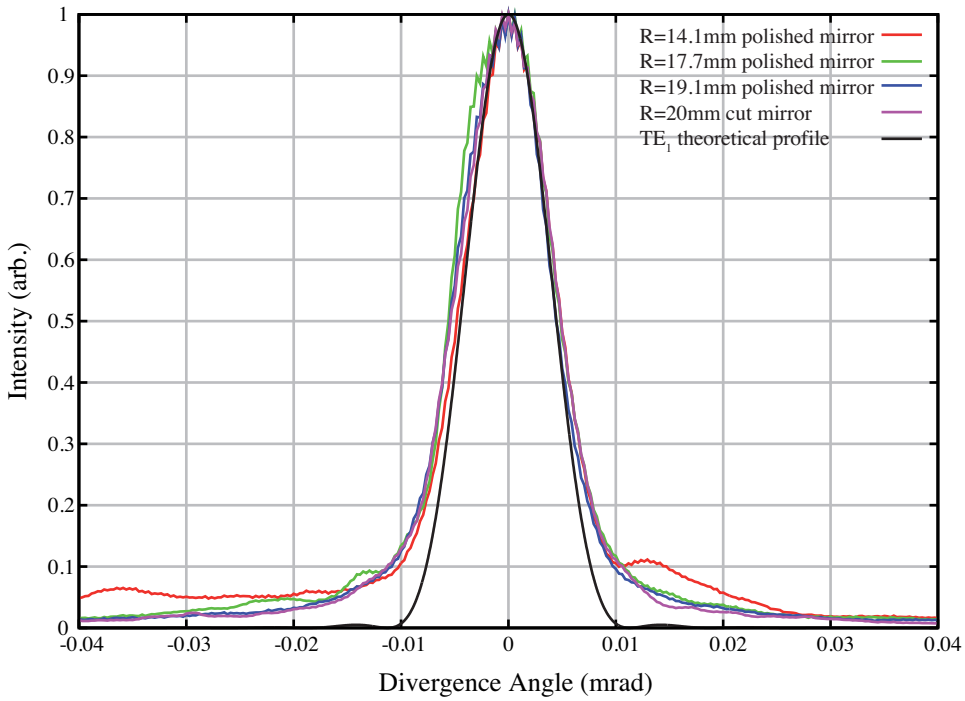

Figure 5.23 – Normalised transverse beam profiles for the various radius of curvature laser cut mirrors plotted along with the theoretical TE_1 beam profile. All mirrors show a good match to the theoretical fundamental waveguide mode.

5.7 Conclusions

Within this chapter, high efficiency lasing from the Yb:YAG planar waveguide has been achieved. Output powers of 400 W with a slope efficiency of 75% represent the highest output power from a diode-pumped solid-state planar waveguide laser to date. Power scaling can be achieved through the use of a wider planar waveguide allowing for greater pump absorption, it is also possible to angularly multiplex more diode bars into each side, with 10-bar stacks available commercially.

Single transverse mode operation has been achieved through using case III waveguide coupling with very little loss to the output power. However, the lateral beam quality is still limited. An attempt was made to improve the lateral beam quality using a hybrid unstable resonator with spherical mirrors, this resulted in single lateral mode operation. Case II coupling when using this resonator resulted in the transverse profile becoming split due to accumulative coupling into the sapphire claddings causing interference.

An intra-cavity slit may clean the transverse profile when using a case II hybrid unstable resonator, however, work on case III laser cut mirrors has proved promising. The first demonstration of a laser cut cylindrical mirror enabled single mode case III operation, with a toroidal mirror also being created by laser machining a cylindrical lens and applying a HR coating. Further resonator design work and improvements to

the laser cutting process are required to develop a toroidal mirrored case III hybrid unstable resonator, this will enable high output power with excellent beam quality in the future.

Chapter 6

Conclusions and Further Work

6.1 Q-switched Nd:YAG and Side-pumped CW Yb:YAG Planar Waveguide Lasers

In this thesis, extending the operation of diode-pumped solid-state planar waveguide lasers into the high pulse-energy Q-switched regime and extended the CW performance using side-pumping of an Yb:YAG gain medium has been reported. Q-switching the Nd:YAG planar waveguide laser proved successful and has shown the limitations on operation due to modulator switch-off time and parasitic oscillation. The initial Yb:YAG planar waveguide design only operated with 10% efficiency. Improvements to the waveguide design suppressed parasitic oscillation, leading to more gain available within the waveguide. Completely redesigned waveguide heatsinks allowed resonator optics to be placed close to the waveguide facets, minimising resonator losses. Finally, the use of double-sided pumping improved the lateral pump uniformity, minimising the laser threshold. These improvements combined to increase the slope efficiency to 75%, representing the highest output power obtained from a solid-state planar waveguide laser to date.

6.1.1 Q-switched Nd:YAG Planar Waveguide Laser

Q-switching of a Nd:YAG planar waveguide laser was achieved through the use of a novel resonator configuration. Placement of the AOM near to the gain medium resulted in a significantly faster optical switching time than that achieved using the standard approach of placing the AOM near to the output coupler. With the AOM in its 'on' state, this resonator configuration couples the diffracted intra-cavity power from the AOM into the waveguide claddings, resulting in significant loss. The RF to the AOM is then switched off, allowing the hybrid unstable resonator to build up a high-energy laser pulse from the energy stored within the planar waveguide. The

hybrid-unstable resonator with an intra-cavity AOM maintained the excellent beam quality previously obtained by Lee [28] with an M^2 of $\sim$1.3.

Q-switched operation resulted in pulse energies as high as 4.5 mJ, with a 15 ns duration at a repetition rate of 5 kHz. High repetition rates gave 1 mJ pulses, with 50 ns duration at a repetition rate of 100 kHz. The unstable resonator was also shown to not introduce additional jitter or decrease the pulse-to-pulse stability when compared to traditional Q-switched lasers. Low repetition rate operation, when the gain is at its highest was shown to be limited by a combination of the AOM optical switching time and parasitic oscillation. High-gain causes a short build-up time, which results in the Q-switched pulse being modulated by the dissipating ultrasound within the AOM, this effect limited the pulse duration to a minimum of 15 ns. Parasitic oscillation was also shown to occur at low repetition rates due to the high-gain available, this clamped the available pulse energy to 4.5 mJ.

These results are competitive with current industrial high-beam quality Q-switched lasers. Other laser systems such as thin disc lasers obtain results similar to those obtained here, however, fibre laser designs must operate with longer pulse lengths to similar pulse energy. There is significant industrial interest in further development of high-beam quality, short pulse duration laser systems. The picosecond pulse length regime is of particular interest due to the low heat affected zone created during machining with a short pulse. To obtain picosecond operation from the planar waveguide laser format, a MOPA system would be required, with a high-beam quality low-power oscillator emitting short pulses which are then amplified by multiple passes through a planar waveguide amplifier.

6.1.2 Side-Pumped Yb:YAG Planar Waveguide Laser

Single-sided pumping of a Yb:YAG planar waveguide was achieved using novel pump units. Initial trials of this laser gave disappointingly low output power with less than 10% efficiency, the poor efficiency was shown to be due to a combination of resonator losses and parasitic oscillation within the waveguide core. Originally, the waveguide was designed with a single edge facet chamfered to 7° to promote coupling of trapped rays from the core, however, experimental results showed this to be insufficient. The resonator losses are caused by poor waveguide coupling due to the need for an intra-cavity lens to compensate for both the shortened waveguide and a significant overhang of the metalwork needed for the heatsinks preventing close-coupled optics.

Parasitic oscillation was detected operating within the Yb:YAG planar waveguide, strongly competing with the laser resonator for gain. Through ray tracing of the mean spontaneous emission ray path length within the core, it was shown both edge facets

need to be chamfered with optimal angles of 7° and 20°. The planar waveguides were then re-polished, successfully suppressing parasitic oscillation.

Utilising a hybrid-stable waveguide resonator on the parasitic suppressing waveguides resulted in an improvement of efficiency from 10% to 57%. The beam properties and high threshold showed the laser to be limited by pump uniformity. The large width of the waveguide combined with single-edge pumping required a high incident pump intensity to bring the full-width of the waveguide above the Yb:YAG transparency threshold, causing a high laser threshold.

The original heatsink design prevented resonator optics from being placed close to the waveguide facets, significantly limiting the available resonator options. New heatsinks were designed to allow for close-coupled resonator optics, removing the need for cylindrical lens elements within the resonator. The heatsinks comprise of two parts, contact cooling the waveguide through the use of micro-channel water coolers. The new heatsinks were designed to be flush with the waveguide end facets in the longitudinal direction. The reduced space available longitudinally caused the new heatsink design to require lateral water flow as more space is available in the pump direction. To prevent a thermal gradient occurring within the waveguide due to the lateral water flow, the water was pumped through the top and bottom heatsinks in opposite directions.

It was critical to measure the pump uniformity through the planar waveguide due to the three-level nature of Yb:YAG. Any under-pumped regions result in absorption at the laser wavelength introducing significant loss. By imaging the fluorescence at the waveguide end facets with a camera, both the alignment and an approximation of the pump uniformity could be monitored. A peak in the fluorescence intensity indicated optimum alignment, whilst the image of the facet gave the fluorescence intensity variation laterally through the waveguide, giving an approximation of the pump absorption profile. Under single-sided pumping, the pump profile followed a Beer's law absorption curve across the width of the waveguide. This caused approximately half of the waveguide to be absorbing near laser threshold, increasing it substantially. To improve the pump uniformity, a second diode stack was used to pump both edge facets simultaneously. This resulted in a reasonably uniform pump profile across the width of the waveguide and minimising the laser threshold.

The gain within the waveguide core was measured through the use of a 1030 nm, 15 mW diode laser. This laser was mode-matched into waveguide core, with the increase in power measured with the laser propagating through the waveguide in 5 mm intervals laterally. This gave the gain profile laterally through the waveguide with varying incident pump intensity. Under maximum incident pump intensity, uniform small-signal gain of 1 cm^{-1} was measured across the width of the waveguide. This

gives an amplification factor of three to four times per pass. The gain is partly limited by green emission due to cooperative luminescence. Measuring the gain with varying pump intensity showed pump saturation to occur under double-sided pumping conditions, which allows for good performance as either an amplifier or a pulsed laser. 1 cm^{-1} is not a particularly high-gain, however, it is ideal for amplification. A lower gain in an amplifier minimises losses due to ASE, which is currently a scaling limit in thin disc lasers.

Improved heatsinks and double-sided pumping allowed high-efficiency laser operation to take place. A cavity working as a dual-case I waveguide resonator in the transverse direction and a plano-concave free-space stable resonator in the lateral direction gave an output power of 400 W with a slope efficiency of 75% represents the highest output power from a solid-state planar waveguide laser to date. The pump uniformity in the transverse direction promoted natural mode selectivity, resulting in single transverse mode operation from a non-mode selective resonator. To clean up the lateral beam profile, a modified version of the hybrid negative branch unstable resonator previously used for the Nd:YAG planar waveguide was used. This consisted of two spherical mirrors, one placed in the case II position, the other in the case I position. The hybrid unstable resonator gave an output power of 300 W, with single-mode operation in the lateral direction. However, the transverse beam profile became an envelope of fringes with divergence equivalent to single-mode operation. This was due to continuous coupling of radiation into the claddings during the unstable resonator walk-out resulting in a diffraction pattern in the laser output.

The results from this thesis show the need for cheap toroidal mirrors for lasers with high lateral to transverse aspect-ratio such as planar waveguide and slab lasers. When using a planar waveguide, the transverse direction requires mirrors with very short radius of curvature, operating in the case III position. However, in the lateral direction, the mirrors need a radius of curvature ∼10x higher than the transverse direction to satisfy the confocal unstable resonator condition. Through the use of a CO_2 laser ablation and polishing technique, both custom cylindrical mirrors and toroidal mirrors were manufactured. These mirrors had excellent surface quality, successfully giving case III operation from the planar waveguide laser. Further research is required to produce mirrors which can create a hybrid case III unstable resonator.

6.2 Further Work

The Q-switched Nd:YAG planar waveguide laser is currently limited only by the available pump power in the high repetition rate regime. Development of a pump chamber with 100 W diode bars, totalling 1 kW incident power would allow operation

of this laser to extend out to 200 kHz repetition rates with 1 mJ pulse energy and 60 ns pulse duration. This laser would be ideal for rapid machining in many industrial applications. To improve the pulse-energy at low repetition rates, an improved AOM would be required giving a 50 ns switch-off time allowing for shorter build-up times, combining this with parasitic oscillation suppression would result in a laser capable of producing 8 mJ, sub-10 ns pulses with a repetition rate of 10 kHz. High pulse-energy at this repetition rate would be suitable for applications such as industrial laser machining and particle image velocimetry.

Improvements to the Yb:YAG laser require further development of the custom laser cut toroidal mirrors introduced within this thesis. Designing a mirror that would allow either a positive or negative branch resonator combined with a case III waveguide resonator would result in single spatial mode operation in both the lateral and transverse directions whilst maintaining the multi-mode output power. Power scaling is also possible, through increasing the width of the planar waveguide, more of the incident pump light will be absorbed, resulting in higher output powers. With increased width, it is also possible to angularly multiplex more diode bars into the waveguide using new aberration correcting phase plates. This gives the possibility of a planar waveguide laser side-pumped by two ten-bar diode stacks. Pump absorption could also be improved through the use of ceramic material with a variation in doping concentration across the width of the waveguide, with the highest concentration in the centre. This would lead to higher absorption and a more uniform pump profile than that already achieved using double-sided pumping techniques. It is also possible to scale the output power through the use of planar waveguide MOPA systems.

Q-switching of the Yb:YAG planar waveguide laser would be possible, however, the high-gain present would result in very short pulse build-up times placing restrictive design constraints on the modulator required. The biggest draw-back of Q-switched operation of this laser is due to the the high energy storage in Yb:YAG. This can result in pulses with pulse energy more than 75% of the damage threshold of the Yb:YAG itself, resulting in significant risk of damage to the planar waveguide. Recently, an Yb:YAG thin-disc laser developed by Antognini *et al.* [59] overcame this problem through the use of a novel MOPA configuration. An initial Q-switched Yb:YAG oscillator utilised a combination of Q-switching and cavity dumping to obtain an initial high-energy seed pulse for an Yb:YAG power amplifier. The oscillator was Q-switched to generate an initial pulse, this pulse was then coupled out of the cavity using an EOM after a certain time delay, preventing the pulse from reaching saturation and destroying the thin-disc. A similar resonator could be implemented on the Yb:YAG planar waveguide laser, however, the large aperture in the lateral direction limits the possible resonator configurations and possible modulators.

The high-gain measured in chapter 4 shows promise for operation as an amplifier. Amplification factors of 3-4x per pass can result in a 1 W seed laser being amplified to more than 500 W after 6 passes through the Yb:YAG planar waveguide. Toroidal mirrors would be extremely useful in this application to maintain single-mode waveguide coupling in the transverse direction whilst increasing the lateral width of the amplified beam to prevent it from reaching saturation intensity after multiple-passes. Rubbuldt *et al.* [89] have recently developed an Yb:YAG INNOSLAB slab amplifier, where a 1 W femtosecond master oscillator is amplified to 400 W average power, with 682 fs pulses at a 76 MHz repetition rate, representing the current world record in femtosecond laser power. The dimensions of the slab used are similar to the planar waveguide presented within this thesis, however, the gain is slightly lower than that shown to be present in the Yb:YAG planar waveguide. This means the Yb:YAG planar waveguide laser presented here should be better than INNOSLAB systems when operated as an amplifier.

There is increasing industrial and military interest in lasers operating in the mid-IR, with wavelengths greater than 2 μm. Industrial applications require this due to the eye-safe nature of these wavelengths, whilst military applications take advantage of the low atmospheric absorption in the mid-IR regions. Future high-power planar waveguide lasers are likely to operate using materials such as Tm:YAG, giving mid-IR emission, utilising ceramic YAG for the gain section to reduce costs. Currently, the cost of producing a planar waveguide is prohibitive due to the expensive contact bonding technique used. Research is ongoing to create ceramic planar waveguides, which can be bonded cheaply during the sintering stage of manufacture. The expense of contact bonded planar waveguides is also leading to research on gain guided planar waveguide lasers. This consists of a cheap ceramic slab that is side pumped to create a sheet of gain $\sim$500 μm in height, offering an inexpensive alternative to the planar waveguide laser.

References

[1] J. Hecht, "Ray guns get real," *IEEE Spectrum*, pp. 25–29, July 2009.

[2] W. Koechner, *Solid-State Laser Engineering, Fifth Edition*. Springer, 1999.

[3] J. Eggleston, T. Kane, J. Unternahrer, and R. Byer, "Slab-geometry Nd:glass laser performance studies," *Optics Letters*, vol. 7, no. 9, pp. 405–407, 1982.

[4] F. Sun, "Thermally induced beam steering in high power diode-pumped planar waveguide lasers," *PhD Thesis, Heriot-Watt University, Edinburgh*, 2007.

[5] J. Mackenzie and H. Meissner, "High-power and ultra-efficient operation of a 946nm Nd:YAG planar waveguide laser," *ASSP Conference, Denver*, 2009.

[6] K. Sueda, H. Takahashi, S. Kawato, and T. Kobayashi, "High-efficiency laser-diodes-pumped microthickness Yb:$Y_3Al_5O_{12}$ slab laser," *Applied Physics Letters*, vol. 87, no. 151110, 2005.

[7] H. Kogelnik and C. Shank, "Stimulated emission in a periodic structure," *Applied Physics Letters*, vol. 18, no. 4, pp. 152–154, 1971.

[8] J. Degnan and D. Hall, "Finite aperture waveguide resonators," *IEEE Journal of Quantum Electronics*, vol. 9, no. 9, pp. 901–910, 1973.

[9] A. Colley, H. Baker, and D. Hall, "Planar waveguide, 1 kW cw, carbon dioxide laser excited by a single rf discharge," *Applied Physics Letters*, vol. 61, pp. 136–138, 1992.

[10] "http://www.trumpf.com," *Trumpf Group, USA*, 2009.

[11] J. Mackenzie, "Dielectric solid-state planar waveguide lasers: A review," *IEEE Journal of Selected Topics in Quantum Electronics*, vol. 13, no. 3, pp. 626–637, 2007.

[12] A. Faulstich, H. Baker, and D. Hall, "Face pumping of thin, solid-state slab lasers with laser diodes," *Optics Letters*, vol. 21, no. 8, pp. 594–596, 1996.

[13] J. Lee, H. Baker, G. Friel, G. Hilton, and D. Hall, "High-average-power Nd:YAG planar waveguide laser that is face pumped by 10 laser diode bars," *Optics Letters*, vol. 27, no. 7, pp. 524–526, 2002.

[14] L. Xiao, X. Cheng, and J. Xu, "High-power Nd:YAG planar waveguide laser with YAG and Al_2O_3 claddings," *Optics Communications*, vol. 281, pp. 3781–3785, 2008.

[15] J. Xu, I. Thomson, J. Valera, H. Baker, A. Russell, and D. Hall, "A planar waveguide Nd:YAG laser using active Q-switching of a hybrid unstable resonator," *IEEE Journal of Selected Topics in Quantum Electronics*, vol. 13, no. 3, pp. 638–646, 2007.

[16] S. Hettrick, J. Mackenzie, R. Harris, J. Wilkinson, and D. Shepherd, "Ion-exchanged tapered-waveguide laser in neodymium-doped BK7 glass," *Optics Letters*, vol. 25, no. 19, pp. 1433–1435, 2000.

[17] P. Chandler, S. Field, D. Hanna, D. Shepherd, P. Townsend, A. Tropper, and L. Zhang, "Ion-implanted Nd:YAG planar waveguide laser," *Electronics Letters*, vol. 25, no. 15, pp. 985–986, 1989.

[18] E. Daran, D. Shepherd, T. Bhutta, and C. Serrano, "Laser operation of Nd:LaF_3 thin film grown by molecular beam epitaxy," *Electronics Letters*, vol. 35, no. 5, pp. 398–400, 1999.

[19] I. Chartier, B. Ferrand, D. Pelenc, S. Field, D. Hanna, A. Large, D. Shepherd, and A. Tropper, "Growth and low-threshold laser oscillation of an epitaxially grown Nd:YAG waveguide," *Optics Letters*, vol. 17, no. 11, pp. 810–812, 1992.

[20] R. Eason, T. May-Smith, C. Grivas, M. Darby, D. Shepherd, and R. Gazia, "Current state-of-the-art of pulsed laser deposition of optical waveguide structures: Existing capabilites and future trends," *Applied Surface Science*, vol. 255, no. 10, pp. 5199–5205, 2009.

[21] "http://www.onyxoptics.com/," *Onyx Optics Inc., USA*, 2009.

[22] C. Brown, C. Bonner, T. Warburton, D. Shepherd, A. Tropper, and H. Meissner, "Thermally bonded planar waveguide lasers," *Applied Physics Letters*, vol. 71, no. 9, pp. 1139–1141, 1997.

[23] D. Shepherd, C. Bonner, C. Brown, W. Clarkson, A. Tropper, D. Hanna, and H. Meissner, "High-numerical-aperture, contact-bonded, planar waveguides for diode-bar-pumped lasers," *Optics Communications*, vol. 160, no. 1, pp. 47–50, 1999.

[24] C. Bonner, T. Bhutta, D. Shepherd, and A. Tropper, "Double-clad structures and proximity coupling of diode-bar-pumped planar waveguide lasers," *IEEE Journal of Quantum Electronics*, vol. 36, no. 2, pp. 236–242, 2000.

[25] D. Shepherd, S. Hettrick, C. Li, J. Mackenzie, R. Beach, S. Mitchell, and H. Meissner, "High-power planar dielectric waveguide lasers," *Journal of Physics D: Applied Physics*, vol. 34, pp. 2420–2432, 2001.

[26] J. Verdeyen, *Laser Electronics, 3rd Edition.* Prentice Hall, 1994.

[27] H. Baker, J. Lee, and D. Hall, "Self-imaging and high-beam-quality operation in multi-mode planar waveguide optical amplifiers," *Optics Express*, vol. 10, no. 6, pp. 297–302, 2002.

[28] J. Lee, *High power, diode-pumped, planar waveguide lasers with excellent beam quality.* PhD thesis, Heriot-Watt University, Edinburgh, 2002.

[29] J. Mackenzie, C. Li, D. Shepherd, R. Beach, and S. Mitchell, "Modeling of high-power continuous-wave Tm:YAG side-pumped double-clad waveguide lasers," *IEEE Journal of Quantum Electronics*, vol. 38, no. 2, pp. 222–230, 2002.

[30] H. Baker, J. Valera, J. Monjardin, and D. Hall, "Edge-pumped Yb:YAG planar waveguide laser," *Europhoton Conference, Pisa*, 2006.

[31] A. Siegman, *Lasers.* University Science Books, 1986.

[32] I. Ananev, V. Sherstobitov, and N. Sventsitskaia, "Properties of a laser with an unstable resonator," *Soviet Physics-JETP*, vol. 28, pp. 69–74, 1969.

[33] W. Krupke and W. Sooy, "Properties of an unstable confocal resonator CO_2 laser system," *IEEE Journal of Quantum Electronics*, vol. 5, no. 12, pp. 575–586, 1969.

[34] A. Siegman, "Unstable optical resonators," *Applied Optics*, vol. 13, no. 2, pp. 353–367, 1974.

[35] Y. Ananev, "Unstable resonators and their applications," *Soviet Journal of Quantum Electronics*, vol. 1, no. 6, p. 565, 1972.

[36] O. Bourne and P. Dyer, "A novel stable-unstable resonator for beam control of rare-gas halide lasers," *Optics Communications*, vol. 31, no. 2, pp. 193–196, 1979.

[37] P. Jackson, H. Baker, and D. Hall, "CO_2 large-area discharge laser using an unstable-waveguide hybrid resonator," *Applied Physics Letters*, vol. 54, pp. 1950–1952, 1989.

[38] J. Mackenzie and W. Clarkson, "Circular output from a high power Nd:YLF slab laser," *Proceedings of SPIE Solid State Lasers XVII: Technology and Devices*, vol. 6871, 2008.

[39] E. Snitzer, "Optical maser action of Nd^3+ in a barium crown glass," *Physical Review Letters*, vol. 7, no. 12, pp. 444–446, 1961.

[40] J. Geusic, H. Marcos, and L. V. Uitert, "Laser oscillations in Nd-doped yttrium aluminum, yttrium gallium and gadolinium garnets," *Applied Physics Letters*, vol. 4, no. 10, pp. 182–184, 1964.

[41] W. Krupke, "Ytterbium solid-state lasers - the first decade," *IEEE Journal of Selected Topics in Quantum Electronics*, vol. 6, no. 6, pp. 1287–1296, 2000.

[42] A. Kaminskii, "Laser crystals and ceramics: recent advances," *Laser and Photonics Review*, vol. 1, no. 2, pp. 93–177, 2007.

[43] A. Ikesue, T. Kinoshita, K. Kamata, and K. Yoshida, "Fabrication and optical properties of high-performance polycrystalline Nd:YAG ceramics for solid-state lasers," *Journal of the American Ceramic Society*, vol. 78, no. 4, pp. 1033–1040, 1995.

[44] "http://www.konoshima.co.jp/en/index.html," *Konoshima Chemical Company Ltd., Japan*, 2009.

[45] J. Lu, K. ueda, H. Yagi, T. Yanagitani, Y. Akiyama, and A. Kaminskii, "Neodymium doped yttrium aluminum garnet ($Y_3Al_5O_{12}$) nanocrystalline ceramics - a new generation of solid state laser and optical materials," *Journal of Alloys and Compounds*, vol. 341, no. 1, pp. 220–225, 2002.

[46] H. Yagi, J. Bisson, K. ueda, and T. Yanagitani, "$Y_3Al_5O_{12}$ ceramic absorbers for the suppression of parasitic oscillation in high-power Nd:YAG lasers," *Journal of Luminescence*, vol. 121, no. 1, pp. 88–94, 2006.

[47] "Transparent ceramics spark laser advances," *Lawrence Livermore National Laboratories, S&TR*, April 2006.

[48] F. M. R. Hellwarth, "Giant optical pulsations from ruby," *Journal of Applied physics*, vol. 33, no. 3, pp. 828–829, 1962.

[49] W. Wagner and B. A. Lengyel, "Evolution of the giant pulse in a laser," *Journal of Applied physics*, vol. 34, no. 7, pp. 2040–2046, 1963.

[50] W. Silfvast, *Laser Fundamentals*. Cambridge University Press, 1996.

[51] J. Mackenzie and D. Shepherd, "An end-pumped, passively q-switched, Yb:YAG double-clad waveguide laser," *Optics Letters*, vol. 27, no. 24, pp. 2161–2163, 2002.

[52] M. Shverdin, D. Walker, D. Yavuz, G. Yin, and S. Harris, "Generation of a single-cycle optical pulse," *Physical Review Letters*, vol. 94, no. 033904, 2005.

[53] E. Lallier, J. Pocholle, M. Papuchon, Q. He, M. de Micheli, D. Osstrowsky, C. Grezes-Besset, and E. Pelletier, "Integrated Nd:MgO:$LiNbO_3$ fm mode-locked waveguide laser," *Electronics Letters*, vol. 27, no. 11, pp. 936–937, 1991.

[54] R. Wessel, R. Ricken, K. Rochhausen, H. Suche, and W. Sohler, "Supermode stabilized coupled-cavity 5- and 10-GHz mode-locked Ti:Er:$LiNbO_3$ waveguide lasers," *IEEE Journal of Quantum Electronics*, vol. 36, no. 3, pp. 394–399, 2000.

[55] E. Thoen, E. Koontz, D. Jones, F. Kartner, E. Ippen, and L. Kolodziejski, "Erbium-ytterbium waveguide laser mode-locked with a semiconductor saturable absorber mirror," *IEEE Photonics Technology Letters*, vol. 12, no. 2, pp. 149–151, 2000.

[56] A. Giesen, H. Hugel, A. Voss, K. Wittig, U. Brauch, and H. Opower, "Scalable concept for diode-pumped high-power solid-state lasers," *Applied Physics B: Lasers and Optics*, vol. 58, no. 5, pp. 365–372, 1994.

[57] J. Abate, L. Lund, D. Brown, S. Jacobs, S. Refermat, J. Kelly, M. Gavin, J. Waldbillig, and O. Lewis, "Active mirror: A large-aperture medium-repetition rate Nd:glass amplifier," *Applied Optics*, vol. 20, no. 2, pp. 351–361, 1981.

[58] J. Deile, R. Brockmann, and D. Havrilla, "Current status and most recent developments of industrial high power disk lasers," *CLEO Conference, Paper CThA4*, 2009.

[59] A. Antognini, K. Schuhmann, F. Amaro, F. Biraben, A. Dax, A. Giesen, T. Graf, T. Hansch, P. Indelicato, L. Julien, K. Cheng-Yang, P. Knowles, F. Kottmann, E. L. Bigot, L. Yi-Wei, L. Ludhova, N. Moschuring, F. Mulhauser, T. Nebel, F. Nez, P. Rabinowitz, C. Schwob, D. Taqqu, and R. Pohl, "Thin-disk Yb:YAG oscillator-amplifier laser, ASE, and effective Yb:YAG lifetime," *IEEE Journal of Quantum Electronics*, vol. 45, no. 8, pp. 993–1005, 2009.

[60] A. Giesen and J. Speiser, "Fifteen years of work on thin-disk lasers: Results and scaling laws," *IEEE Journal of Selected Topics in Quantum Electronics*, vol. 13, no. 3, pp. 598–609, 2007.

[61] T. Dekorsy, J. Neuhaus, D. Bauer, C. Scharfenberg, J. Kleinbauer, A. Killi, S. Weiler, and D. Sutter, "Femtosecond high-power thin-disc laser oscillators," *CLEO Conference, Paper CThJ3*, 2009.

[62] A. Liu and K. Ueda, "The absorption characteristics of circular, offset, and rectangular double-clad fibers," *Optics Communications*, vol. 132, no. 5, pp. 511–518, 1996.

[63] V. Dominic, S. MacCormack, R. Waarts, S. Sanders, S. Bicknese, R. Dohle, E. Wolak, P. Yeh, and E. Zucker, "110W fibre laser," *Electronics Letters*, vol. 35, no. 14, pp. 1158–1160, 1999.

[64] "http://www.ipgphotonics.com/," *IPG Photonics, USA*, 2009.

[65] R. Paschotta, *Encyclopedia of Laser Physics and Technology*. Wiley-VCH, 2008.

[66] H. Baker, A. Chesworth, D. P. Millas, and D. Hall, "A planar waveguide Nd:YAG laser with a hybrid waveguide-unstable resonator," *Optics Communications*, vol. 191, pp. 125–131, 2001.

[67] H. Baker, J. Valera, A. Russell, I. Thomson, and D. Hall, "Q-switching of an unstable resonator for a high average power, planar waveguide Nd:YAG laser," *CLEO conference*, 2006.

[68] H. Baker, "Waveguide laser resonator," *US Patent*, no. 7050476, 2006.

[69] J. Xu *Private Communications*, 2005.

[70] "http://www.gsig.com/," *GSI Group Inc., UK*, 2009.

[71] I. Thomson, J. Valera, H. Baker, A. Russell, and D. Hall, "Q-switching dynamics of an efficient, unstable resonator, planar waveguide laser," *Europhoton Conference, Pisa, Paper TuA5*, 2006.

[72] J. Monjardin, K. Nowak, H. Baker, and D. Hall, "Correction of beam errors in high power laser diode bars and stacks," *Optics express*, vol. 14, no. 18, pp. 8178–8183, 2006.

[73] J. Hecht, *Optics, 4th Edition*. Addison Wesley, 2001.

[74] W. Krupke and L. Chase, "Ground-state depleted solid-state lasers and laser amplifiers," *Optical and Quantum Electronics*, vol. 22, pp. 1–22, 1990.

[75] A. Kaminskii, *Crystalline lasers: Physical processes and operating schemes*. CRC Press, 1996.

[76] T. Fan, "Heat generation in Nd:YAG and Yb:YAG," *IEEE Journal of Quantum Electronics*, vol. 29, no. 6, pp. 1457–1459, 1993.

[77] H. Yin, P. Deng, and F. Gan, "Defects in YAG:Yb crystals," *Journal of Applied physics*, vol. 83, no. 7, pp. 3825–3828, 1998.

[78] S. Xu, D. Fang, Z. Zhang, and Z. Jiang, "Effect of OH^- on upconversion luminescence of Er^{3+} doped oxyhalide tellurite glasses," *Journal of Solid State Chemistry*, vol. 178, pp. 2159–2162, 2005.

[79] R. Walti, W. Luthy, H. Weber, S. Rusanow, A. Yakovlev, A. Zagumenyi, I. Shcherbakov, and A. Umyskov, "Yb^{3+}/Ho^{3+} energy exchange mechanisms in Yb:Ho:YAG crystals for 2 μm or 540 nm lasing," *Journal of quantitative spectroscopy and radiative transfer*, vol. 54, no. 4, pp. 671–681, 1995.

[80] E. Nakazawa and S. Shionoya, "Cooperative luminescence in $YbPO_4$," *Physical Review Letters*, vol. 25, no. 25, pp. 1710–1712, 1970.

[81] M. Ito, C. Goutaudier, Y. Guyot, K. Lebbou, T. Fukuda, and G. Boulon, "Crystal growth, Yb^{3+} spectroscopy, concentration quenching analysis and potentiality of laser emission in $Ca_{1-x}Yb_xF_{2+x}$," *Journal of Physics: Condensed Matter*, vol. 16, pp. 1501–1521, 2004.

[82] M. Malinowski, M. Kaczkan, R. Piramidowicz, Z. Frukacz, and J. Sarnecki, "Cooperative emission in Yb^{3+}:YAG planar epitaxial waveguides," *Journal of Luminescence*, vol. 94-95, pp. 29–33, 2001.

[83] X. Xu, Z. Zhao, P. Song, B. Jiang, G. Zhou, J. Xu, P. Deng, G. Bourdet, J. C. Chanteloup, J. Zou, and A. Fulop, "Upconversion luminescence in yb^{3+} -doped yttrium aluminum garnets," *Physica B*, vol. 357, pp. 365–369, 2005.

[84] I. Thomson, H. Baker, N. Trela, J. Monjardin, J. Valera, and D. Hall, "Double sided diode edge-pumped yb:yag planar waveguide laser with 230w output power," *CLEO conference*, 2009.

[85] R. Beach, "CW theory of quasi-three level end-pumped laser oscillators," *Optics Communications*, vol. 123, pp. 385–393, 1995.

[86] "http://www.powerphotonic.co.uk," *PowerPhotonic Ltd., UK*, 2010.

[87] G. Markillie, H. Baker, F. Villarreal, and D. Hall, "The effect of vaporization and melt ejection on laser machining of silica glass micro-optical components," *Applied Optics*, vol. 41, p. 5660, 2002.

[88] K. Nowak, H. Baker, and D. Hall, "Efficient laser polishing of silica micro-optical componenets," *Applied Optics*, vol. 45, no. 162, 2006.

[89] P. Rubbuldt, H. Hoffmann, and T. Mans, "Power scaling of ytterbium INNOSLAB amplifiers beyond 100w average power," *SPIE Photonics West*, 2009.